SolidGround

Energinet
Energy Island North Sea

Seismic geotechnical interpretation of seismic dual setup

July 6, 2023

This document is confidential to Energinet and SolidGround

This report was prepared by:

Frederik Horn, Seismic specialist
Henrik Juhl Hansen, Lead Geophysicist
Ask Frode Jakobsen, Rock/soil physicist
Santosh Kuppens, QI Geophysicist
Bruno Stuyts, Geotechnical Engineer
Esben Dalgaard, Project Manager

SolidGround ApS
Århusgade 88, 1.
DK-2100 Copenhagen Ø
Denmark
Phone: +45 4041 9842
Email: info@solidground.xyz

Contents

Contents

Chapter 1

Executive summary

Project scope

In order to address the potential risks associated with settlements beneath the planned site of the artificial energy island, a 2D seismic survey was conducted. The survey aimed to penetrate the subsurface down to the Top Chalk surface, reaching depths of 1200-1600 meters below the seafloor. The collected seismic data, along with geotechnical information and deep borehole data, were utilized for a comprehensive geotechnical interpretation analysis. The analysis focused on determining the elastic parameters of the sedimentary layers spanning from the seabed to the Top Chalk surface. This information will contribute to assessing and mitigating settlement risks in the vicinity of the future energy island.

All seismic data lines were acquired by Ocean Infinity, using a 2D dual seismic configuration which involved the utilization of two distinct systems. The first system employed was a high frequency multi-channel seismic setup, which specifically targeted the shallow sections. Conversely, the second system used a relative low frequency multi-channel seismic setup, with a primary focus on capturing data from the deep sections. The lines were processed by Geourveys, who also provided the seismic interpretations.

The geotechnical data consists of 280 seabed CPTs, 3 downhole (deep) CPTs, 12 S-CPTs, 8 P-S loggings, 12 sampling boreholes with associated laboratory testing. These data were collected and delivered by Fugro. Data from 3 deep boreholes with measured P-wave velocity and logged gammaray were acquired from the GEUS database.

This approach ensured comprehensive coverage and enabled the acquisition of detailed information from both shallow and deep areas of interest.

Project outcome
The following products were obtained through seismic inversion and interpretation:

- Elastic and deformation parameters

Young's Modulus	Poisson's ratio	Bulk Modulus
Initial Shear Modulus	Density	

- Soil type classification

Sand	Sand with gas shows	Chalk
Clay	Lignite	Harder soils

- Pore pressure

Hydrostatic pressure	Pore pressure	Excess pore pressure

- CPT interpretation/Synthetic CPTs

  Cone resistance

Considerations

The project's outcome provides a comprehensive assessment of the geotechnical ground conditions from a seismic perspective. Two distinct seismic datasets were utilized to target different depth intervals, each presenting its own unique challenges.

In the case of the shallow section, a high frequency seismic dataset was extensively analyzed to predict geotechnical parameters. However, this dataset was more susceptible to the influence of weather conditions compared to the deeper relative low frequency seismic data. Notably, distinct noise signatures were observed in the shallow dataset and effectively mitigated. The shallow section benefitted from a substantial amount of ground truth data, which greatly supported the modeling and validation process.

For the deeper part, the availability of ground truth data was significantly limited. Consequently, the absolute values obtained for the deeper parts of the study may be somewhat biased due to reliance on a single ground truth location within the study area. Nevertheless, the results align well with observations from geologically analogous settings, confirming their reliability and validity.

In conclusion, the findings of this study were influenced by the limited availability of ground truth data, especially at greater depths, leading to a relatively high uncertainty of absolute values of deformation and elastic parameters. Despite this limitation, the seismic data quality was deemed to be of good quality, which resulted in a relatively low level of uncertainty with respect to the relative changes in the derived results.

Comparison of the seismic frequency bandwidth with the seismic derived results at ground truth locations, it is concluded that layers down to 50 centimeters are resolved with the high

frequency system whereas layers down to 5 meters are resolved using the relative lower frequency system.

Zooming in on the results below the energy island location, a comprehensive examination was conducted to identify any significant anomalies within the sedimentary composition, pressure regime, and derived elastic parameters. The study indicated that the sedimentary composition in the pre-quaternary with a high likelihood primarily consists of clay, interspersed with a few layers of homogeneous sand. Notably, with high certainty the data did not reveal any evidence of gas or anomalous excess pore pressure in the pre-quaternary sand layers. The characteristics of the pre-quaternary layers, extending to the chalk surface, were estimated to be similar to the observations from IDA-1, Ibenholt-1, and Inez-1 wells, except for the absence of gas beneath the seismic lines at the energy island location.

Regarding the quaternary section, the data analysis benefited from an extensive amount of ground truth data, which instilled a high level of confidence in the findings. However, the deepest channel infill posed the greatest uncertainty as it is unsampled by any ground pepetrations and lacked comparable sediment samples, making it a subject of future investigation.

In summary, while the study encountered challenges related to limited ground truth data, particularly at greater depths, the seismic data quality and the analysis of relative changes in derived results provided valuable insights. Future studies can focus on addressing the uncertainties associated with deeper channel infill and expanding the scope of ground truth data to enhance the accuracy and reliability of geological and geotechnical interpretations in the area.

Chapter 2

Introduction

2.1 General

Energinet Eltransmission A/S (Energinet) is currently engaged in the development of a new offshore energy island situated in the Danish Sector of the North Sea. This report presents the findings of the seismic geotechnical interpretation conducted using a seismic dual setup. The dual setup allowed for the mapping of both the shallow portion, reaching depths of 1-200 meters, as well as the relatively deeper section extending down to the chalk layer. The survey area for this project is located offshore Denmark, approximately 100 km west of Thorsminde. Figure 2.1 provides an overview of the site's location and illustrates the survey data used for the analysis.

2.2 Project scope

To mitigate the potential risk of settlements underneath the future location of the artificial energy island, a 2D seismic survey with a penetration depth down to the Top Chalk surface (1200-1600 m below the seafloor) was performed. The acquired seismic and geotechnical data together with deep boreholes were used for a geotechnical interpretation analysis to determine the elastic parameters of the sedimentary succession between the seabed and the Top Chalk surface.

2D dual seismic setup: All survey lines were acquired with a dual seismic setup focusing on the shallow and deep sections. The shallow sections were acquired with a relative low frequency seismic system, the deep sections with a high frequency multi-channel seismic system.

Specific scopes of the project was to estimate:

- Elastic and deformation parameters
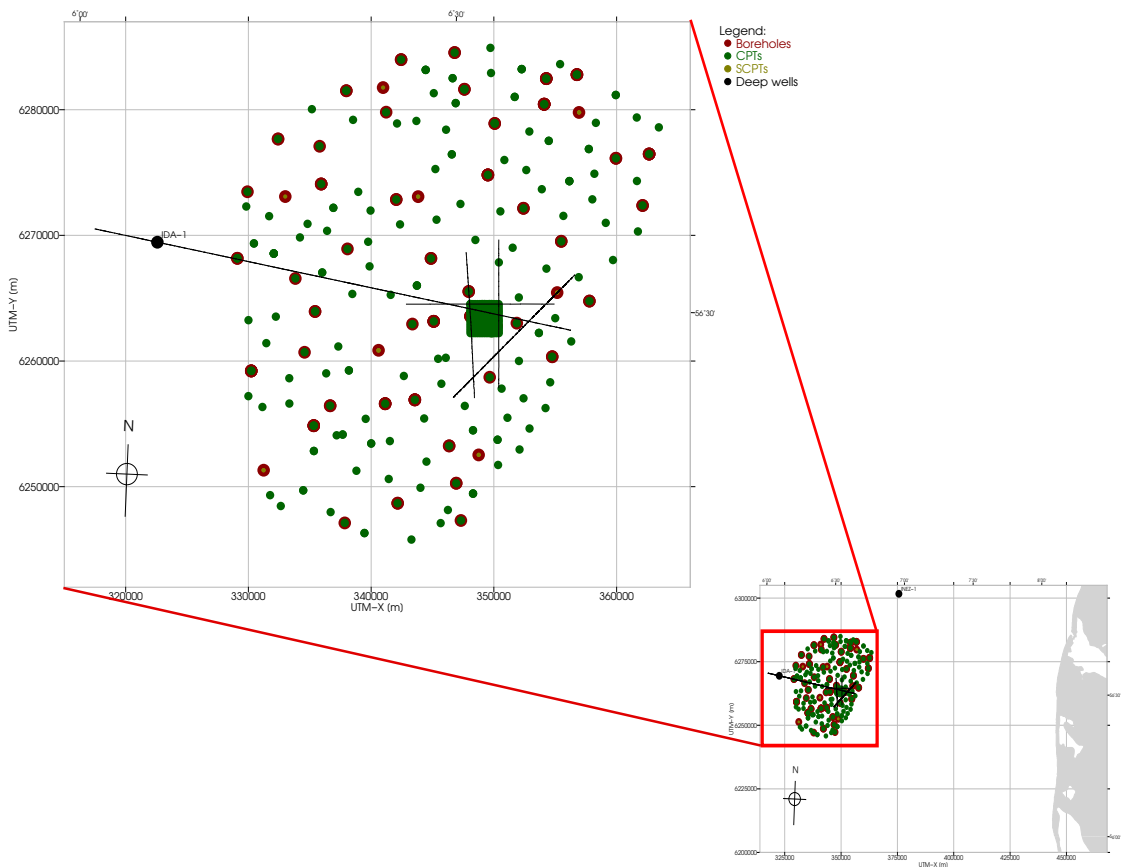
Figure 2.1: *Overview of the survey area and the avaible data for the analysis performed.*

Young's Modulus	Poisson's ratio	Bulk Modulus
Initial Shear Modulus	Density	

- Soil type classification

Sand	Sand with gas shows	Chalk
Clay	Lignite	Harder soils

- Pore pressure

Hydrostatic pressure	Pore pressure	Excess pore pressure

- CPT interpretation/Synthetic CPTs

  Cone resistance

10/341

2.3   Project overview

The following tests were available for the geotechnical and geological data evaluation:

- 280 seabed CPTs

- 3 downhole (deep) CPTs

- 12 S-CPTs

- 8 P-S loggings

- 12 sampling boreholes with associated laboratory testing

- 3 deep boreholes with measured p-wave velocity and gamma ray from around 300 meters and down

    - IDA-1 (on seismic 2D line)

    - Inez-1 (outside survey area)

    - Ibenholt-1 (outside survey area)

The above geotechnical data were acquired and delivered by Fugro and data from the 3 deep boreholes were acquired from the GEUS database.

A very high density of seabed CPTs (300-400 m offset between each location) was observed in the footprint of the Energy Island. This allowed a very detailed characterization of the top 20-35 m below seabed level. Below 35 m, there is limited data coverage as only three downhole CPTs are available. The direct measurement of the elastic properties of the soil with S-PCPT and P-S logging is only available for locations outside of the Energy Island footprint.

The following seismic data were available for analysis:

- High frequency seismic (Sparker system)

    - Total number of sections: 6

    - Samplerate: 0.1 ms

    - TWT range: 0.0 - 0.799 s

    - Associated RMS and interval seismic velocities were available

- Relative low frequency seismic (Airgun system)

    - Total number of sections: 6

    - Samplerate: 1 ms

    - TWT range: 0.0 - 2.799 s

    - Associated RMS and interval seismic velocties were available

The following 39 seismic horizons both in depth and time were analysed and used for the geotechnical parameter interpretation.

00 H00 SB	14 H70	26 Intra Gram PQ-04
01 H05	15 H71	27 Gram
02 H10	16 H72	28 Intra Lark 05
03 H20	17 HKSA	29 Intra Lark 04
04 H25_Te	18 H85	30 Intra Lark 03
05 H25	19 H90	31 Intra Lark 02
06 H30	20 HKSB	32 Intra Lark 01
07 H35	21 Intra Luna PQ-01	33 Lark
08 H38	22 Luna	34 Rogaland
09 H40	23 Intra Marbæk PQ-02	35 Ekofisk
10 H60	24 Intra Marbæk PQ-03	36 Maastrichtian
11 H61		37 CromerKnoll
12 H62	25 Marbæk	38 Kimmeridge
13 H69		

Chapter 3

Geological Setting

This chapter gives an overview of the geological setting above the Chalk in the Energy Island area. This chapter is primarily based on [Paul C. Knutz, 2022], [Rambøll, 2021], [Fugro, 2022] and [MMT, 2021].

The area of investigation goes from Seabed surface down to the Chalk surface. The shallow part consists of Quaternary sediments and are covered by the high frequency sparker seismic system and measured and described from multiple boreholes and CPTs. The deeper section down to the Chalk surface consists of Tertiary sediments and are covered by the lower frequency airgun seismic system and are measured and described by the deeper boreholes IDA-1, Ibenholt-1 and Inez-1.

3.1 Quaternary

The site underwent multiple glaciations during the Pleistocene, resulting in complex stratigraphic architecture. Pre-Pleistocene and Early Pleistocene sediments were glacio-tectonically deformed during the glaciations. The ice sheet during the Elsterian and Saalian glacial periods covered the site completely and eroded glacial valleys up to 350 m into older deposits, see Figure 3.1. The infill of these valleys includes sand, clay, and locally till. Deposits from the Saalian glacial landscape (Bakkeøer) are preserved in Jutland and the Danish Sector of the North Sea. Interglacial deposits consist of Holsteinian and Eemian marine sand and clay. During the Weichselian glacial period, till and glacio-tectonic deformation were found in the north of the site, while outwash plain deposits were found in the south. In the Late Weichselian to Early Holocene, marine transgression resulted in deposition in fluvial and estuarine environments. During the Holocene, the site was inundated by the North Sea and marine sands were deposited. An overview of the expected stratigraphy at the site can be found in Figure 3.2.
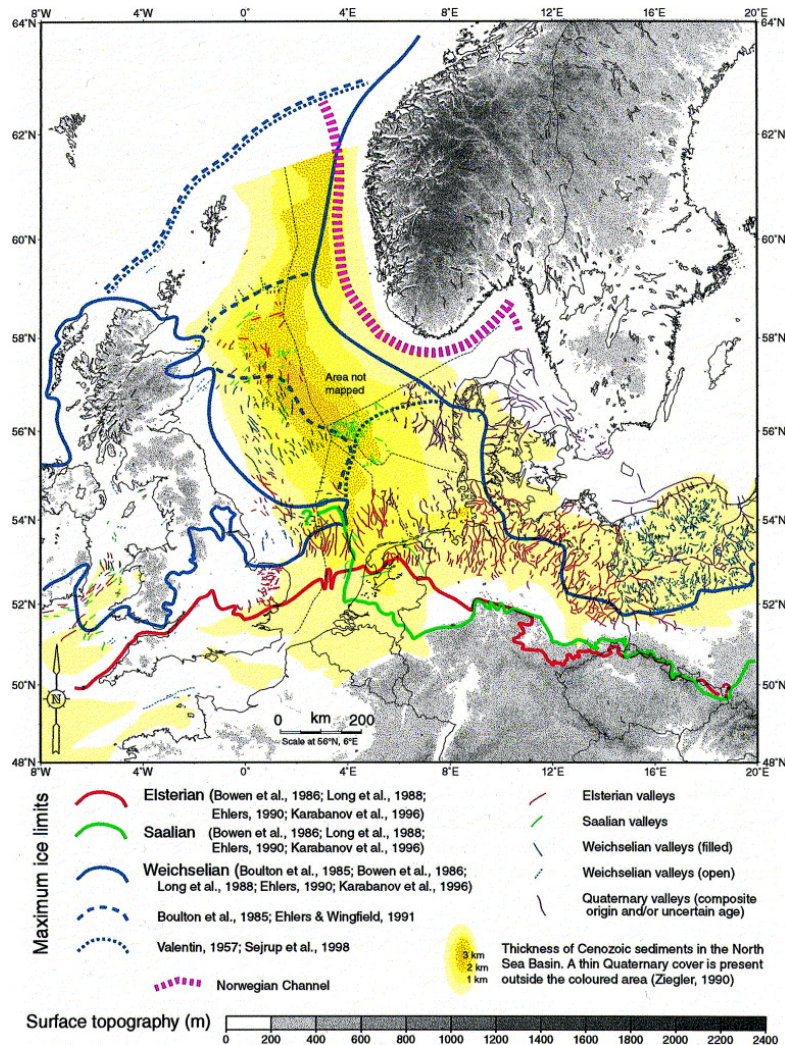
Figure 3.1: *Ice sheet extent and location of tunnel valleys of the three main glaciations (after [Huuse and Lykke-Andersen, 2000]).*

3.2 Tertiary

In the earliest Paleocene, the North Sea Basin was filled with mud rich in carbonate (as shown in Figure 3.4). This sedimentation pattern continued from the Late Cretaceous period and was partly due to a low input of clastic material from the Fennoscandian Shield and older Paleozoic massifs around the North Sea. During the Late Paleocene-Eocene, carbonate deposition stopped, and delta systems and associated submarine fans were deposited in the marginal areas around the Shetland Platform. Meanwhile, hemipelagic clays dominated most of the North Sea Basin, and there was limited incursion of clastic sediments from the Fennoscandian Shield, except for minor influx of glauconite-rich turbidites in the Late
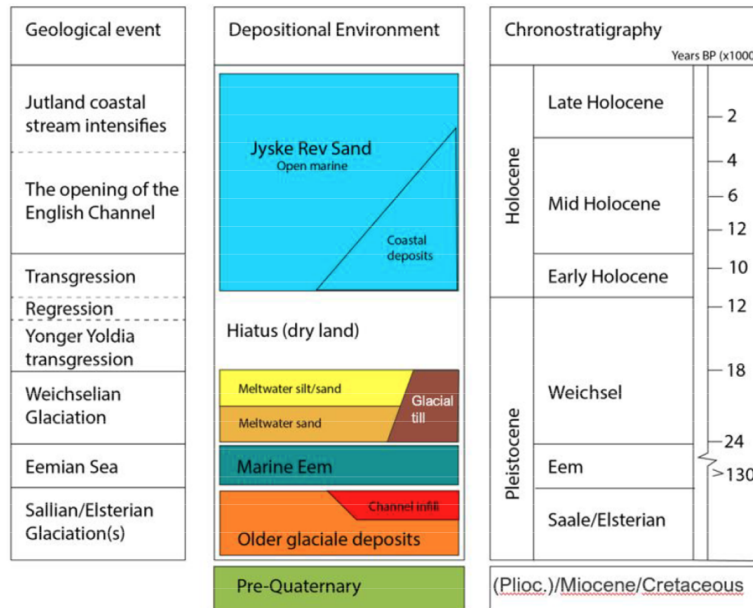
Figure 3.2: *Expected stratigraphy at the site (after [Paul C. Knutz, 2022] and [Rambøll, 2021]).*

Paleocene - Early Eocene. West of Norway, outbuilding of submarine fans occurred during the Late Paleocene - Eocene. Deltas continued to prograde from the Shetland Platform during the Oligocene, but there was a change in clastic input from Scandinavia. Sediment supply to the west of Norway became restricted, and the sediment was directed toward the south, where a delta-shelf system developed in the eastern North Sea Basin south of present-day Norway. In the northern North Sea adjacent to Scandinavia, almost pure clay was deposited, indicating very low input of coarse sediments to this area (as shown in Figure 3.4).

In the Early Miocene, distinct sand deposition characterized the northern North Sea, sourced from the Shetland Platform. In the eastern North Sea Basin, a marked progradation of a delta system began, sourced from southern Norway and central Sweden (as shown in Figure 3.3 and 3.5). During the Middle Miocene, marine mud deposition dominated the early phase of sedimentation, followed by sand deposition in the northern North Sea, while deposition of marine mud continued in the eastern North Sea Basin. In the Late Miocene, the eastern North Sea Basin was fully marine, with water depths of more than 100 m. The marine environment was predominated by hemipelagic settling of fine-grained sediments with some intercalation of distal tempestites composed of silt to fine-grained sand, referred to as the Gram Formation (as shown in Figure 3.3). During the latest Miocene, a fluviodeltaic depositional setting was established in the study area, and the shoreline migrated towards the southwest across the Ringkøbing-Fyn High area. The Marbæk and Luna Formations were deposited during this time (Figure 3.5).
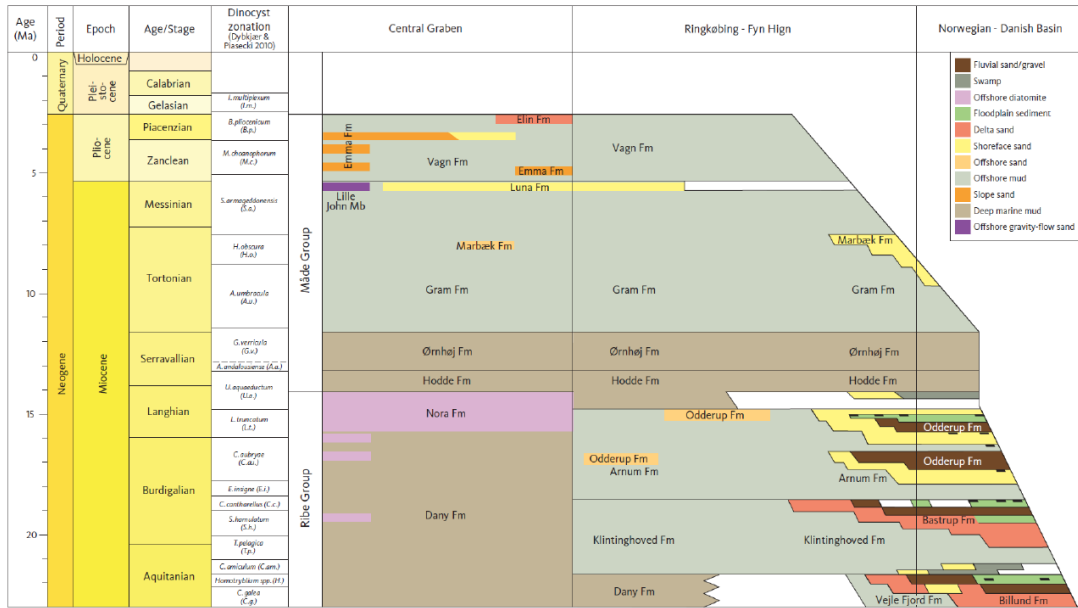
Figure 3.3: *Neogene lithostratigraphy and dinocyst zonation of the Danish sector [Paul C. Knutz, 2022].*
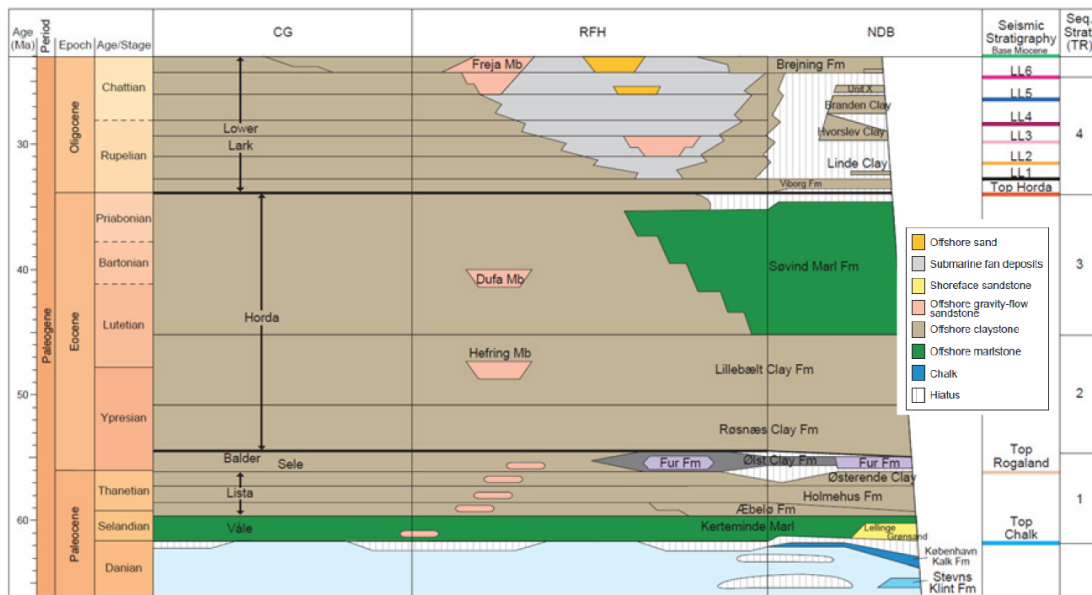
Figure 3.4: *Paleogene lithostratigraphy and dinocyst zonation of the Danish sector. CC, Central Graben. RFH, Ringkøbing-Fyn High. NDB, Norwegian-Danish Basin [Paul C. Knutz, 2022].*
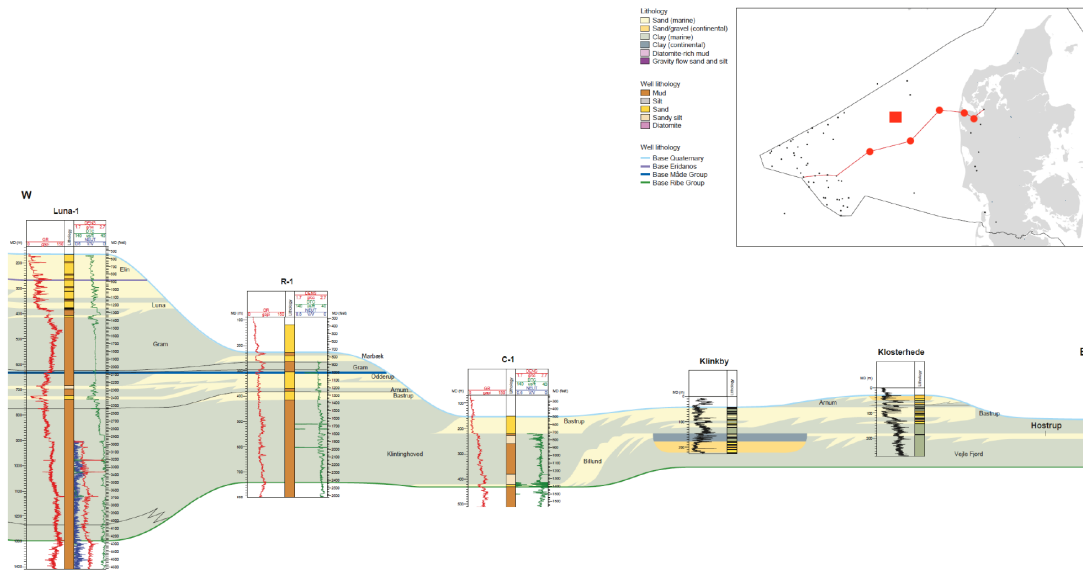
Figure 3.5: *West - East correlation panel showing the onshore - offshore correlations of the Neogene succession. The Neogene geology of the study area correspond to Gram and Luna formations between the Luna-1 and R-1 wells [Paul C. Knutz, 2022]. Wells displayed in section are highlighted with red circles on map. Approximate location of Energy Island area is highlighted with the red square on the map.*

In the Pliocene, strong subsidence resulted in resumed marine conditions in the Ringkøbing-Fyn High area, which was the result of sediment load (Eridanos Delta) in the southern North Sea Basin. During the latest part of the Pliocene, sediment supply from northeast (Fennoscandia) resulted in the reestablishment of a fluviodeltaic system in the Ringkøbing-Fyn High area, and during most of the Late Pliocene and Early Pleistocene, the area was land. A strong tilt of the pre-Quaternary and Early Pleistocene succession occurred at 1.1 million years before present.

3.3 Chalk surface

The Top Chalk layer has been surveyed in various investigative phases utilizing different generations of seismic data ([Vejbæk, 2007];[Huuse, 1999]). The Chalk surface is located at a depth of 1000-1200 meters beneath the AOI (Figure 3.6). To the north and east of the area, diapirs of Permian salt have uplifted the Chalk. The Chalk surface is evident on all seismic lines as a strong reflector. The Chalk surface marks the depth of investigation.
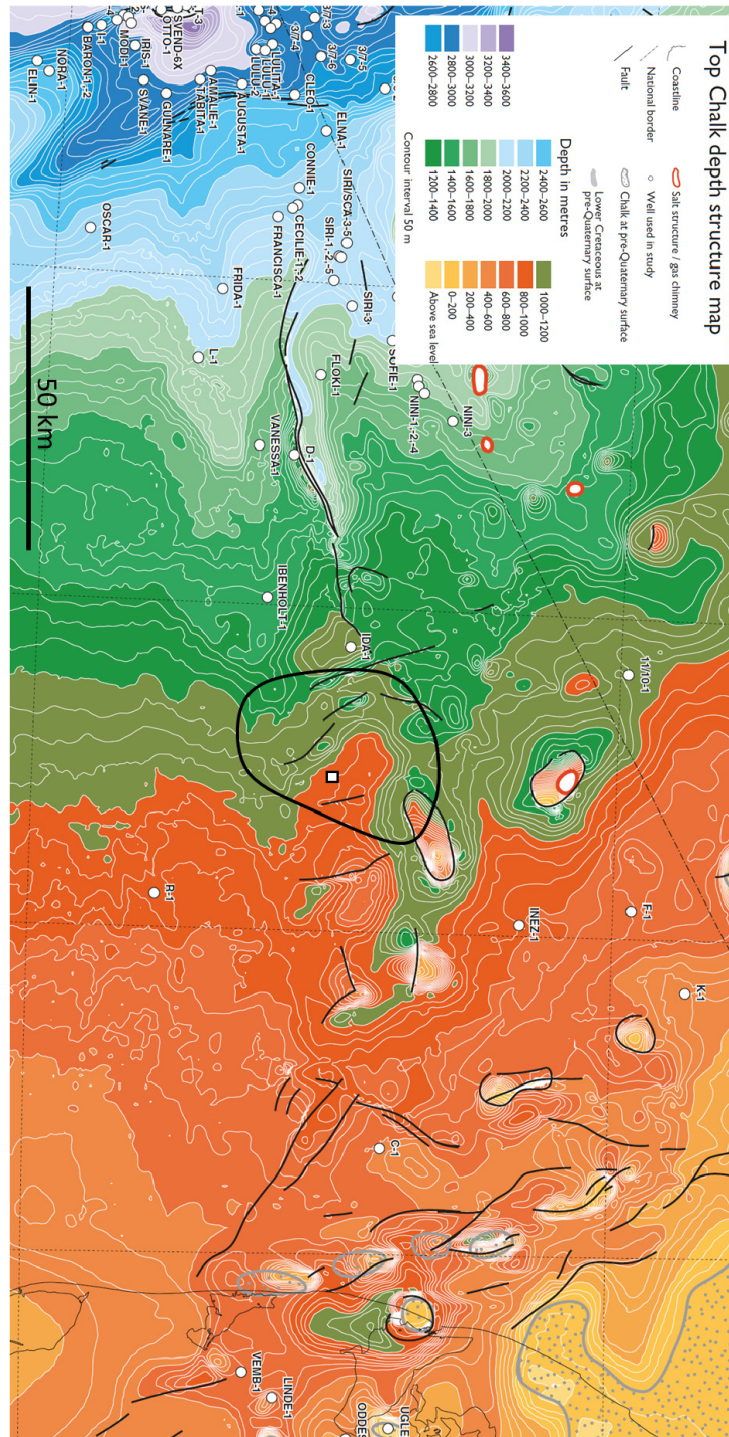
Figure 3.6: *Depth-structure map of the Top Chalk surface ([Vejbæk, 2007]). Concentric highs and associated faults structures demarcate salt diapirs causing uplift of the overlying succession. Proposed energy island area (AOI) and surrounding area designated for windfarms shown with white square and black polygon, respectively. [Paul C. Knutz, 2022].*

3.4 Layers

Following surfaces were used for the investigation of geotechnical parameters in the area. The layer definitions are in accordance with the definitions described in [Fugro, 2022] and [MMT, 2021].

Seabed	H69	Intra Gram PQ-04
H05	H70	Gram
H10	H71	Intra Lark 05
H20	H72	Intra Lark 04
H25	HKSA	Intra Lark 03
H25	H85	Intra Lark 02
H30	H90	Intra Lark 01
H35	HKSB	Lark
H38	Intra Luna PQ-01	Rogaland
H40	Luna	Ekofisk
H60	Intra Marbæk PQ-02	Maastrichtian
H61	Intra Marbæk PQ-03	CromerKnoll
H62	Marbæk	Kimmeridge

Chapter 4

Geotechnical data processing

This section of the report describes the geotechnical data processing performed to support the geophysical inversion for the Energy Island. At geotechnical borehole locations, the target properties of the inversion (shear wave velocity V_S, compression wave velocity V_P and bulk density ρ) can either be directly inferred from geotechnical measurements or indirectly derived through geotechnical correlations.

The relevant tests to determine V_S, V_P and ρ are discussed first and the available correlations for deriving them from the cone penetration tests (CPT) are presented in the next section. Subsequently, the available geotechnical data for the energy island project is presented and reviewed in the context of obtaining the required properties from the available geotechnical tests. The relevance of the proposed correlations is checked against the available data and example results which are fed to the geophysical modeling are presented.

4.1 Direct geotechnical measurement of elastic soil properties

4.1.1 Shear wave velocity V_S

Seismic CPT

As the CPT is a destructive test involving significant deformation of the soil, the stiffness at limited deformations cannot directly be derived from the CPT data. To allow direct measurement of the soil behavior at small strain using the same equipment as a conventional CPT test, two sets of additional accelerometer sensors (geophones) are placed on the cone rod to allow the detection of seismic waves. Seismic shear waves (S-waves) are then generated at the seabed using a seismic source placed at a known offset to the CPT rod. This setup is known as the S-PCPT (Seismic Piezocone penetration test) and is shown schematically in

Figure 4.1. The acceleration of the geophone sets is measured and by calculating the cross-correlation between the signals received at the upper and lower geophone, the difference in arrival time can be identified. When the offset between the two geophone sets is divided by the difference in arrival time, the seismic shear wave velocity V_S is obtained. The seismic shear wave velocity (V_S) has a direct relation to the small-strain shear modulus (G_{max}) when the bulk density of the soil (ρ) is known (Equation 4.1). It should be noted that the small-strain shear modulus can exhibit anisotropy [Wang and Mok, 2008] with differences between the value in horizontal and vertical direction. The S-PCPT test measures accelerations in both vertical and horizontal directions with the horizontal component being more relevant for pile-soil interaction. Furthermore, S-PCPT measurements near the seabed can be affected by noise due to the interference between surface waves and shear waves. To increase the accuracy of the S-PCPT, a system with dual geophones as described above, is preferred. Systems with a single geophone suffer more from noise as the arrival time of the shear wave needs to be selected from the noisy data. Despite the measurement uncertainty described above, the S-PCPT test is the most commonly used test to determine the small-strain shear modulus of the soil in-situ.

$$G_{max} = \rho \, V_S^2 \tag{4.1}$$

P-S logging

Although less frequently employed than S-PCPT testing, P-S logging is being performed to determine the seismic compression wave (P-wave) and shear wave (S-wave) velocity in an uncased borehole [Biringen and Davie, 2010]. This technique is especially useful in ground types where the CPT cannot penetrate (e.g. weak rock or very deep boreholes). A long probe is lowered into the borehole and consists of a seismic source which is acoustically separated from two geophone sets positioned on the probe at a given offset. When the source is activated, the time required for P- and S-waves to travel through the soil can be inferred from the measurements. Because both P- and S-wave velocity are recorded, information on bulk modulus (K) and shear modulus (G) can be obtained. P-wave velocity V_P is related to bulk and shear modulus as shown in Equation 4.2.

$$V_p = \sqrt{\left(K + \frac{4}{3}G\right)/\rho} \tag{4.2}$$

Bender element tests

Bender element testing employs the same principle as S-PCPT testing, the propagation velocity of S-waves is measured by assessing the travel time between a seismic source and a receiver. For bender element testing, a cylindrical sample is first saturated and then
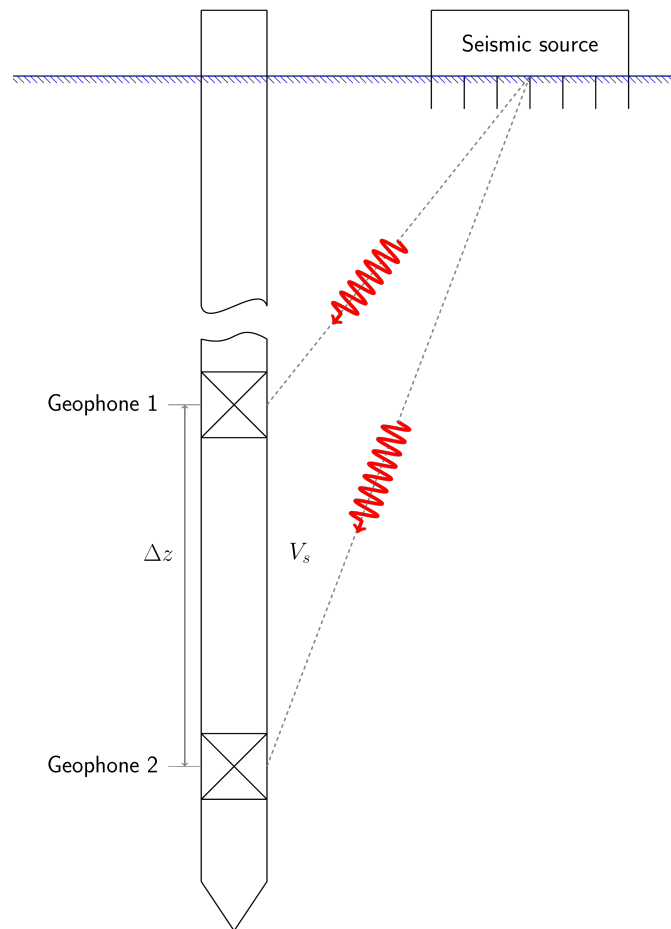
Figure 4.1: *Schematic representation of the S-PCPT test.*

consolidated to the in-situ stress conditions in a triaxial cell. Piezo-ceramic bender elements are inserted a the top and bottom of the sample to generate and receive S-waves. Specialized test setups also allow measurement of the S-wave velocity in the lateral direction by inserting bender elements at mid-height of the sample on diametrically opposite sides. Figure 4.2 shows a test setup which allows measurement in the vertical and lateral direction. Knowledge of the sample dimensions allows the S-wave velocities (and therefore G_{max}) to be calculated from the measured travel times. Identifying the time of first arrival can be challenging and the frequency of the input signal needs to be selected with care [Gomez and Stuyts, 2022]. Bender element testing is often combined with conventional drained or undrained (cyclic) triaxial testing.
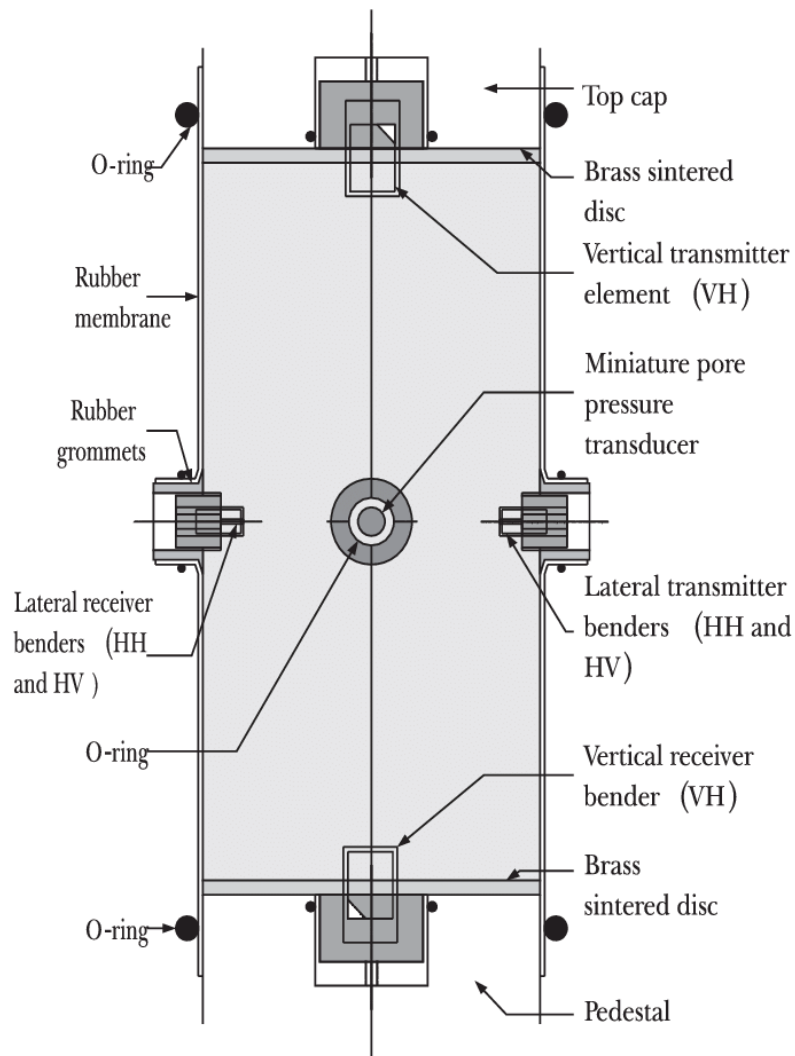
Figure 4.2: *Test setup for a bender element test on a triaxial specimen with vertical and lateral receivers [Nash et al., 2007].*

Resonant column tests

Soil plasticity starts developing as soon as irreversible movements of soil particles relative to each other manifest themselves. The shear modulus degrades from the maximum value at small strains as soon as soil strains exceed this threshold. To measure the degradation of shear modulus with increasing strain levels, the resonant column device (Figure 4.3) can be used. A fixed-amplitude cyclic torsional loading is applied to the soil for various frequencies. The frequency at which the sample responds with the maximum strain is called the resonance frequency. The shear strain in the sample can be calculated from the magnitude of the resonance peak and the resonance frequency allows the shear modulus corresponding

to this strain to be identified. The resonant column test also allows the determination of the soil damping as a function of shear strain. For a full description of the test, reference is made to [Keene et al., 2017]. The resonant column test is used in practice to determine the small-strain stiffness and to provide input to advanced constitutive models employed in 3D finite element analysis (FEA).

4.1.2 Acoustic wave velocity V_P

The only geotechnical test which is routinely used for P-wave velocity measurement is P-S logging (Section 4.1.1). In onshore practice, cross-hole testing is also used but this is not practically feasible in the offshore environment.

4.1.3 Bulk density ρ

The unit weight of soil can be determined directly by filling a proofing ring of known volume with soil and determining its mass. The bulk density ρ of the soil grains and the pore water contained in the void space is obtained by dividing the mass contained in the ring by the rings internal volume. The bulk unit weight γ is obtained by multiplying the bulk density ρ by the acceleration of gravity g as shown in Equation 4.3. This test is carried out offshore, immediately after sample extrusion to ensure that the pore water does not drain from the sample.

$$\rho = m_{\text{inside ring}}/V_{\text{ring}}$$
$$\gamma = \rho \cdot g \tag{4.3}$$

The unit weight can also be obtained indirectly from the water content of a specimen of soil. A specimen of arbitrary volume is weighed before and after drying at 105°C for 24 hours. The total mass before the test is composed of the mass of the solid grains W_s and the mass of the pore water W_w. After the test, only the mass of the solid grains remains. The water content is then expressed as the ratio of the weight of water to the weight of solids. Phase relations can be used to determine bulk unit weight from the water content. The void ratio e which is the ratio of the volume of voids to the volume of solids is completely filled with pore water for saturated offshore soils ($S = 1$). The void ratio is thus equal to the water content multiplied by the specific gravity G_s, the ratio of the weight of the soil grains to the weight of water of equal volume. This leads to the relation between bulk unit weight γ and water content (Equation 4.4). Note that the specific gravity of the soil needs to be known. G_s is typically taken equal to 2.65 but can be determined with a pycnometer test for coarse-grained soil.
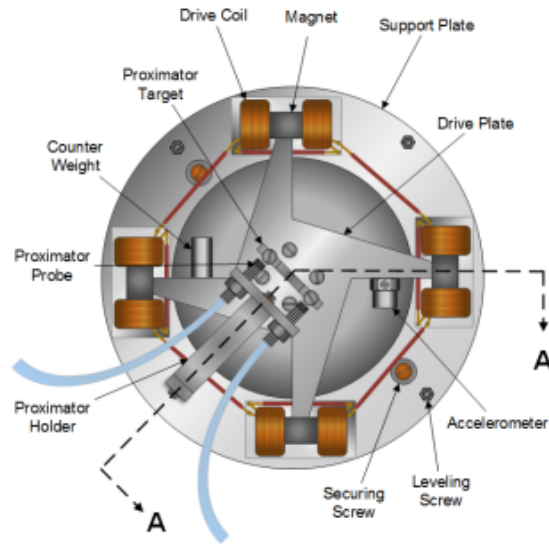
a) Top View of Drive and Monitoring Systems (LVDT is Removed for Clarity)
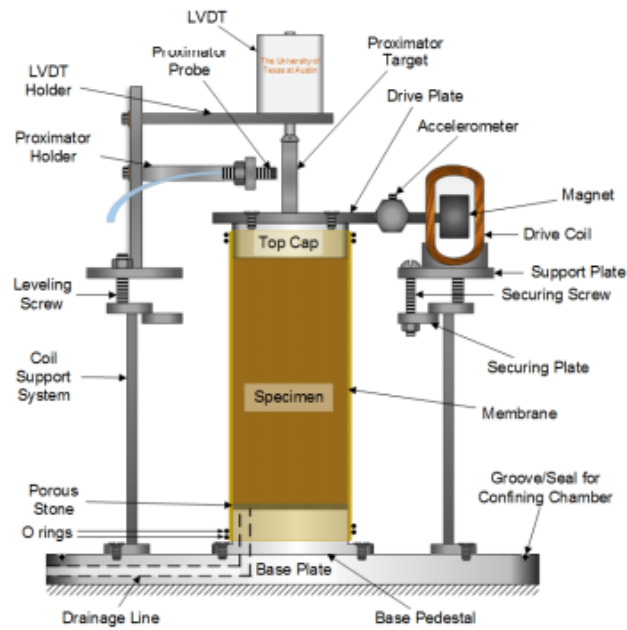
b) Section AA Showing Soil Specimen in RCTS Set-Up

Figure 4.3: *Test setup for a resonant column test on a triaxial specimen [Keene et al., 2017].*

25/341

$$w = \frac{W_w}{W_s}$$
$$S \cdot e = w \cdot G_s \tag{4.4}$$
$$\gamma = \frac{W}{V} = \left(\frac{G_s + S \cdot e}{1 + e} \right) \cdot \gamma_w$$

4.2 Indirect geotechnical determination of elastic soil properties

4.2.1 CPT-based correlations for V_S

As the direct measurement of shear wave velocity is operationally more difficult and costly than performing a conventional CPT test, correlations were sought which link shear wave velocity V_S or small-strain shear modulus G_{max} with CPT measurements.

Robertson & Cabal [Robertson and Cabal, 2015] formulated a widely used correlation for shear wave velocity based on soil behavior type index as shown in Equation 4.5. Unfortunately, the authors do not present the background data used for the calibration of the correlation. Although the vertical total stress is used in the formula for shear wave velocity, the correlation does not have an explicit dependence on the vertical effective stress.

$$V_S = [\alpha_{vs}(q_t - \sigma_{vo})/P_a]^{0.5}$$
$$\alpha_{vs} = 10^{0.55 \cdot I_c + 1.68} \tag{4.5}$$

Cha et al [Cha et al., 2014] published a framework which explicitly captures the stress-dependence of the small-strain shear modulus. The effective stress in the direction parallel to shear wave propagation ($\sigma'_\parallel$) and the direction perpendicular to the wave propagation ($\sigma'_\perp$) are considered. The authors proposed a dependence of the coefficients α and β on the compression index of the soil material by investigating results from an oedometer test setup equipped with bender elements.

The compression index needs to be known for this relation to be applied. It should be noted that C_c also has a stress dependence. Data on the compression index is only available from a limited amount of tests which are generally only performed on samples from cohesive layers. Therefore, an alternative formulation of the calibration coefficients α and β was sought in which these vary linearly with soil behavior type index I_c (Equation 4.6). The advantage of this equation is that it has an explicit dependence on the effective stress conditions.

$$V_S = \sqrt{\frac{G}{\rho}} = \alpha \left(\frac{\sigma'_\perp + \sigma'_\parallel}{2 \text{ kPa}}\right)^\beta$$

$$\text{where } \alpha = 2.4031 - 0.1986 \cdot I_c$$
$$\text{and } \beta = 0.0758 + 0.0627 \cdot I_c$$

(4.6)

4.2.2 Relation between bulk modulus K, shear modulus G and V_P

The theory of elasticity dictates that a relation exist between V_S, V_P and ρ and bulk modulus K, shear modulus G and Poisson's ratio ν (Equation 4.7). These equations can be used to derive compression wave velocity from shear wave velocity when a valid choice of Poisson's ratio ν is made.

$$V_P = \sqrt{\frac{K + \frac{4}{3} G}{\rho}}$$

$$V_S = \sqrt{\frac{G}{\rho}}$$

$$\implies V_P = \sqrt{\frac{K + \frac{4}{3} \rho V_S^2}{\rho}}$$

$$\text{and } K = \frac{2G(1+\nu)}{3(1-2\nu)} = \frac{2\rho V_S^2(1+\nu)}{3(1-2\nu)}$$

(4.7)

4.2.3 CPT-based correlation for bulk density

A correlation between unit weight γ and CPT measurements is proposed by Mayne et al. [Mayne et al., 2010]. The correlation from Equation 4.8 is derived for several soil types (sand, soft clay and stiff clay) but does not apply for cemented soils. It should be noticed that the correlation shows significant scatter between unit weight measurements and values derived with the correlation. An error band of $\pm 2 \text{kN/m}^3$ encompasses the data quite well.

$$\gamma = 1.95 \cdot \gamma_w \cdot \left(\frac{\sigma'_{vo}}{P_a}\right)^{0.06} \cdot \left(\frac{f_t}{P_a}\right)^{0.06}$$

$$\text{where } \gamma = \rho \cdot g$$

(4.8)

4.3 Review of available geotechnical data

4.3.1 Relevant geotechnical tests

The footprint of the Energy Island and the surrounding wind farm zone has been subjected to an extensive site investigation. The available geotechnical test locations are shown in Figure 4.4.

The following tests were available for the geotechnical data evaluation:

- 280 seabed CPTs

- 3 downhole (deep) CPTs

- 12 S-PCPTs

- 8 P-S loggings

- 12 sampling boreholes with associated laboratory testing

A very high density of seabed CPTs (300-400m offset between each location) was observed in the footprint of the Energy Island. This allowed a very detailed characterization of the top 20-35m below seabed level. Below 35m, there is limited data coverage as only three downhole CPTs are available.

The direct measurement of the elastic properties of the soil with S-PCPT and P-S logging is only available for locations outside of the Energy Island footprint. As such, correlations are required to derive the elastic properties for the geotechnical test locations inside the Energy Island footprint.

The geological structure of the site can be revealed by plotting the cone tipe resistance from the CPT tests on a profile line through the Energy Island. This profile line is selected along one of the geophysical profile lines and is shown in Figure 4.5. Locations in a 200m search band around the profile line are selected and the cone tip resistance is projected onto the profile line and scaled to reveal geotechnical trends. The two stratigraphic profiles are also plotted in Figure 4.6.

The geotechnical profile shows a relatively homogeneous site in terms of cone tip resistance with gradual variations of the CPT traces from west to east. The data shows a surface layer of sand with high cone resistance overlying a layer of silty sand with variable thickness. A clay layer of variable thickness, characterized by low cone resistance is found below the silty sand. Underneath the clay, a layer of very dense sand with high cone resistance is again observed. The only deep CPT along the profile line is BH-006 and this deep CPT test reveals the presence of a thicker clay layer (>30m thickness) below the very dense sand.

Although the geotechnical conditions in the wind farm area are relatively homogeneous, the variable thickness of the clay layer could lead to differential settlements after constructions.
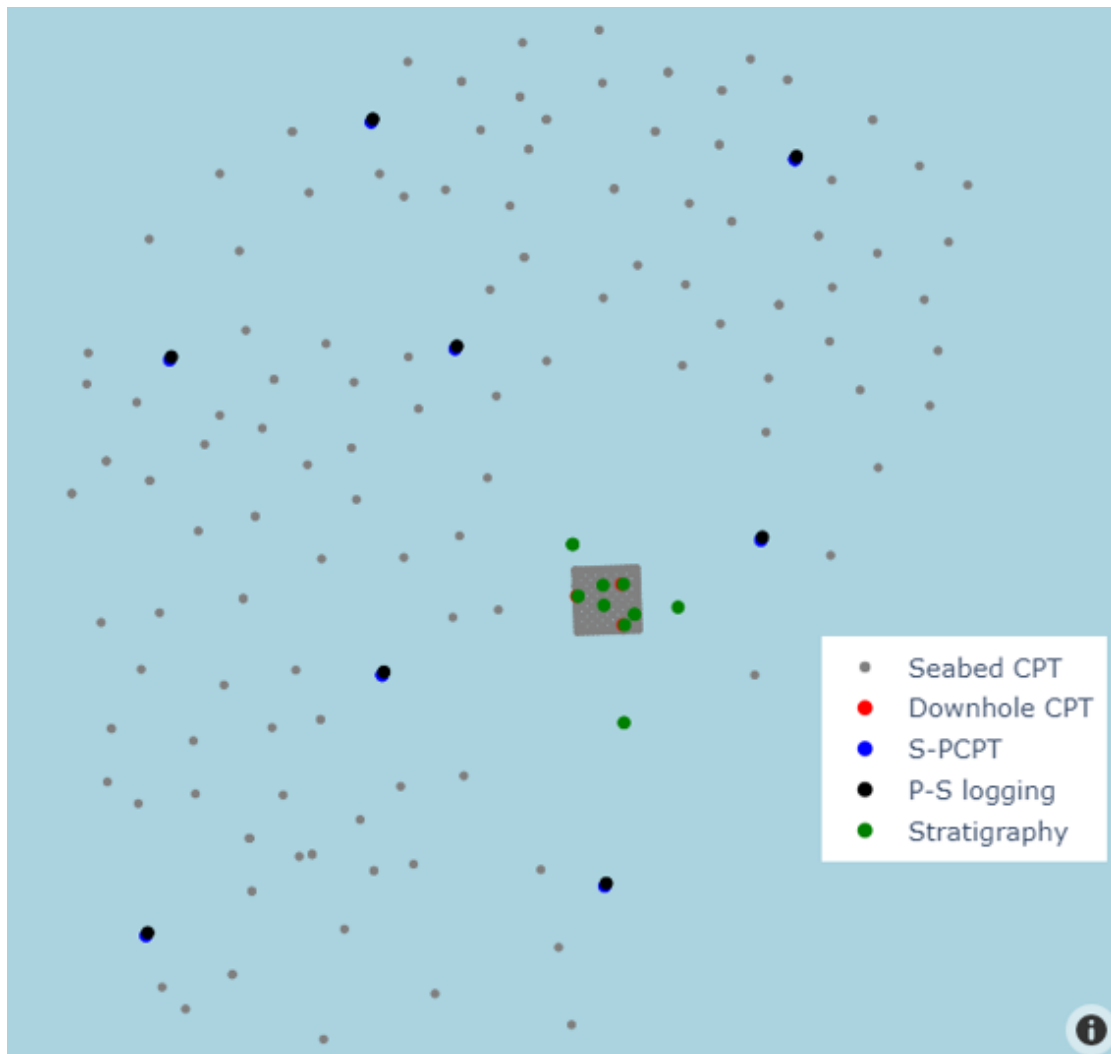
Figure 4.4: *Overview of available geotechnical testing locations.*

Characterizing the thickness of this clay layer accurately (also in between available geotechnical boreholes) is one objective of the inversion modeling. For deeper clay layers which are not revealed by the relatively shallow seabed CPTs, the inversion provides a mean to characterize the thickness quantitatively.

4.3.2 QA/QC on elastic geotechnical properties

The elastic geotechnical properties are available for 8 locations with S-PCPT and P-S logging and the consistency between both data sources was checked. Practically, this is only possible for V_S as S-PCPT tests do not provide reliable V_P estimates. For the depths where
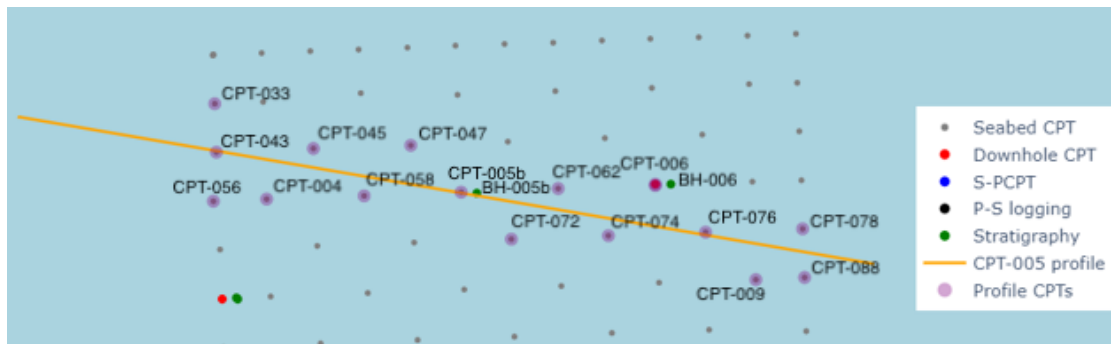
Figure 4.5: *Plan view of a profile line crossing the Energy Island footprint and the selected locations for plotting. Data highlighted are represented in Figure 4.6*
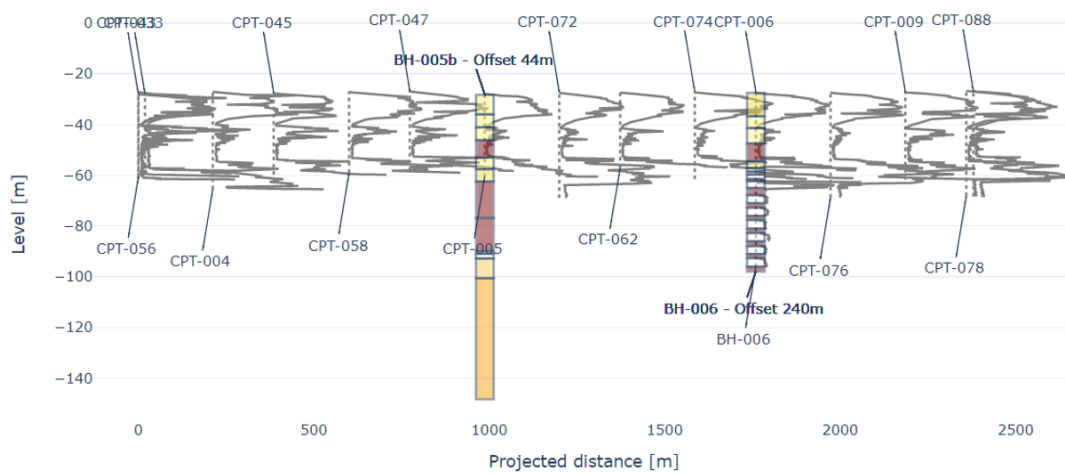
Figure 4.6: *Geotechnical data projected onto the CPT-005 profile line (Figure 4.5) through the Energy Island area.*

S-PCPT and P-S logging results overlap, their consistency can be checked. An example is shown in Figure 4.7 which is the location with the deepest S-PCPT penetration. For the other locations with S-PCPT and P-S logging, the S-PCPT data terminates at a shallower depth, resulting in limited overlap between S-PCPT and P-S logging data.

Figure 4.7 also shows that V_S from P-S logging is available in both normal and complementary direction. The data from those two orientation appears to be very consistent. Therefore, the normal V_S data from P-S logging was used for further QA/QC.

For every V_S data point from S-PCPT, a corresponding P-S logging measurement was sought and the measurements were plotted in Figure 4.8. If both measurements would correspond perfectly, all data would plot on the black dashed line. This is clearly not the case for the Energy Island tests. V_S from P-S logging appears to be consistently lower
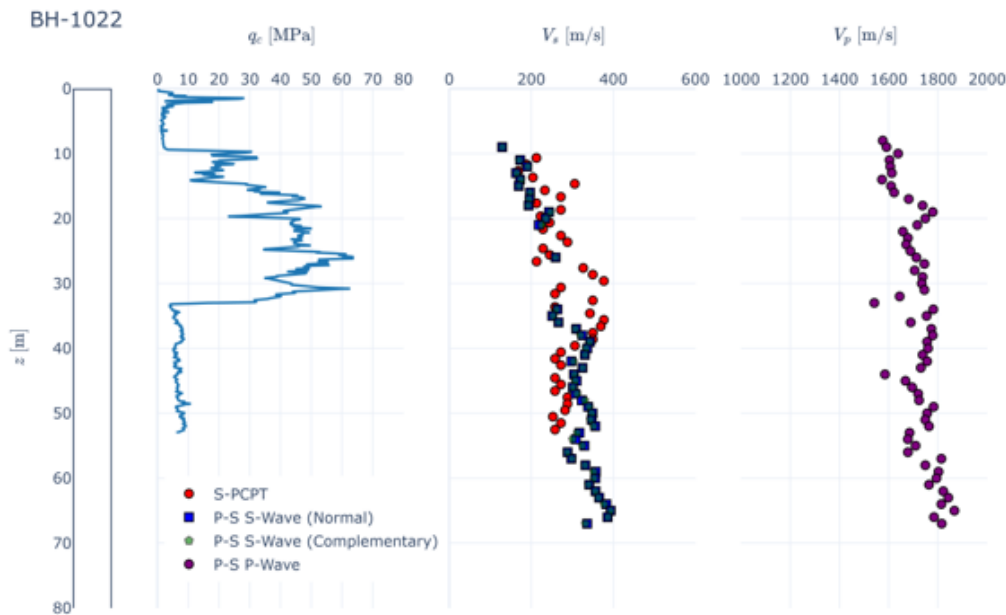
Figure 4.7: *Cone tip resistance q_c, shear wave velocity V_S and compression wave velocity V_P at location BH-1022.*

than V_S from S-PCPT, except for data in the deeper clay at location BH-1022 (below 32m in Figure 4.7). The probable causes of this are stress relaxation in cohesionless soils due to borehole drilling. As V_S is stress-dependent, a lower effective stress between the grains would also lead to a reduction in shear wave velocity. Insertion of the CPT rod, on the other hand, leads to a stress increase and therefore a higher V_S. In cohesive soils, the borehole wall is autostable, an such relaxation is not going to occur to the same extent, which could explain the different result for BH-1022.

4.3.3 Applicability of proposed correlations

Stress-dependent V_S correlation

Based on the available data, the applicability of the proposed correlations can be checked. Figure 4.9 and 4.10 show the comparison between the V_S estimates with the CPT-based correlations by Robertson & Cabal [Robertson and Cabal, 2015] and the stress-dependent correlation. A coefficient of lateral earth pressure K0=1 was used to establish the relation between horizontal and vertical effective stress in the soil
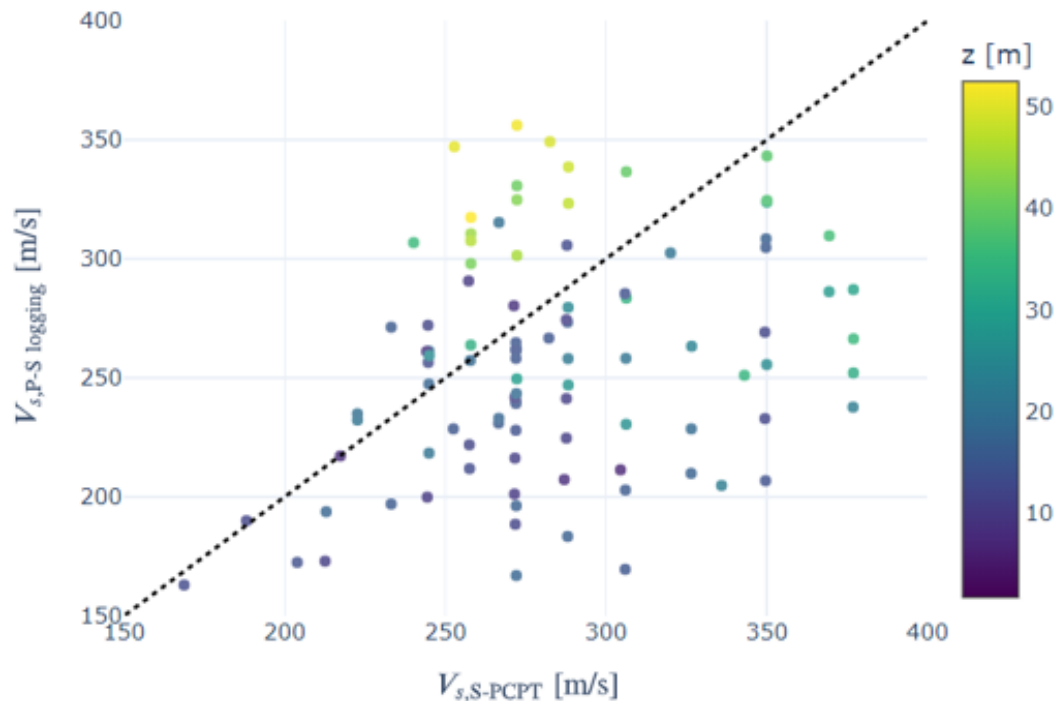
Figure 4.8: *Comparison between V_S from S-PCPT and P-S logging. The data is color-coded according to depth.*

The comparison is made for the S-PCPT and PS logging data. The data for the Energy Island site is color-coded according to soil behavior type index I_c. Soil behavior type index >2.7 indicates cohesive behavior, $I_c < 2.5$ indicated cohesionless behavior. The gray dots in the chart are measurements for other sites in the southern North Sea. This data indicates whether the data collected at the Energy Island site conforms with the data collected at other North Sea sites. The shaded blue area indicates a $\pm30\%$ error band.

The results indicate that the stress-dependent correlation leads to less scatter in the prediction. The predictions for this correlation are unbiased for the S-PCPT data but for the PS logging data, a bias towards overprediction of V_S is noticed. As mentioned before, this bias can be due to stress-relaxation from borehole drilling, leading to lower V_S measurements with PS logging. The correlation by Robertson & Cabal leads to greater scatter with a significant number of points lying outside the blue $\pm30\%$ uncertainty band. The bias towards overprediction of V_S from PS logging is also noticed for this correlation.

Based on the observations above, the stress-dependent correlation is used to infer V_S at locations where only CPT data is available.
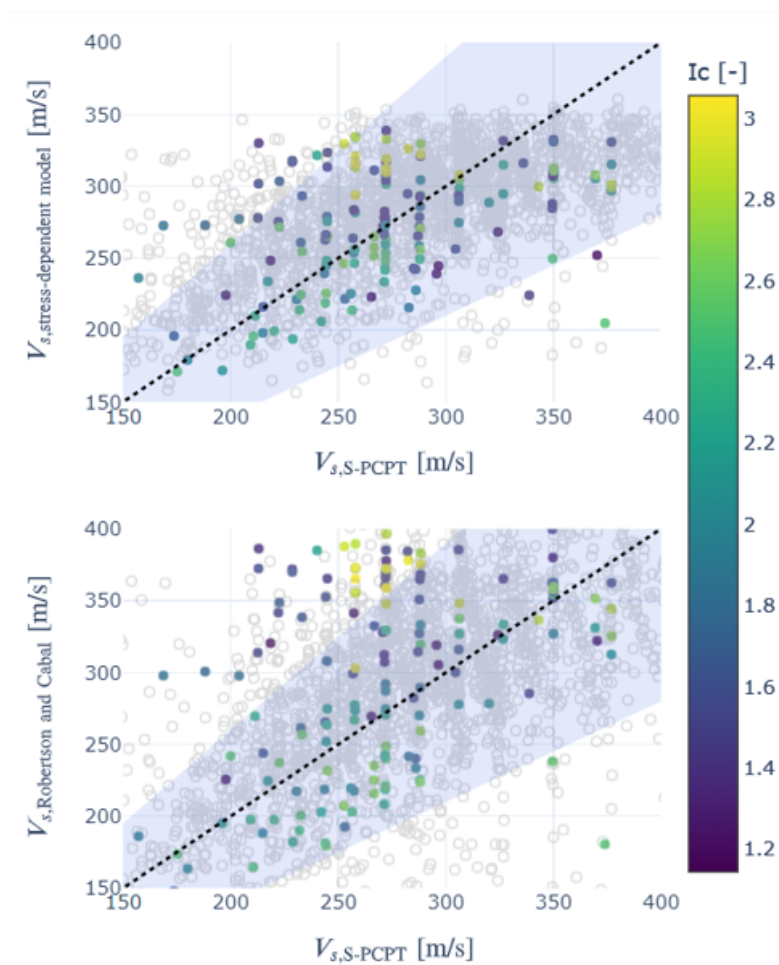
Figure 4.9: *Comparison between V_S estimates with CPT-based correlations and V_S measurements with S-PCPT.*

Correlation for V_P

The literature does not propose any correlations between V_P and CPT measurements. The formulae proposed in Equation 4.2 rely on a selection of Poisson's ratio ν. Poisson's ratio typically ranges from 0.2 to 0.5 (where ν=0.5 means fully incompressible behavior). A meaningful fit to the data could not be identified with a Poisson's ratio in this range. After inspection of the relation between V_S and V_P in Figure 4.11, a mathematical formula was fitted to the data. This formula is proposed in Equation 4.9 and is shown in Figure 4.11 as the dashed black line.

$$V_P = 1200 + 6.5 \cdot V_S^{0.75} \tag{4.9}$$
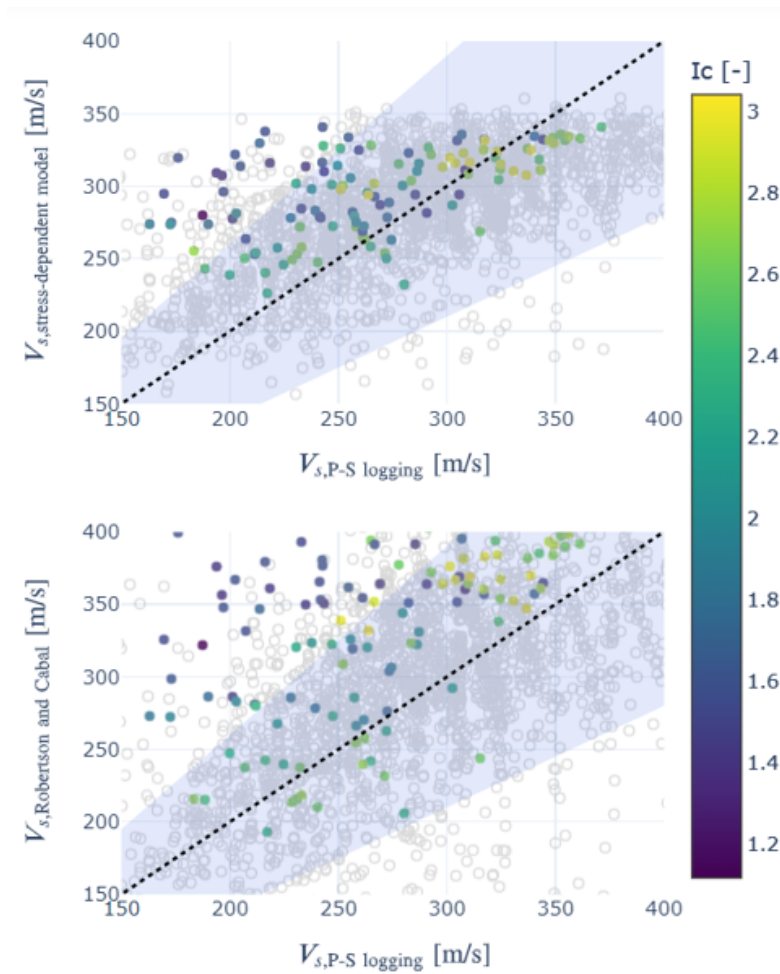
Figure 4.10: *Comparison between V_S estimates with CPT-based correlations and V_S measurements with P-S logging.*

Estimates of V_P are obtained by first estimating V_S from the CPT data using the stress-dependent correlation from Equation 4.6 and then applying Equation 4.9. It should be noted that this adds transformation uncertainty (the uncertainty when obtaining an estimate of a soil parameter indirectly) two times. Figure 4.12 shows the transformation uncertainty when obtaining V_P indirectly. The top panel shows the scatter when V_S from PS logging is transformed to V_P. The data shows a slight bias towards underprediction and all data is contained in a $\pm 10\%$ uncertainty band. The bottom panel shows how V_P estimated from CPT data (by first calculating V_S) compares to the measured V_P values. The data is also contained in the $\pm 10\%$ uncertainty band but it should be noted that the estimate of V_P is almost always contained between 1600 and 1700m/s. The low V_P, there is a tendency towards overprediction and for high V_P, a tendency towards underprediction.
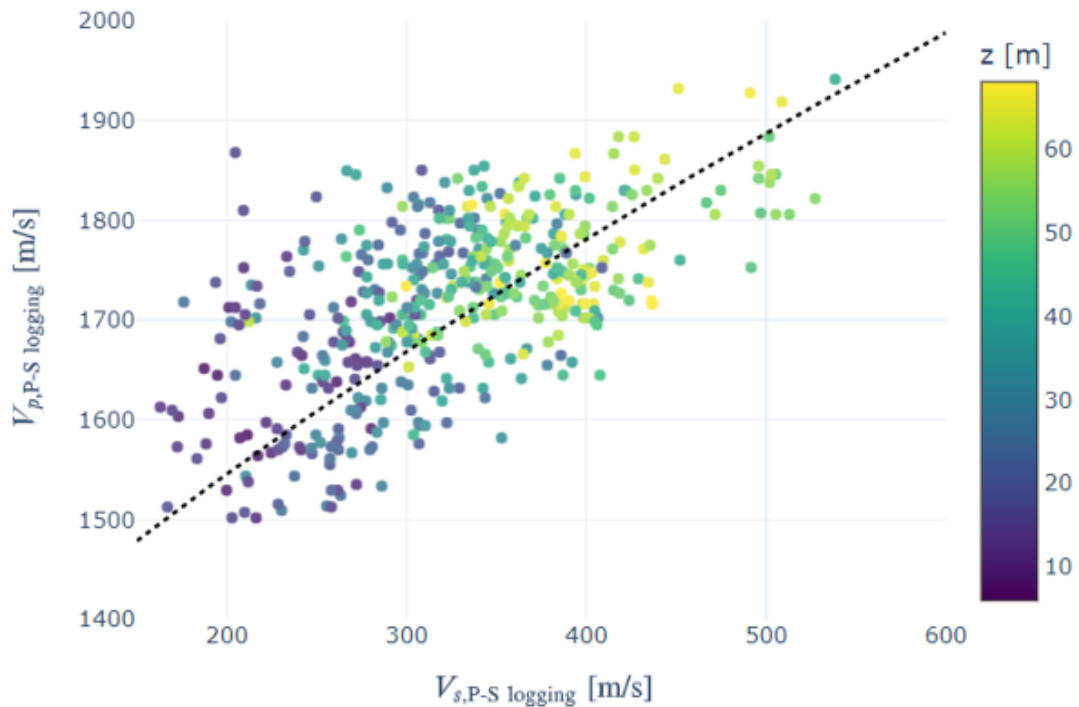
Figure 4.11: *Correlation between V_S and V_P data from P-S logging. The data is color-coded according to depth. The fitted relation is shown as a dashed black line.*

Given that all data is contained in the $\pm10\%$ uncertainty band, V_P is calculated at all CPT locations by first estimating V_S using Equation 4.6 and then applying Equation 4.9.

Unit weight correlation

The unit weights measured from the offshore samples can be compared to unit weight estimates using the correlation by Mayne et al. [Mayne et al., 2010]. Figure 4.14 shows the scatter on the estimate of unit weight when using the correlation from Equation 4.8. It should be noted that the coefficient of 1.95 was divided by 1.05 to obtain an unbiased estimate of unit weight.

The uncertainty on the unit weight estimate is shown in Figure 4.14. Most of the data falls within a $\pm15\%$ uncertainty band.

Given that unit weight data shows a significant amount of measurement uncertainty, the correlation by Mayne et al. is retained for calculating the unit weight, with an adjustment to the multiplier as shown in Equation 4.10. The density is easily obtained from the unit weight by multiplying it with the acceleration of gravity (g=9.81m/s^2).
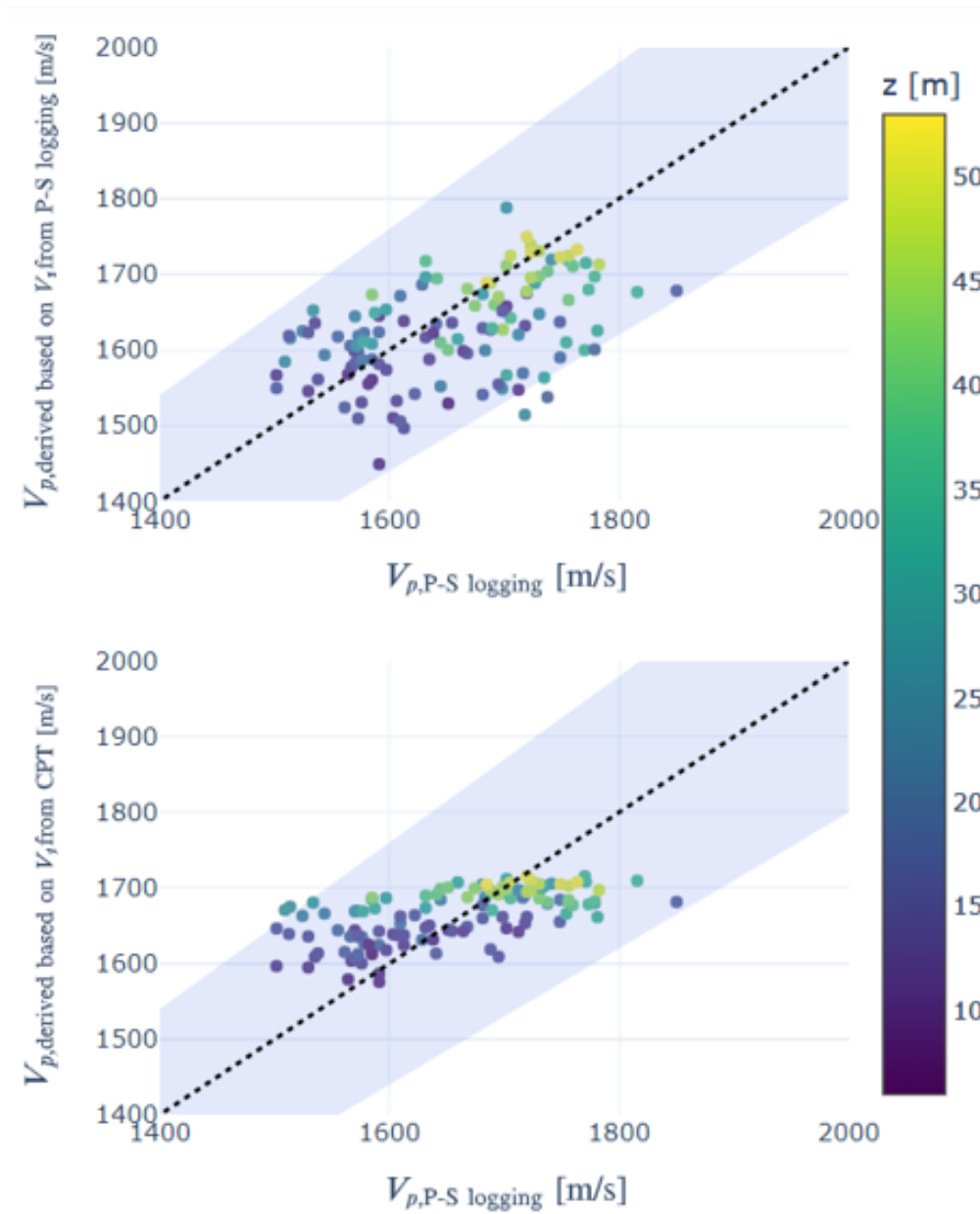
Figure 4.12: *Comparison between directly measured V_P and V_P from correlation with V_S data.*
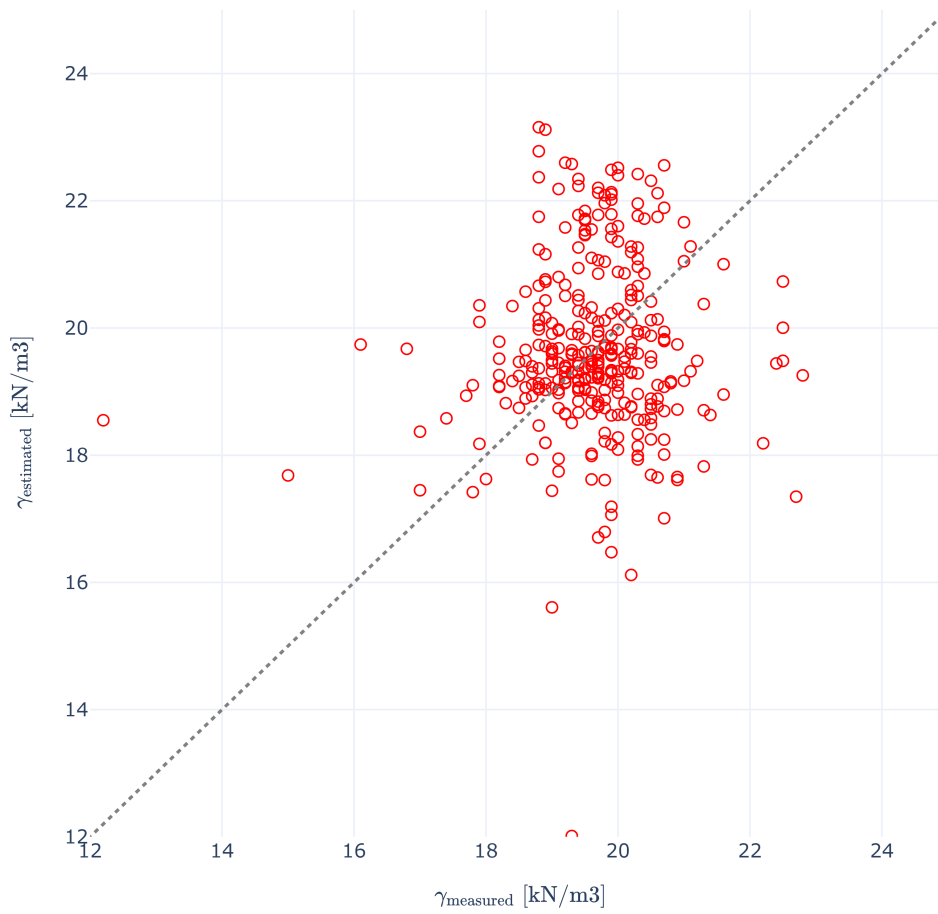
Figure 4.13: *Comparison of measured and estimated unit weight with the correlation by Mayne et al [Mayne et al., 2010].*
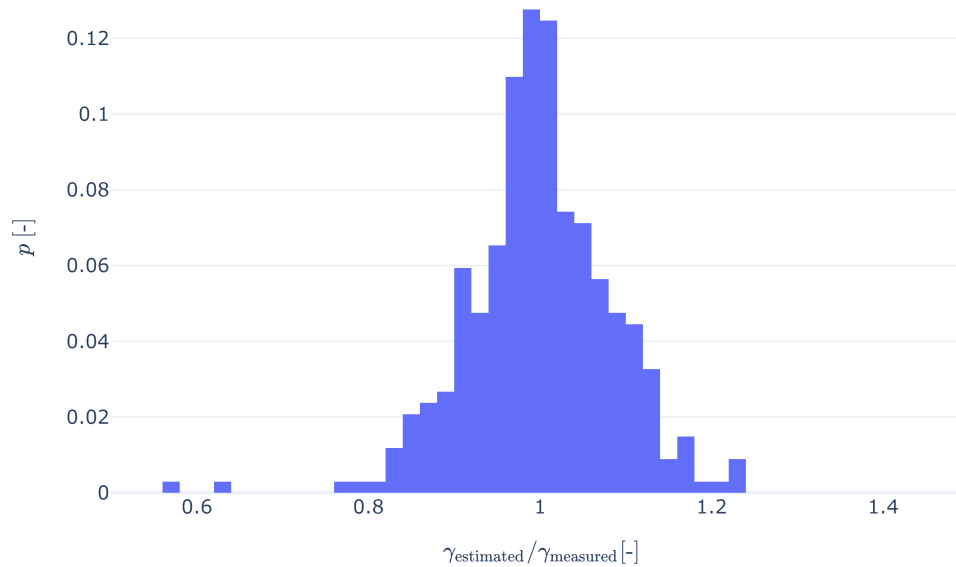
Figure 4.14: *Histogram of the ratio of estimated to measured unit weight.*

$$\gamma = \frac{1.95}{1.05} \cdot \gamma_w \cdot \left(\frac{\sigma'_{vo}}{P_a}\right)^{0.06} \cdot \left(\frac{f_t}{P_a}\right)^{0.06}$$

$$\text{where } \gamma = \rho \cdot g$$

(4.10)

4.4 Derivation of elastic soil properties for use in inversion model

With the relations for establishing V_S, V_P and ρ being defined, elastic properties can be calculated at all CPT locations. This operation was performed for all CPTs within the Energy Island footprint and the surrounding offshore wind farm area. An example of the estimates of V_S, V_P and γ is shown for location BH-1032 in Figure 4.15. This location is presented as there are also direct measurements of V_S and V_P available there. The calculated properties (in yellow) show good agreement with the direct measurements. No unit weight data was available at this location, so only the modeled relation is shown.

An example of the modeled unit weight compared to measurements for location BH-015 (where direct measurements of unit weight are available) is shown in Figure 4.16. The data
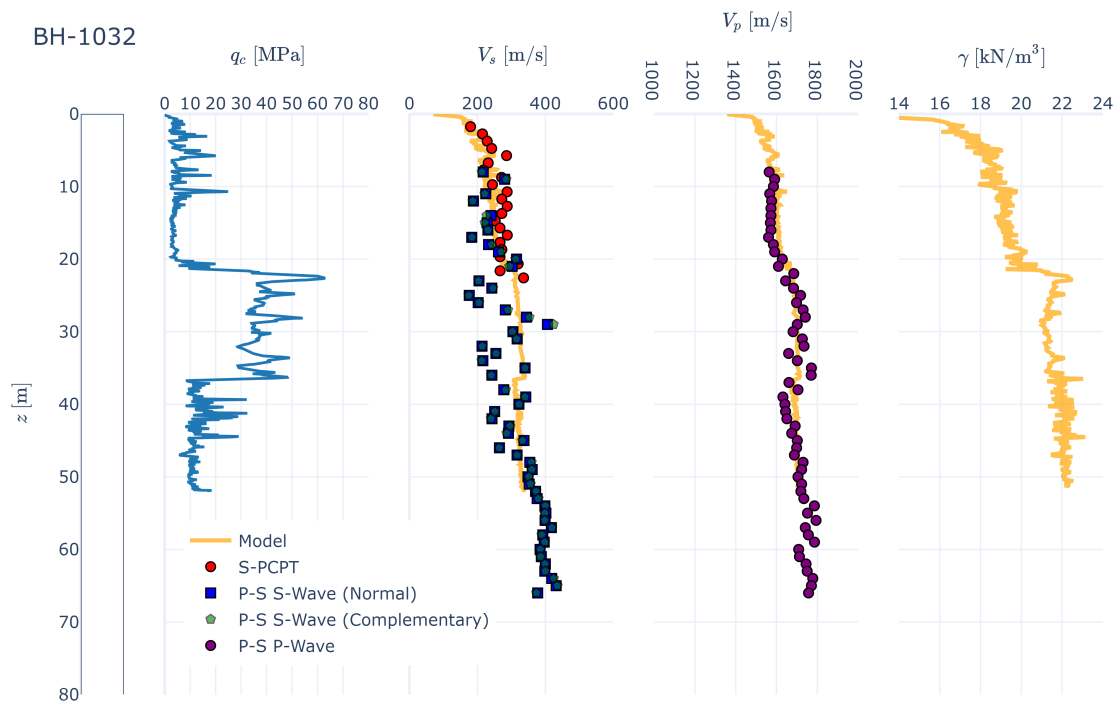
Figure 4.15: *Derived V_S, V_P and unit weight at location BH-1032 where elastic soil property data is available. Unit weight data is not available at this location so only the modeled unit weight is shown.*

shows reasonable agreement with the trend. An underestimation of unit weight is noticed for the upper 3m and an overestimation in the dense sand layer below 25m.

4.5 Conclusions

The report outlines the estimation of elastic soil properties from the available geotechnical tests in the Energy Island area. Correlations between CPT data and V_S, V_P and ρ are established and checked against the available data. Although there is some transformation uncertainty and a dependency on the methods used for measuring V_S directly (S-PCPT vs PS-logging), the proposed models provide results which are within a defined range of uncertainty ($\pm30\%$ for V_S, $\pm10\%$ for V_P and $\pm15\%$ for unit weight).
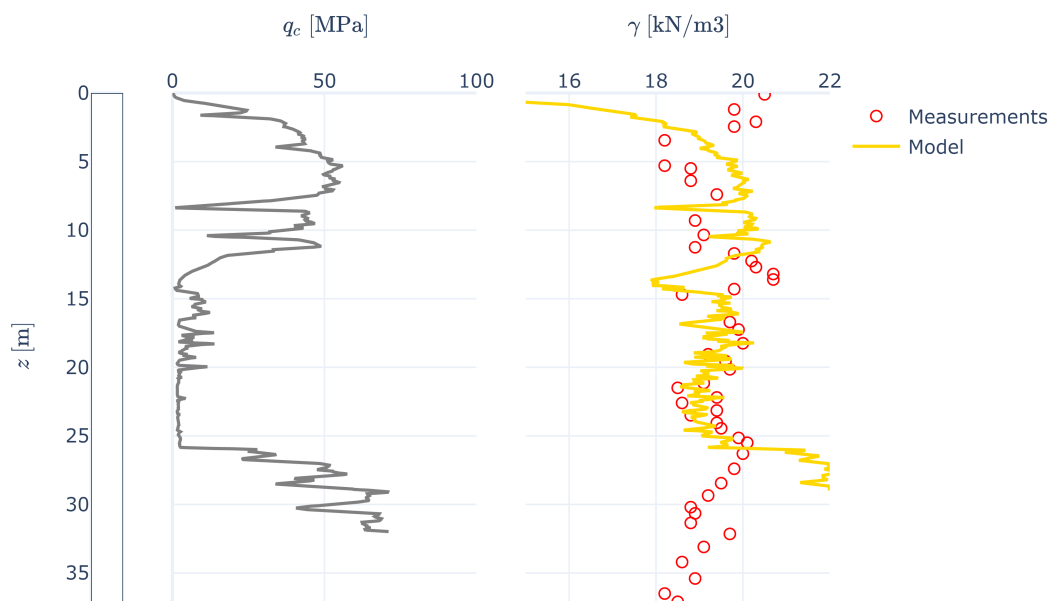
Figure 4.16: *Derived and measured unit weight at location BH-015.*

Chapter 5

Seismic data overview and pre-conditioning

This chapter describes the quality control and pre-conditioning of the seismic data prior to the seismic inversion. The preconditioning sequence for the Airgun data was different than for the Sparker dataset, due to the differences is data quality. Both Airgun and Sparker data were acquired in suboptimal weather conditions, having data of fluctuating amplitudes across the section as a result. This is to some degree compensated for, as described below.

5.1 Airgun data

Airgun data only required preconditioning in the anglestack domain. After generating 5-degree angle-stacks from the received gathers, the pre-conditioning consists of an applied lowpass filter with a cut of 200 Hz, and an alignment of stacks. Afterwards, the seismic amplitudes were balanced, to drastically reduce the effect of suboptimal weather conditions on the measured seismic data.

5.1.1 Seismic angle-stack generation

The pre-stack depth migrated offset gathers were stacked into ten five-degree angle stacks:

- $0°$-$5°$
- $5°$-$10°$
- $10°$-$15°$
- $15°$-$20°$
- $20°$-$25°$
- $25°$-$30°$
- $30°$-$35°$
- $35°$-$40°$
- $40°$-$45°$
- $45°$-$50°$

SolidGround
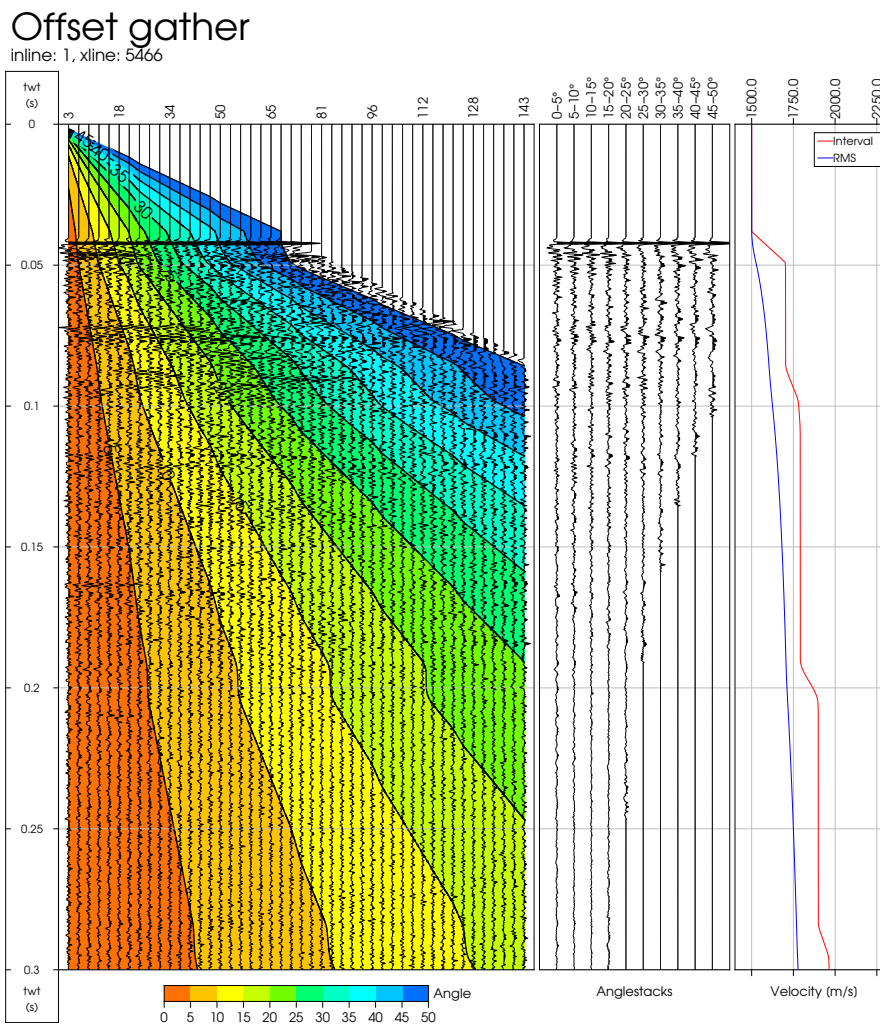
Figure 5.1: *Seismic offset gathers and resulting angle-stacks at Ida-1. The left panel shows the offset gathers for location in-line = 1, cross-line = 5466 of line ML01, overlaid with the parts of the seismic data that go into each 5-degree angleband, using the seismic velocities. The resulting anglestacks are displayed on the middle panel. On the right panel, the seismic interval and RMS velocity are displayed at this location.*

5.1.2 Lowpass filtering

The first step in the preconditioning sequence was the application of a lowpass filter with a cutoff at 200 Hz, to eliminate the high frequencies with relatively high amplitudes. Figure 5.2 shows the amplitude spectra of line ML01 before and after lowpass filtering for all anglestacks.
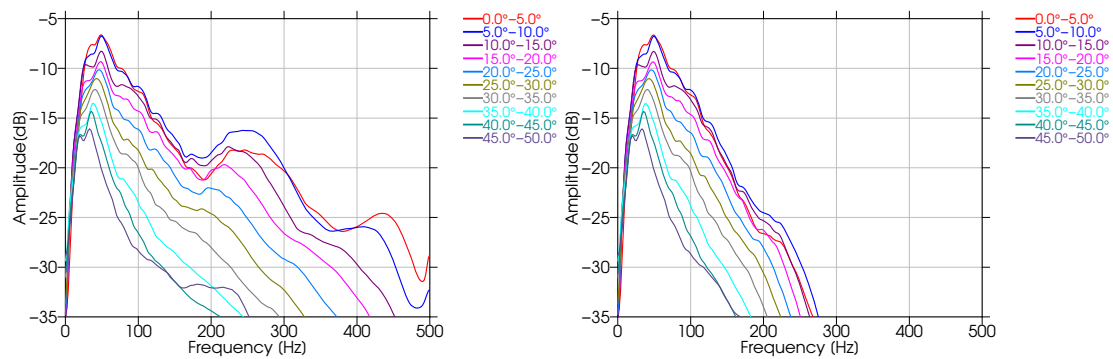
Figure 5.2: *Amplitude spectra of the raw (left) and lowpass filtered (right) seismic data of line ML01. As seen on the left, an abundant amount of energy is present in the frequency ranges above 200 hz. The absolute energy levels are still more than 5 dB lower than the peak energy below 100 Hz. It was therefore deemed appropriate to apply a lowpass filter with a cutoff of 200 Hz.*

5.1.3 Seismic alignment

The computed angle-stacks showed minor levels of residual move-out, hence the angle-stacks were aligned using SolidGround's algorithm with the $5°$-$10°$ angle-stack as the reference stack.

The displacement fields were computed in an iterative fashion in order to ensure maximum similarity between the angle-stacks going into the warping and in order to be as robust as possible against potential polarity reversals. That is, from low angles to central angles and from high angles to central angles.

$$0° - 5° \longrightarrow 5° - 10° \longrightarrow 10° - 15° \longleftarrow 15° - 20° \longleftarrow \ldots \longleftarrow 40° - 45°$$

The selected parameters for the alignment are a compromise between providing a high cross-correlation and a time shift field sufficiently smooth in order not to alter any waveform. Here they were selected to be relatively conservative as the computed angle-stacks initially show a relatively high level of cross-correlation.

The warping algorithm is amplitude preserving and the resulting displacement fields are optimized both locally and globally.

The regularization of the warping is controlled by three parameters:

- Horizontal smoothing of displacement fields – A lateral effective smoothing over seismic traces

- Vertical smoothing of displacement fields – A value relative to the center of frequency of the seismic

- Number of iterations – A number of iterations was selected after which, no significant improvements in the cross-correlation were observed

Quality control of the warping of the angle-stacks is displayed in Presentation Seismic alignment of airgun data QC shows the following:

- Angle-stack gathers at the total depth of Ida-1

- Section plots of the seismic anglestacks before and after warping

- Section plots of the applied displacement fields

5.1.4   Seismic amplitude balancing

Due to suboptimal weather conditions when acquiring the seismic data, some amplitude differences that can not be attributed to geological phenomena were observed. An example can be seen in upper plot in Figure 5.3.

In an attempt to resolve this issue, amplitude balancing has been performed. This partially boosts/restores amplitudes to a level that is believed to better represent the encapsulated geology. Per line and per stack, a correction field is calculated and multiplied to its respective seismic stack line. The procedure is coming to this correction field can be broken down in the following steps:

- Clip the seismic to eliminate extreme values

- Calculate a reference smooth RMS field. This field is clipped with stack-dependent values

- Calculate a detailed smoothened RMS field. This field is also clipped with stack-dependent values

- Calculate the correction field which is based on the ratio of the reference and detailed RMS field

- Apply the correction field to the seismic cube through multiplication

The dataset was amplitude balanced by estimating a sliding RMS field over a clipped seismic cube.

The clipping is necessary to leave out extremeties and high amplitudes stemming from strong reflectors. The two fields allow for the computation of a stack-dependent correction field, which is then applied to the whole cube cube.

A full QC of this procedure can be found in Presentation Seismic amplitude balancing of airgun data QC, showing the following for each line and each anglestack:

- Section plots of the input seismic data

- Section plots of the clipped seismic data

- Section plots of the reference/target RMS field

- Section plots of the detailed RMS field

- Section plots of the correction field

- Section plots of the amplitude balanced seismic data
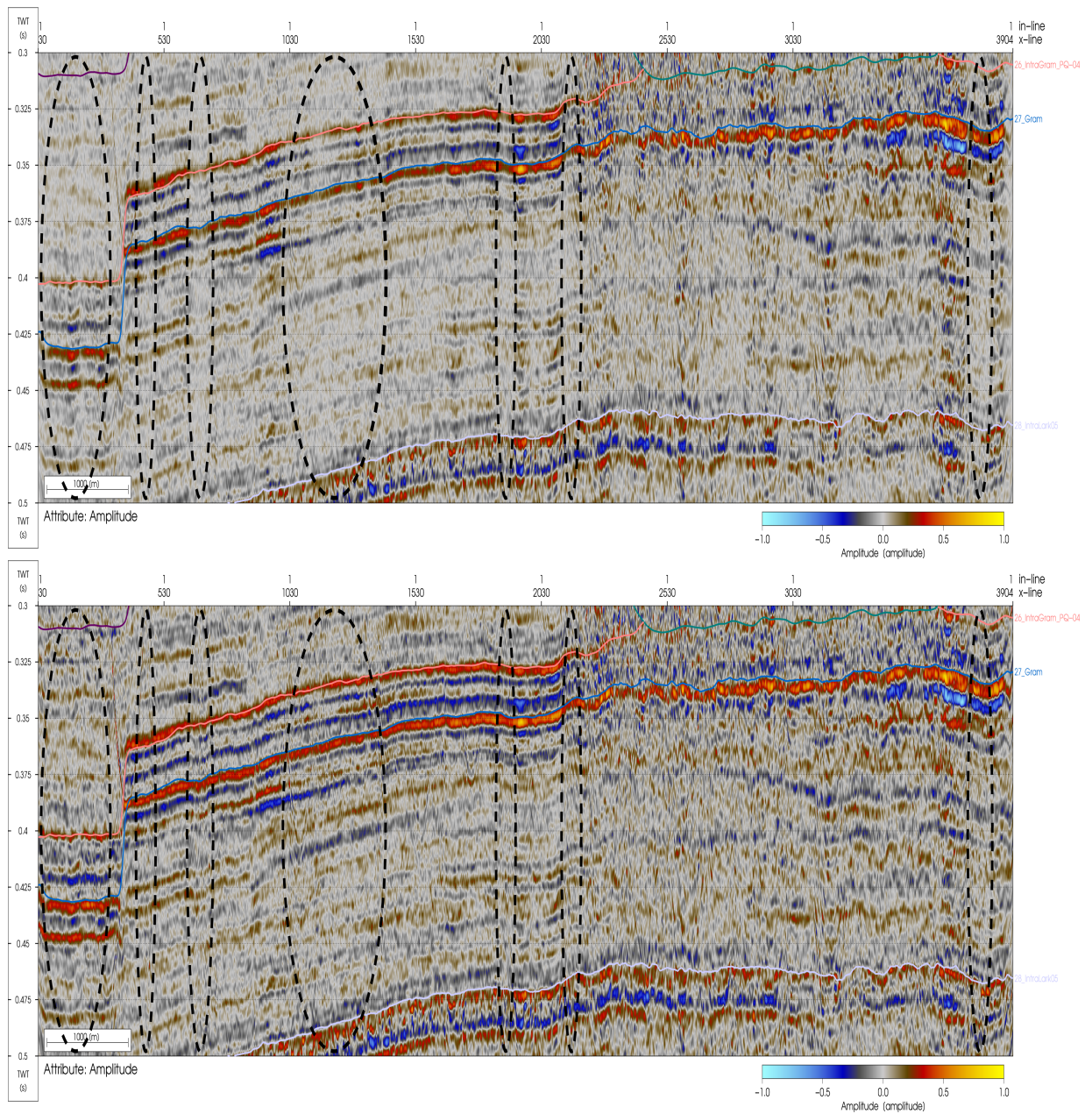
Figure 5.3: *The artifacts to compensate are the dimmer zones (vertical white stripes, highlighted with the dashed black outlines) in the upper figure displaying the 0°-5° anglestack of line ML04. After amplitude balancing the seismic stacks, these zones boosted so amplitudes now match the surrounding seismic that is not affected (bottom figure). An apparent overall boost is noticeable, zones where the difference is most clear are circled with a black dashed line.*

5.2 Sparker data

The different nature of the Sparker data required a more extensive preconditioning workflow. In the offset gather domain, an F-k filter was applied to remove linear up- and downdipping noise. After generating 5-degree angle-stacks from the received gathers, the preconditioning consists of an applied bandpass filter with a cut of 200 Hz on the low end and a cut on the high end of 1000 Hz. A Cadzow filter was applied to these stacks to further eliminate random noise. Further, a seismic alignment and amplitude balancing were applied.

5.2.1 F-k filtering

The seismic gathers showed linearly updipping and downdipping noise. Different F-k settings were tested and a suitable setting was found. The F-k filtering was also tested in the elastic inversion domain to make sure the seemingly harmless removal of noise was not affecting, but rather improving the quality of the inversion results.

The filtering was done in the F-k domain where the degree of filtering is determined by the wave number. The area left after muting is then backtransformed to offset domain. An example is shown in Figure 5.4 where the process is shown at the well location of CPT 005.
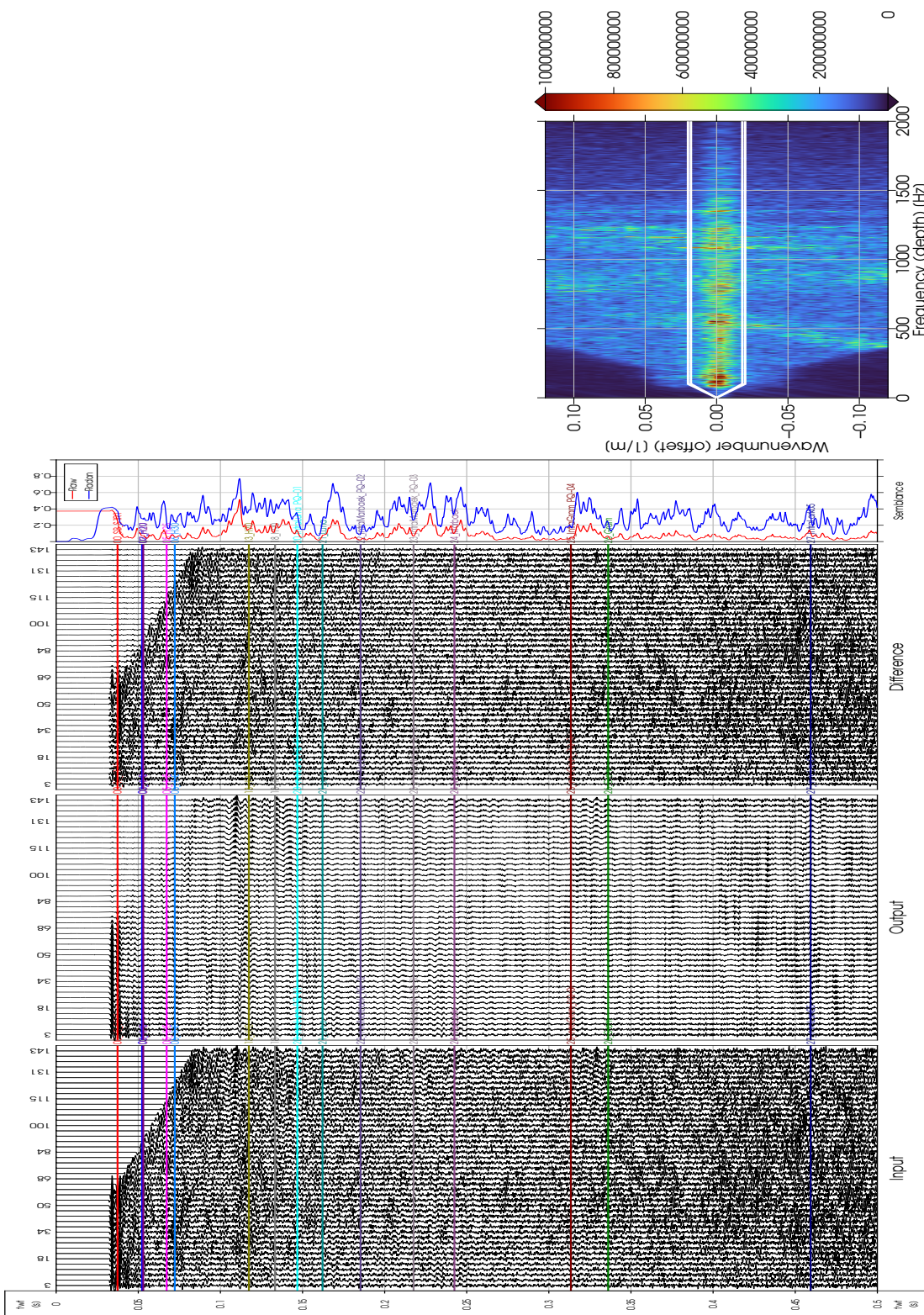
Figure 5.4: *The left figure shows (from left to right) raw input gather, F-k filtered gather and residuals at the location of line ML01a, closest CPT 005. The semblance curve after applying the F-k filter (blue curve) shows an increase in semblance, indicating the offsets are more similar. The figure on the right displays the seismic gather in the F-k domain, where the white lines outline the zone which is muted. That is everything outside that area.*

5.2.2   Seismic angle-stack generation

The F-k filtered gathers were stacked into ten five-degree angle stacks:

- 0°-5°
- 5°-10°
- 10°-15°
- 15°-20°
- 20°-25°

- 25°-30°
- 30°-35°
- 35°-40°
- 40°-45°
- 45°-50°

5.2.3   Bandpass filtering and Cadzow filtering

The first step in the preconditioning sequence after anglestack generation was the application of a bandpass filter with a cutoff at 200 Hz on the low end, and a cutoff at 1000 Hz on the high end.

One these low and high frequencies were filtered out, some random noise was still present. This was removed with the use of a Cadzow filter with rank 1.

5.2.4   Seismic alignment

The anglestacks showed minor levels of residual move-out, hence the angle-stacks were aligned using SolidGround's algorithm with the 5°-10° angle-stack as the reference stack.

This procedure is identical to the one applied to the airgun data, see subsection 5.1.3.

5.2.5   Seismic amplitude balancing

The last step in the preconditioning sequence on the Sparker data was amplitude balancing.

This procedure is identical to the one applied to the airgun data, see subsection 5.1.4.

Chapter 6

Deformation and elastic properties from inversion

This chapter describes the results of the final seismic AVO inversion and the derived properties.

The pre-conditioned seismic angle-stack data were inverted for bulk modulus, shear modulus and density. In a relative inversion, the calculated products are centered around a fixed value - a constant background model. An absolute inversion makes use of a non-constant background model, also called a prior model, or a low frequency model.

The inversion uses the Aki-Richards approximation [Aki and Richards, 1980] to the exact and non-linear Zoeppritz equations [Zoeppritz, 1919], originally formulated in acoustic impedance, V_P/V_S and density and given below.

$$
\begin{aligned}
R(\theta) = (\frac{1}{1 - \sin^2 \theta} &- 8 \sin^2 \theta \, e^\lambda) \, \alpha \\
&+ 8 \sin^2 \theta \, e^\lambda \, \beta \\
&+ (1 - \frac{1}{1 - \sin^2 \theta} + 4 \sin^2 \theta \, e^\lambda) \, \gamma,
\end{aligned}
\tag{6.1}
$$

where

$$\alpha = \frac{1}{2}(\ln(AI_2) - \ln(AI_1))$$

$$\beta = \frac{1}{2}(\ln\left(\frac{V_{P2}}{V_{S2}}\right) - \ln\left(\frac{V_{P1}}{V_{S1}}\right))$$

$$\gamma = \frac{1}{2}(\ln(\rho_2) - \ln(\rho_1))$$

$$\lambda = -\ln\left(\frac{V_{P1}}{V_{S1}}\right) - \ln\left(\frac{V_{P2}}{V_{S2}}\right)$$

and AI_1, $\frac{V_{P1}}{V_{S1}}$, ρ_1 and AI_2, $\frac{V_{P2}}{V_{S2}}$, ρ_2 are the acoustic impedance, V_P/V_S and density respectively in a layer above and below an interface, θ is the angle of incidence of the seismic wave, and $R(\theta)$ is the computed angle of incidence dependent reflectivity.

This set of equations describes the reflection coefficients of a sound wave encountering the elastic properties of the assumed horizontally layered earth. The inversion process calculates, based on seismic data, the elastic properties of the Earth.

For this project, the equations were formulated in bulk modulus, shear modulus and density instead. This is merely a transformation of variables without any loss of information.

The relative inversion results had constant background values of $15.65e9$ Pa for bulk modulus, $2.0e9$ Pa for shear modulus and 2300 kg/m^3 for density.

From these calculated properties, the following can be calculated:

$$\nu = \frac{3k - 2g}{2\,(3k + g)},$$

$$AI = \sqrt{\rho\left(k + \frac{4}{3}g\right)},$$

$$\frac{V_P}{V_S} = \sqrt{\frac{k + \frac{4}{3}g}{g}},$$

$$V_P = \frac{AI}{\rho},$$

$$E = 3k\,(1 - 2\,\nu),$$

where ν is Poisson's ratio, AI the acoustic impedance, $\frac{V_P}{V_S}$ the ratio between acoustic and shear wave velocity, V_P the acoustic wave velocity and E being the Young's modulus.

Prior to the final inversion, a range of tests was carried out to determine the optimum settings for the inversion. These entailed:

- Various pre-conditioned seismic input data versions

- The optimum weight of the input pre-conditioned seismic angle-stacks

- Wavelets estimated using the different methods

- Horizontal continuity and deviation away from the low-frequency model

- Angle-range of the input stacks

An important aspect was to define which stacks to use in the inversion as well as the levels of influence (weight) from each angle-stack that were to be used. Using stacks $0°$-$45°$, no stack was of significant better/worse quality, hence all stacks were weighted equally.

6.1   3D Low frequency modelling

To compare the elastic information from the seismic data obtained through inversion to ground truth data from CPTs, seismic CPTs, Boreholes and deep log data, additional information is necessary as seismic data contains information of relative changes of elastic properties, not absolute values. To infuse a notion of absolute values, the generation of a low frequency model, also called a prior model or background model, is required.

The input data for building these models (one for each elastic property), consists of:

- Data from carefully chosen CPT, SCPT and BH locations, primarily for the shallow parts

- Data from Ida-1 for the deeper parts

- Seismic surfaces

For each parameter, an interpolation is done between the available geotechnical locations in a 3D grid, where for each 2D line in the seismic survey, this property is cut out to obtain a 2D low frequent elastic model.

Data from IDA-1 in the depth of interest consists only of p-wave velocity and gamma ray. To model the various deformation and elastic parameters s-wave velocity and density are needed. Based on the Greenberg-Castagna relation [Greenberg and Castagna, 1992] an robust estimate of s-wave velocity were obtained, and based on the Gardner relation [Gardner and Gregory, 1974] an robust estimate of density was obtained. The Greenberg-Catagna and the Gardner relations are guided by the volume of clay at a given site, this volumes of clay is estimated from the Gamma ray. The relation between gamma ray and volume of clay are based on a plot provided by GEUS, see Figure 3.1, and on well site reports for IDA-1.

These relations are the basis of the absolute values of the final deformation and elastic parameters, thus inversion results should be used with these modelling uncertainties in mind.
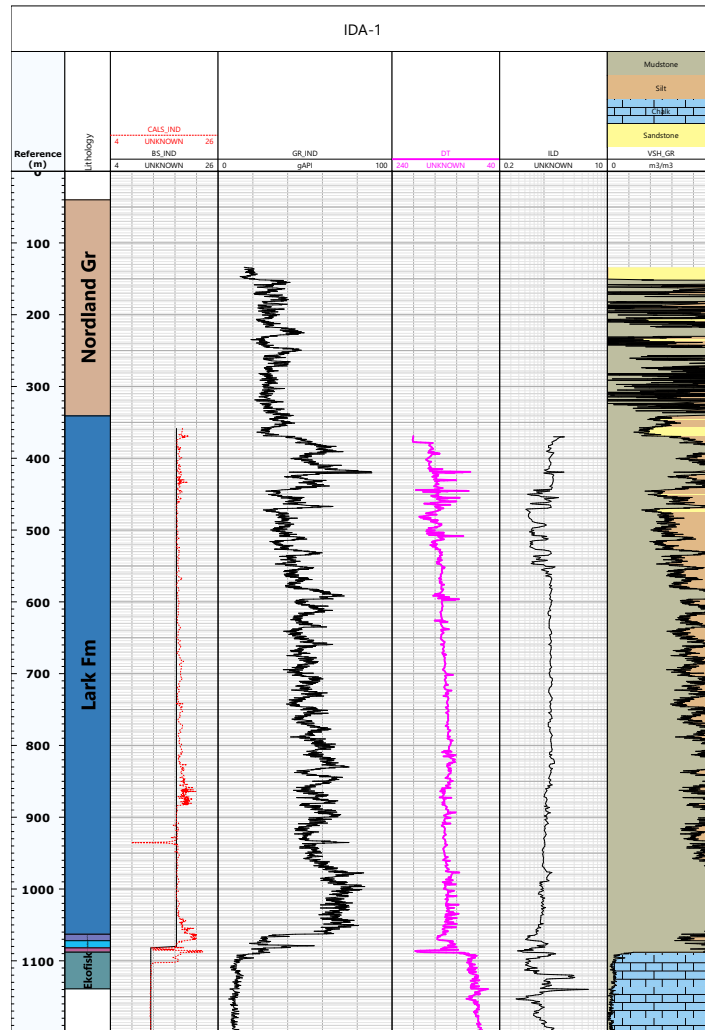
Figure 6.1: *Log information from IDA-1 with an estimate of volume of clay calculated from the gamma ray. Provided by GEUS.*

6.2 Airgun data

Using optimum settings, a final relative and absolute inversion result was obtained. For the absolute inversion, low-frequency models using Ida-1 and CPT information for the shallow section were used. Results around Ida-1 can be seen in Figure 6.2 and Figure 6.3 on the next pages.

A full QC can be seen in Appendix C.
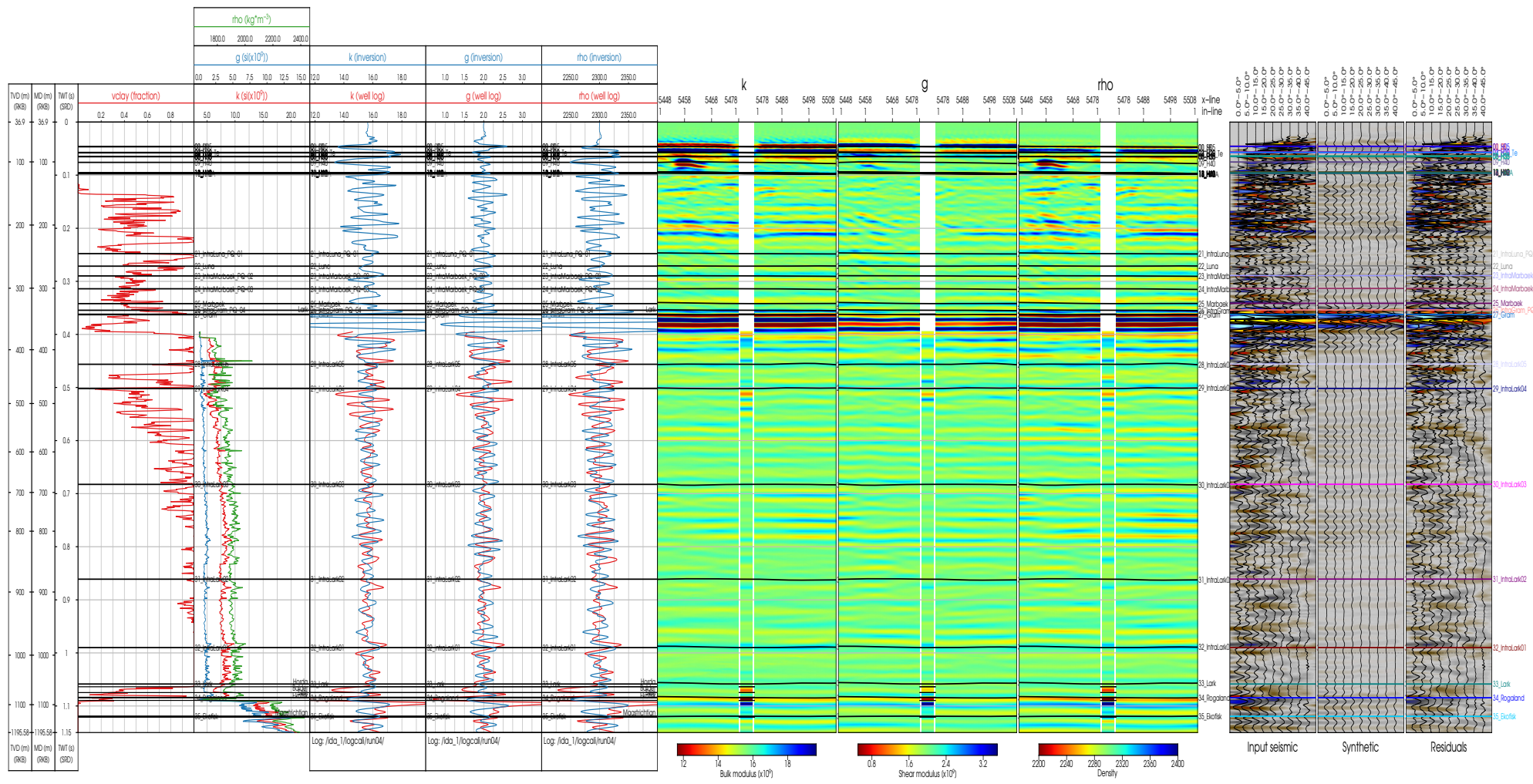
Figure 6.2: *Relative AVO inversion result along well Ida-1. The panel on the far left displays the volume of clay log. The second panel shows the elastic logs (k, g and ρ) in the seismic sample rate (1 ms). The next three panels are curves for each elastic parameter, comparing the de-trended and lowpass filtered log data and the inversion result along the well trace. The minisections show the inversion data 30 traces of line ML01 on each side from Ida-1, with the well data displayed in the center. The seismic panels on the far right display, in the following order, the input seismic, the synthetic (forward modelled from the inversion result), and the residuals (difference between input and synthetic). Note that however a lot of energy is thrown in the residuals, the inverted properties capture the dynamics of the log data to a high degree.*

Figure 6.3: *Absolute AVO inversion result along well Ida-1. The panel on the far left displays the volume of clay log. The second panel shows the elastic logs (k, g and ρ) in the seismic sample rate (1 ms). The next three panels are curves for each elastic parameter, comparing the lowpass filtered* log data *and the* inversion result *along the well trace. The low frequent background/prior model is displayed as a black dashed line. The minisections show the inversion data 30 traces of line ML01 on each side from Ida-1, with the well data displayed in the center. The seismic panels on the far right display, in the following order, the input seismic, the synthetic (forward modelled from the inversion result), and the residuals (difference between input and synthetic). Again, note that despite the high energy in the residuals, the match between log data and inversion result is deemed very good.*

6.3   Sparker data

The Sparker data proved to be a bit more challenging, especially in the very upper part where the seismic data has considerably higher amplitudes.

Using optimum settings, a final relative and absolute inversion result was obtained. For the absolute inversion, low-frequency models using Ida-1 and CPT information for the shallow section were used. Results around Ida-1 can be seen in Figure 6.2 and Figure 6.3 on the next page.

A full QC can be seen in Appendix D
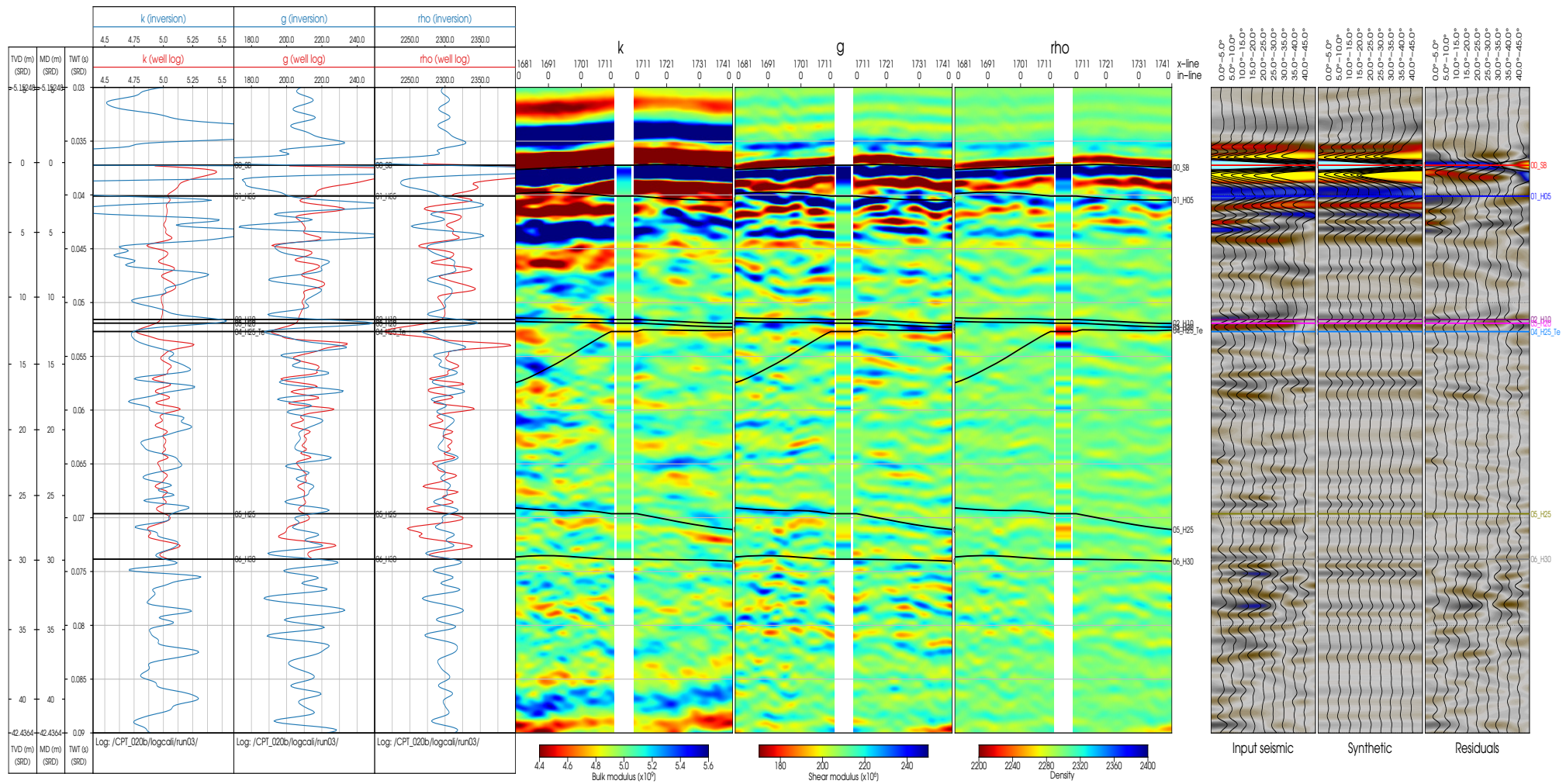
Figure 6.4: *Relative AVO inversion result along well CPT 020b. The first panel shows the elastic logs (k, g and ρ) in the seismic sample ra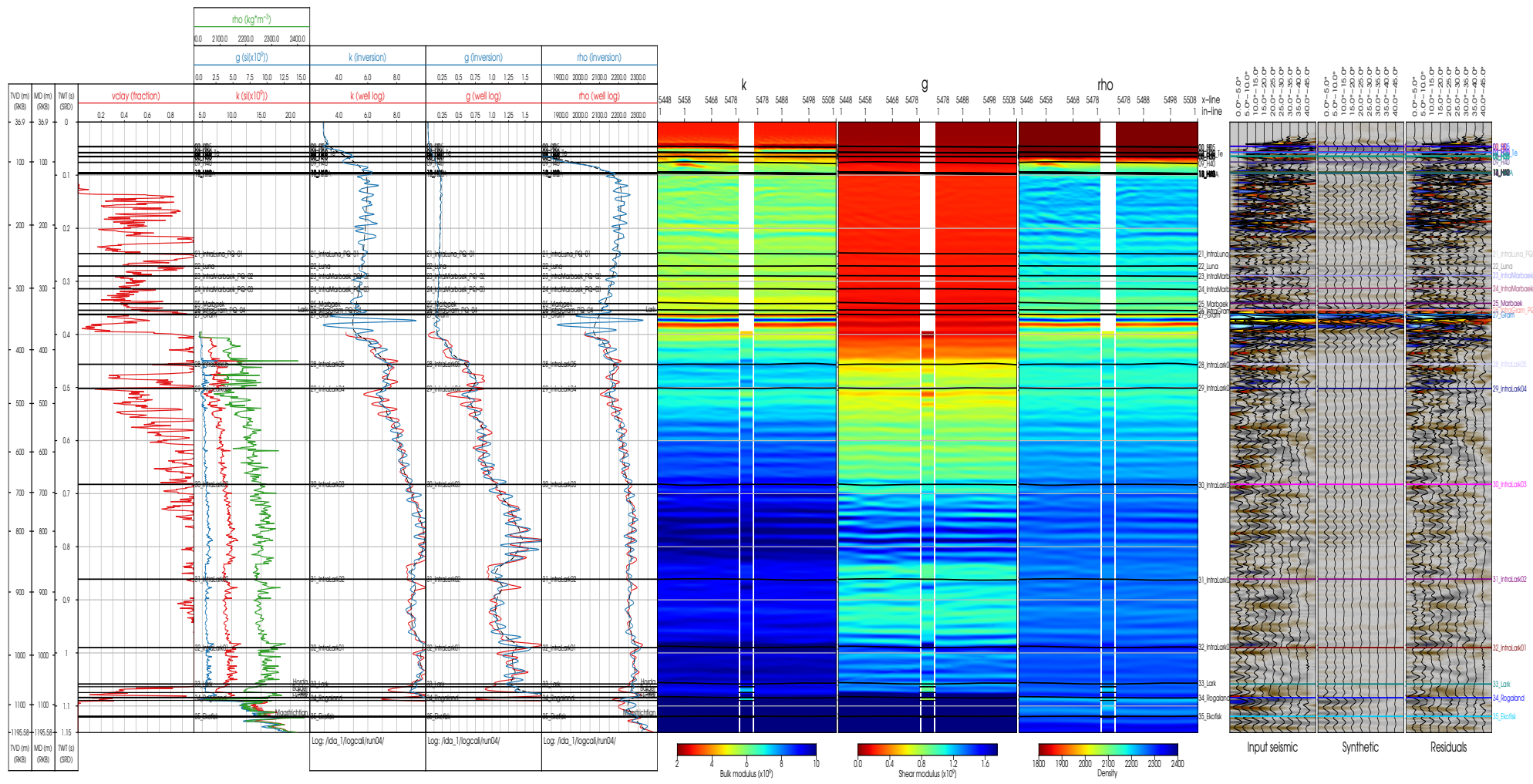te (0.1 ms). The next three panels are curves for each elastic parameter, comparing the de-trended and lowpass filtered log data and the inversion result along the well trace. The minisections show the inversion data 30 traces of line ML04 on each side from CPT 020b, with the well data displayed in the center. The seismic panels on the far right display, in the following order, the input seismic, the synthetic (forward modelled from the inversion result), and the residuals (difference between input and synthetic). In comparison to the Airgun data, the residuals have a significantly lower amount of energy.*
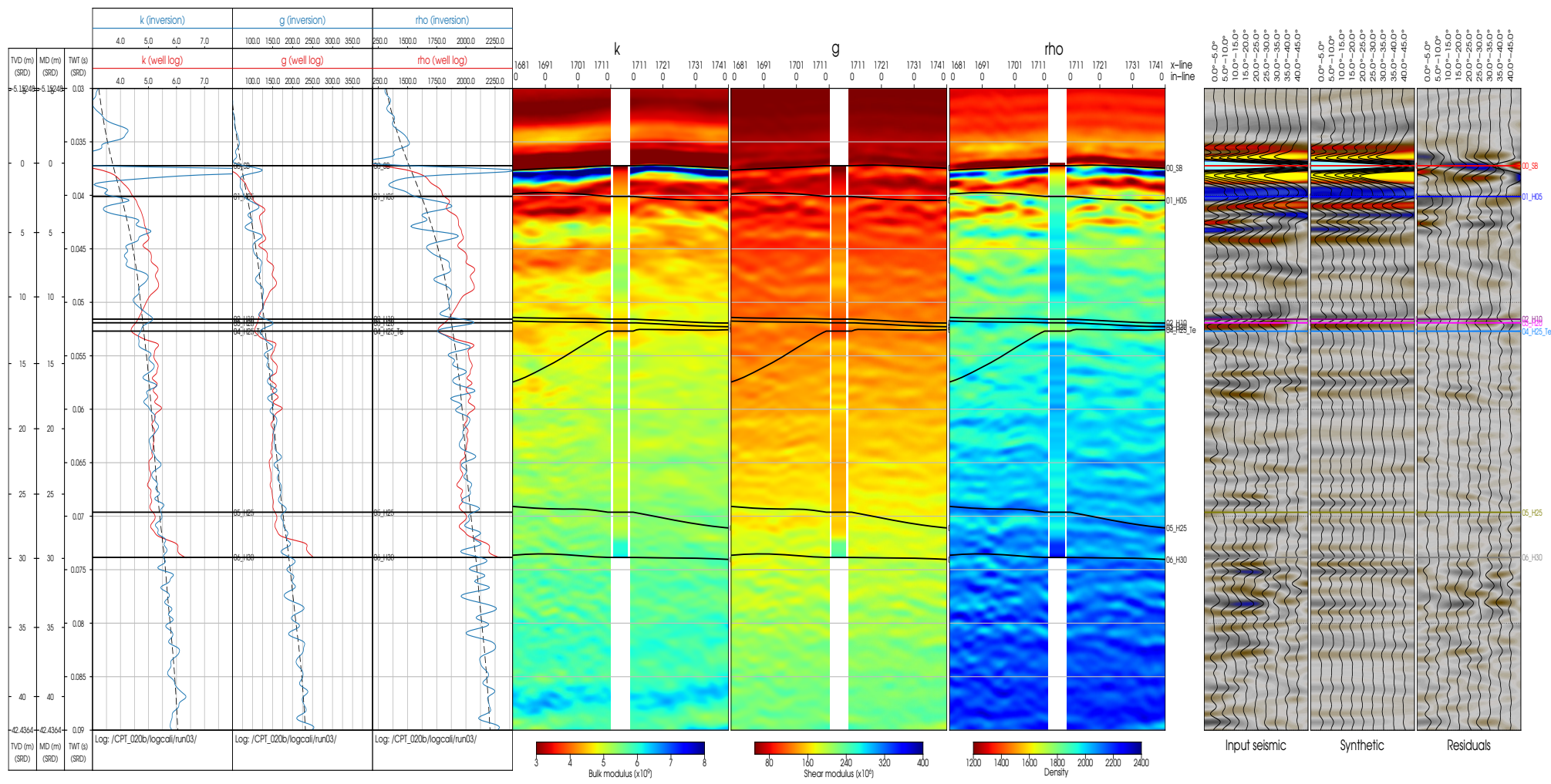
Figure 6.5: *Absolute AVO inversion result along well CPT 020b. The first panel shows the elastic logs (k, g and ρ) in the seismic sample rate (0.1 ms). The next three panels are curves for each elastic parameter, comparing the lowpass filtered log data and the inversion result along the well trace. The low frequent background/prior model is displayed as a black dashed line. The minisections show the inversion data 30 traces of line ML04 on each side from CPT 020b, with the well data displayed in the center. The seismic panels on the far right display, in the following order, the input seismic, the synthetic (forward modelled from the inversion result), and the residuals (difference between input and synthetic). Again, note that despite the high energy in the residuals, the match between log data and inversion result is deemed very good.*

6.4 Considerations

Relative inversions are a direct link to the seismic data. Just as seismic data is centered around 0, are relative inversion results centered around a certain fixed value for all depths. Variations around that value are coming straight from the seismic data. The results for the Airgun data are deemed of good quality. The Sparker results are deemed of sufficient quality, where extra caution is necessary for the very shallow part (first ~10 meters).

In the absolute case however, the relative variations are centered around a value that varies both laterally and vertically we call prior/low frequency model. The use of such a model in the inversion inherits the uncertainty that comes with that model. In the case of low data support (only 1 deep well, Ida-1, inside the seismic survey) this uncertainty can become significant.

Chapter 7

CPT prediction

7.1 Method - Sparker domain

The CPT prediction is formulated in a probabilistic framework and is able to handle any type of CPT property. This method is able to address the fact that a number of different CPTs exhibit an identical elastic response, by assigning equal probabilities to such CPT's. The properties used to perform the CPT prediction are the absolute acoustic impedance and V_P/V_S inversion results.

This process was performed for following CPT properties:

- Cone resistance

The CPT prediction is based on non-Gaussian probability density functions (PDFs) using Gaussian kernel-density estimation. The probability density functions are calculated based on polygons that encapsulate points from the inversion results. The PDFs are then applied to the inversion data to arrive at CPT probabilities. From the interpreted logs and the log reports provided by Energinet, it is seen that the subsurface that is inverted, primarily is a sand-clay system. The CPT probabilities are transformed to actual CPT values by applying a calculated correlation from the geotechnical data.

The following is evaluated iteratively to estimate the CPT volumes:

- Cross-plots of acoustic impedance versus V_P/V_S, for inversion results.

- Cross-plots of acoustic impedance versus V_P/V_S, for well log data.

- PDFs are calculated based on polygons encapsulating points from the inversion results.

- CPT probabilities based on the estimated PDFs and the inversion results are quality controlled against log observations and in sections.
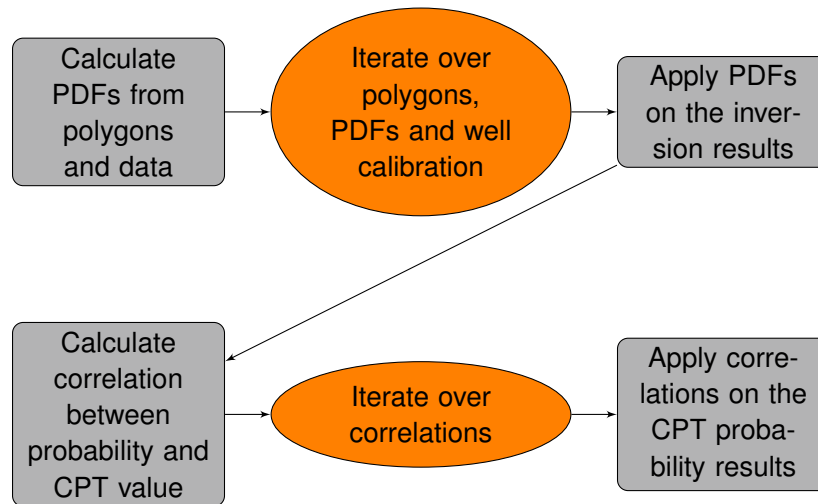
Figure 7.1: *Flow chart of the CPT prediction method.*

- Optionally refine the PDFs by modifying the established polygons.

- Cross-plots beteween CPT probability from inversion and CPT value from log.

- Calculate and apply correlation beteween CPT probability from inversion and CPT value from log

- Optionally refine above calculated correlation, see Figure 7.1.

7.2   Method - Airgun domain

For the deeper part of the target area covered by the airgun data, CPT data were not available. Therefore the cone resistance for the deep part could not be correlated to actual measured data. In this case a model was built and applied. The model utilizes the results derived in the soil classification, see Chapter 8. As we are in a dominantly sand-clay system, the likelyhood for sand and clay was set to be the driver of the cone resistance model. A model for sand (Equation 7.2) and a model for clay (Equation 7.3) was build. The two models were then mixed, based on the sand clay probabilities derived (see Equation 7.4).

For the sand part, the model is based on [Baldi, 1986].

$$\sigma'_m = \frac{1}{3} \left(\sigma'_{\nu_0} + 2 \cdot k_0 \cdot \sigma'_{\nu_0} \right), \tag{7.1}$$

$$q_{c_{\text{sand}}}(z) = 0.001 \cdot e^{\left(\frac{Dr}{\left(\frac{1}{C_2} \right)} \right)} \cdot C_0 \cdot \left(\sigma'_m \right)^{C_1}, \tag{7.2}$$

where $Dr = 0.9$ is the relative density to account for low pore volume at these depths, $C_0 = 181.0$, $C_1 = 0.55$ and $C_0 = 2.61$.

For the clay part, an extrapolation of the trend for normally consolidated clays was applied, given by:

$$q_{c_{\mathrm{clay}}}(z) = 0.001 \cdot 0.22 \cdot 10 \cdot 20 \cdot z \tag{7.3}$$

Letting the probability of clay p_{clay} act as a weighting factor, the cone resistance is given by:

$$q_c = p_{\mathrm{clay}} \cdot q_{c_{\mathrm{clay}}} + (1 - p_{\mathrm{clay}}) \cdot q_{c_{\mathrm{sand}}} \tag{7.4}$$

7.3 Observations

An example of the quality control for the CPT prediction is seen on Figures 7.2, 7.3 and 7.4.

The CPT prediction results offer a comprehensive understanding of CPT properties within the seismic bandwidth and enable the identification of spatial variations in specific CPT properties. By transforming the inversion results into the CPT domain, a direct evaluation of the seismic inversion results against the CPT measurements becomes feasible. This integration links two independent measures, namely seismic data and CPT measurements.

Many of the challenges discussed in previous chapters are also addressed in the CPT prediction analysis. Since the evaluation primarily occurs in the CPT domain rather than the elastic domain, the estimation of elastic properties from CPTs has a reduced influence on the uncertainties associated with seismic CPT prediction.

Overall, a high level of agreement between the seismic-predicted CPT properties and the actual CPT measurements was observed at most CPT locations. Additionally, the behavior of CPT predictions along the seismic lines demonstrated good consistency.

SolidGround
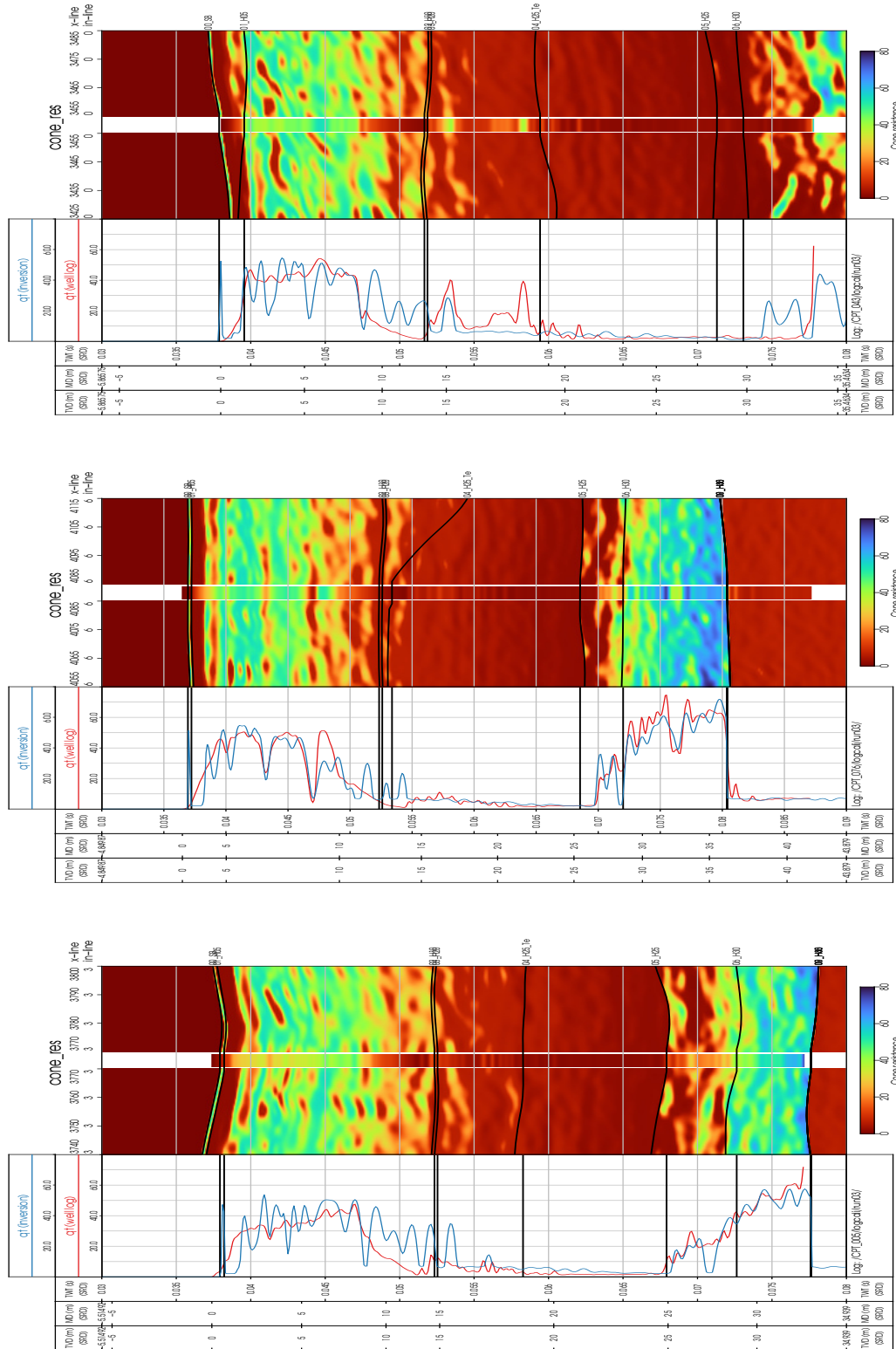
Figure 7.2: *Synthetic cone resistance for locations CPT 005 (left), CPT 076 (middle) and CPT 043 (right). The seismic data for all three locations are taken from line ML01a.*
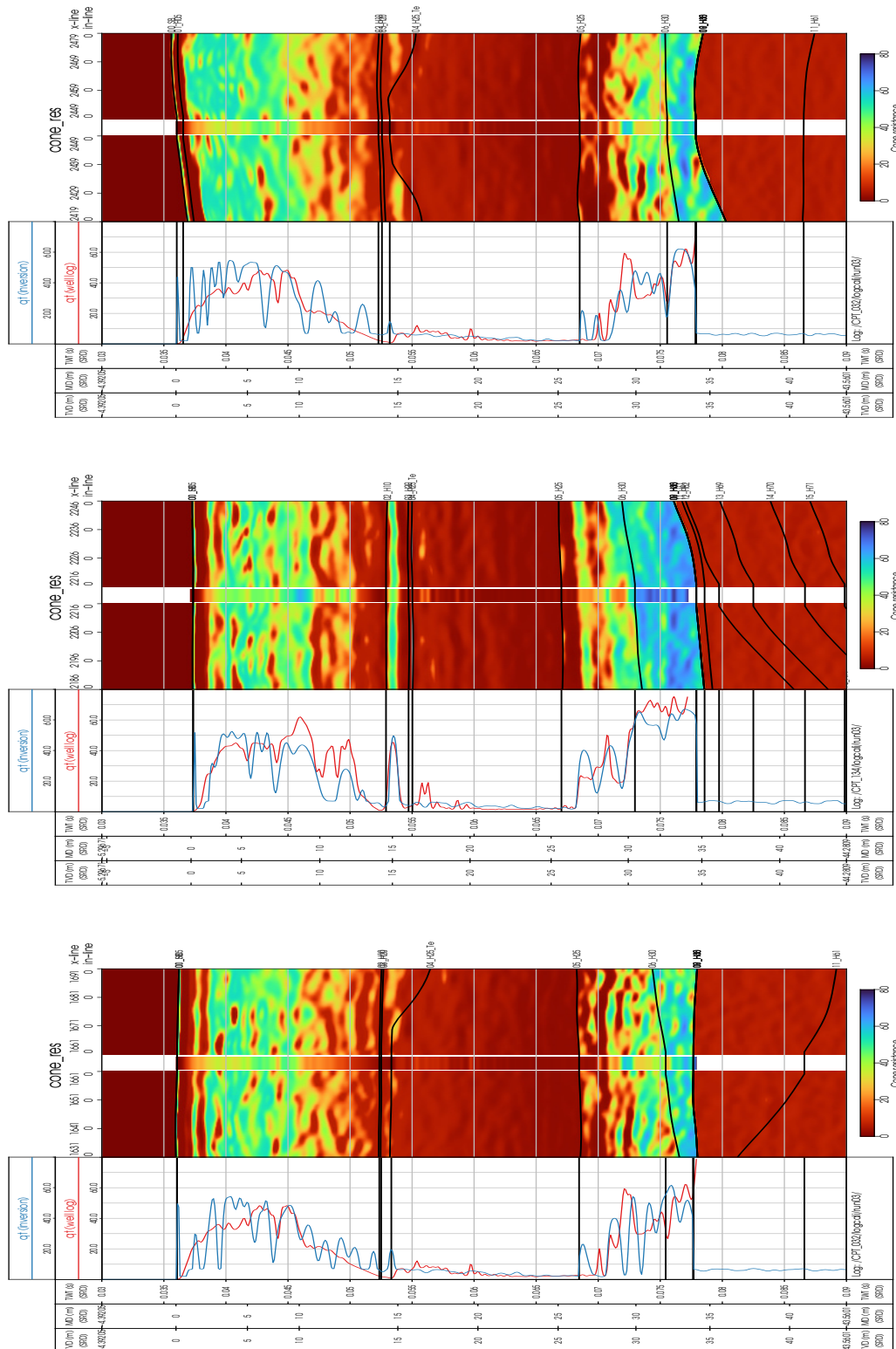
Figure 7.3: *Synthetic cone resistance for locations CPT 032 (left), CPT 134 (middle) and CPT 032 (right). The seismic data for CPT 032 (left) and CPT 134 (middle) are taken from ML03. The seismic data for CPT 032 (right) are taken from ML04.*
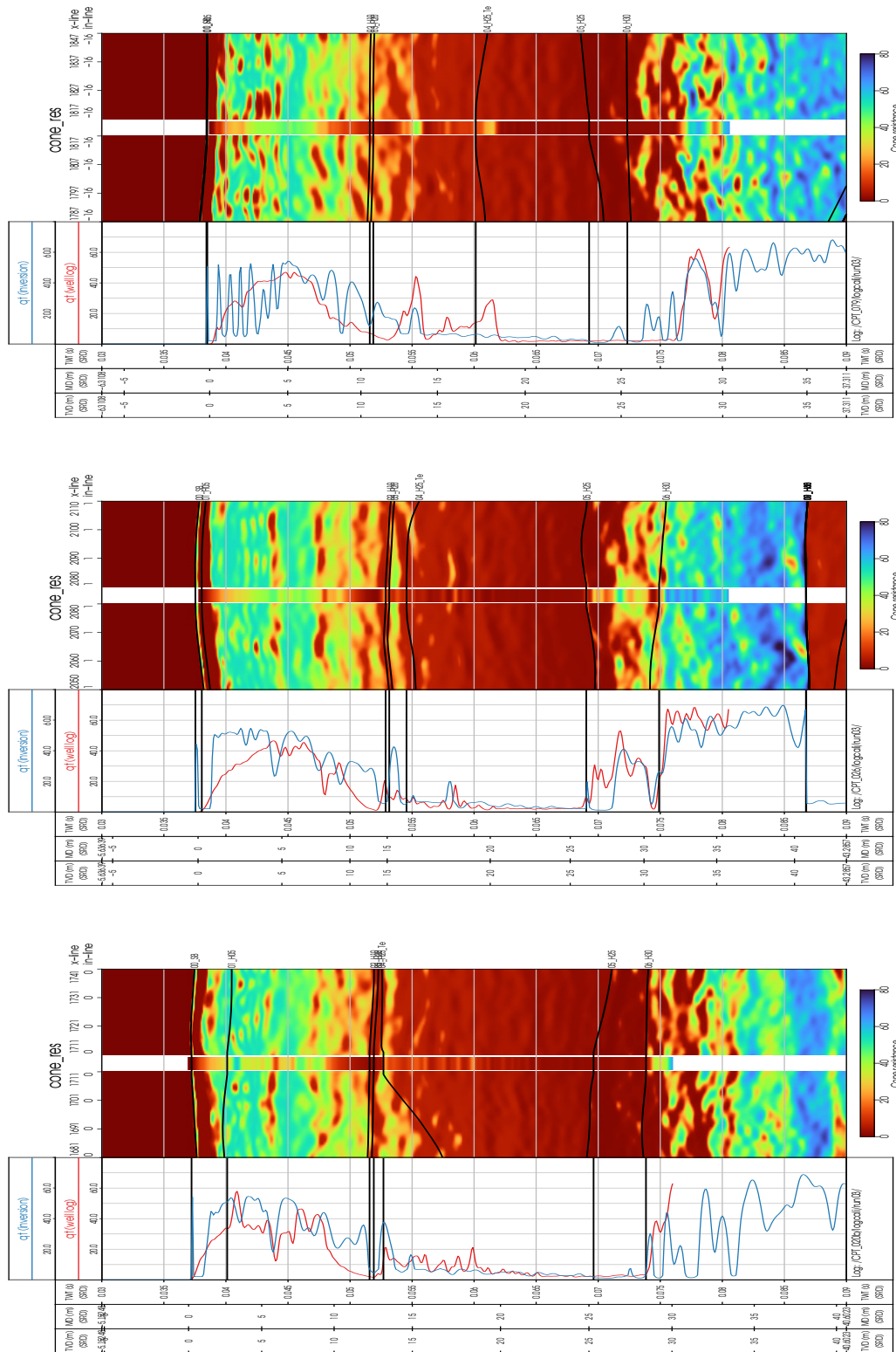
Figure 7.4: *Synthetic cone resistance for locations CPT 020b (left), CPT 026 (middle) and CPT 079 (right). The seismic data for CPT 020b (left) and CPT 026 (middle) are taken from ML03. The seismic data for CPT 079 (right) are taken from ML04.*

Chapter 8

Soil classification

This chapter describes the results of the soil classification.

The absolute acoustic impedance and V_P/V_S inversion results based on the pre-conditioned angle-stacks were used in a soil classification. The density inversion result was not used due to its reduced quality relative to the acoustic impedance and V_P/V_S inversion results.

The soil classification is formulated in a probabilistic framework and is able to handle any type of soil type. Probability density functions (PDFs) are estimated on training data (well log data and/or inversion results extracted along the well trajectory) and then applied using the full volume/line inversion results as input to arrive at probabilities for the defined soil types.

As such, this method is able to address the fact that a number of different soil types exhibit an identical elastic response by assigning equal probabilities to such soil types.

8.1 Probability density functions

The soil classification is based on non-Gaussian probability density functions (PDFs) using Gaussian kernel-density estimation. The probability density functions are calculated based on polygons encapsulating points of training data in an acoustic impedance versus V_P/V_S cross-plot.

Arriving at the final set of PDFs is an iterative process. The following is iteratively evaluated to estimate the soil probability volumes:

- Cross-plots of acoustic impedance versus V_P/V_S for the inversion results

- Cross-plots of acoustic impedance versus V_P/V_S for well log data

- Probability density functions are calculated based on polygons encapsulating points in the acoustic impedance versus V_P/V_S cross-plot

- Soil classification based on the estimated PDFs and the inversion results are QC'ed against well observations and in sections

- Optionally refine the PDFs by modifying the established polygons. See Figure 8.1

It is important to understand that refinements are made to generate set of PDFs that classify the inversion results optimally in terms of match with the well observations, and that the PDFs interact such that a change in a polygon for one soil classification will potentially affect other soil classes.

```
┌──────────────┐      ╭──────────────╮      ┌──────────────┐
│  Calculate   │      │  Iterate over │      │  Apply PDFs  │
│  PDFs from   │ ───▶ │   polygons,   │ ───▶ │ on the inver-│
│  polygons    │      │ PDFs and well │      │ sion results │
│  and data    │      │  calibration  │      │              │
└──────────────┘      ╰──────────────╯      └──────────────┘
```
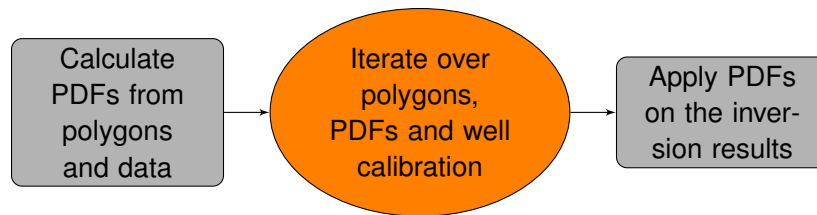
Figure 8.1: *Flow chart of the soil classification method.*

8.2   Soil classification

For practical purposes, two sets of soil classifications were run. One was ran on inversion results using the Airgun data, the second used Sparker inversion data. These two inversions are distinct from each other in terms of inversion data quality and resolution.

For each soil type, the results from Sparker and Airgun data are combined into one cube, by:

1. Re-sample the Airgun results (1 ms) to the finer Sparker sample rate (0.1 ms)

2. Merge re-sampled Airgun results with Sparker results, using horizon HKSA as boundary

3. Time-to-depth convert the obtained probability cube

Six soil types were defined for the soil classification:

- Clay
- Sand
- Gas sand

- Hard Soil
- Lignite
- Chalk

Note that if a pixel is not classified within the six classes above, it will fall into the category of undefined, so that in a given sample adding all classes together will result in the value of 1. The data used to define the PDFs were well log data and inversion results.

8.3   Considerations and evaluations

The discipline faced significant challenges due to limited data support. In the deeper section, only the Ida-1 well was available for calibrating the clay/non-clay content. For the shallow section, some boreholes contained 'Soil type' logs indicating the upper boundaries of lithological formations.

Despite the challenges, meaningful probabilities were successfully derived from both the Ida-1 well and along line ML01, where the gas layer was accurately identified. The predictions regarding sand with gas were consistent with observations of seismic amplitudes and velocities, thereby enhancing the confidence in the predictions.

Within the Quaternary layer, the soil composition is predicted to predominantly consist of sand, with areas of clays and glacial till.

In the region between the Quaternary layer and the Chalk layer, the soil is predicted to be highly homogeneous, primarily comprising clays with occasional sand stringers. Limited occurrences of lignite and harder soil zones were observed.

The Chalk layer exhibited the highest predicted probability, as it displays distinct elastic characteristics compared to other soil types. The prediction of Chalk soil aligns with the seismic interpretation.

The soil type classification presented in this report offers an atlas of the existing soils in the Energy Island area. The results are based on available but limited ground truth data and information from literature on regional soil types. The accuracy of the results is dependent on data quality and quantity. While the soil type classification aligns with available data, increased accuracy can be achieved with more ground truth information.
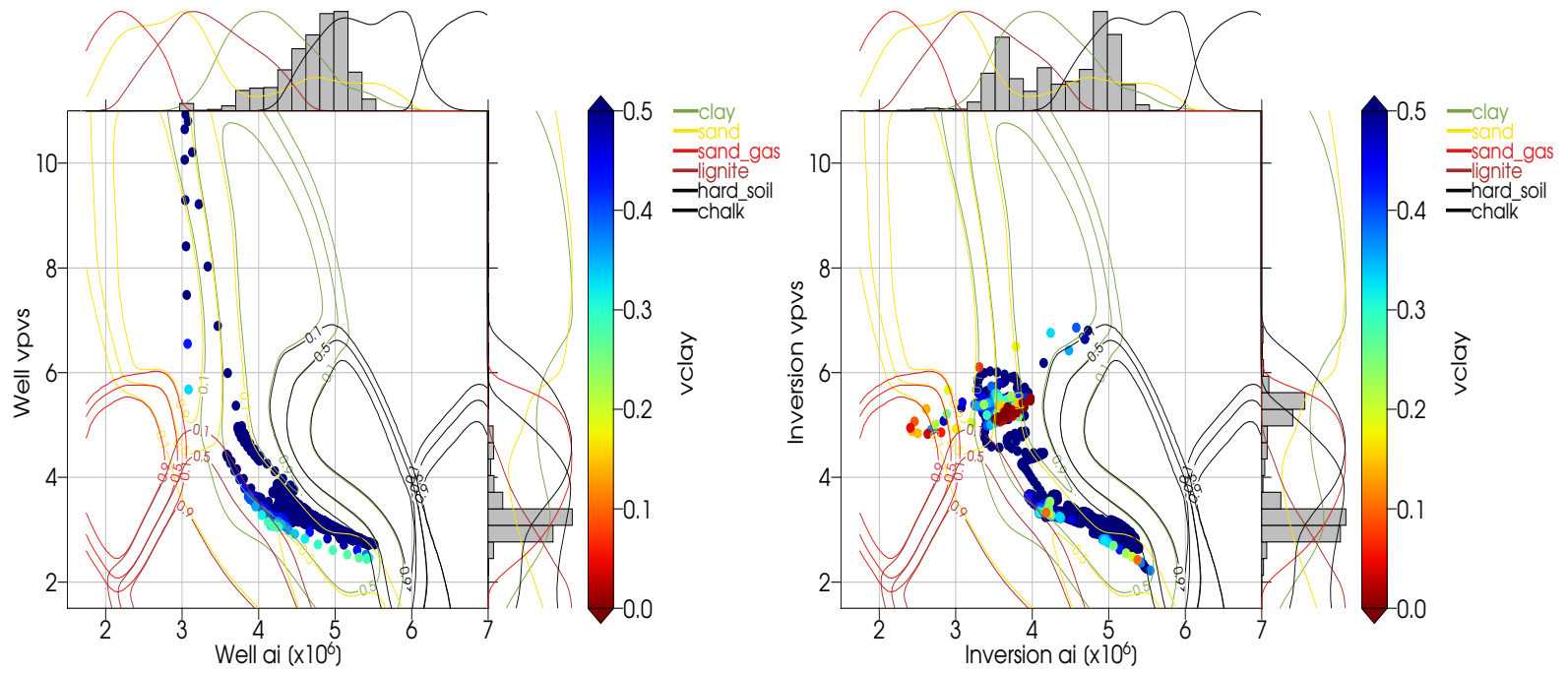
Figure 8.2: *The well data (left) and the Airgun inversion results along the well trace (right) of Ida-1 that the soil probability density functions (overlaid in colour) are based on.*
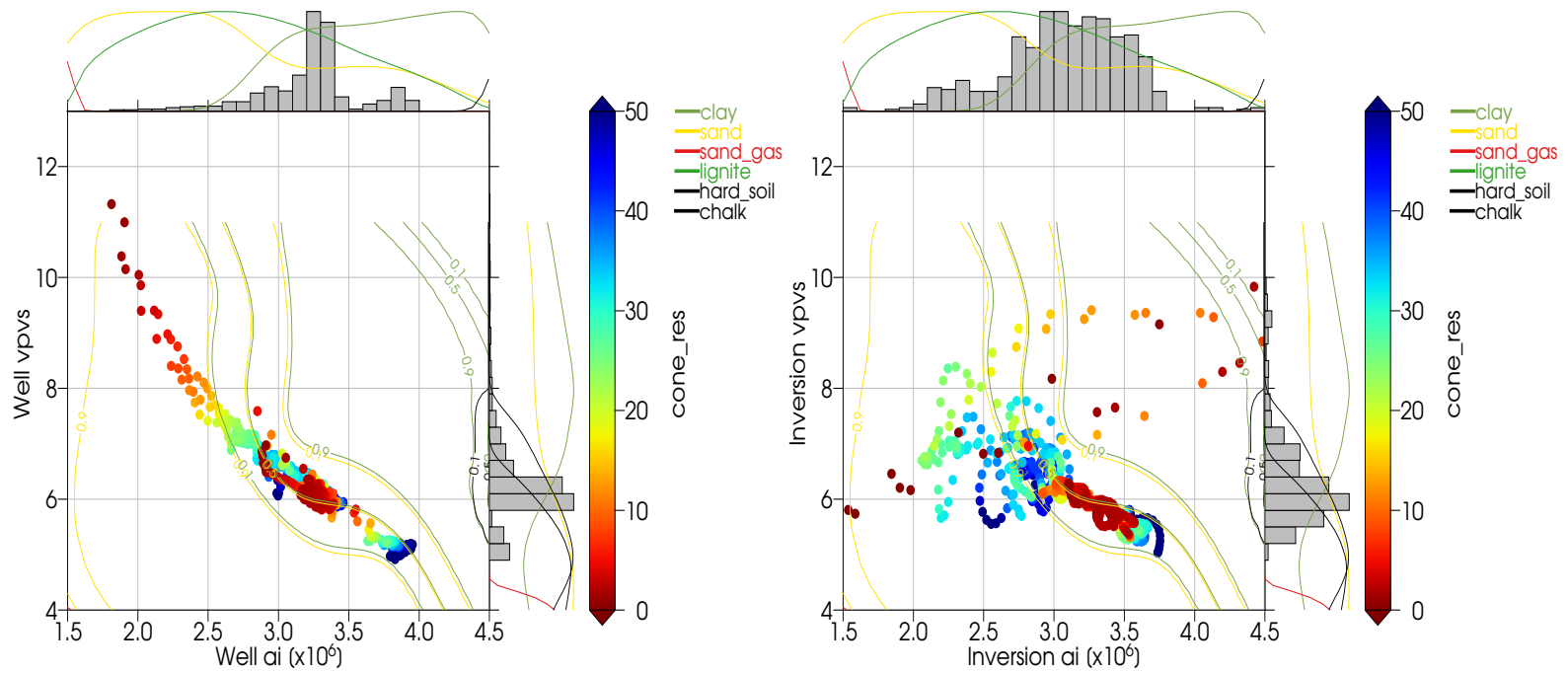
Figure 8.3: *The elastic properties derived from re-sampled CPT data (left) and the Sparker inversion results along the CPT trajectories (right) of CPT 020, CPT 020a and CPT 032 that the soil probability density functions (overlaid in colour) are based on.*
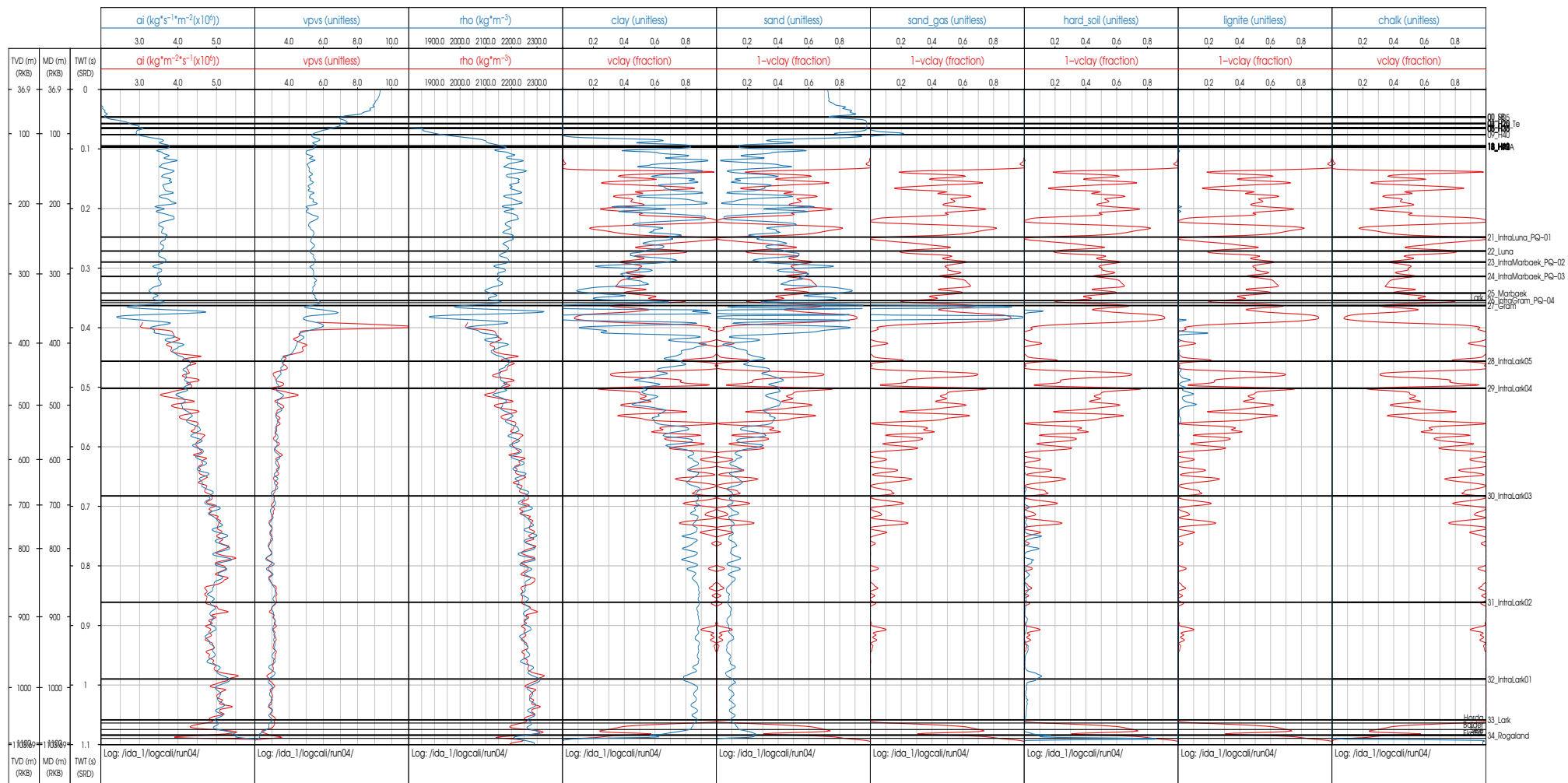
Figure 8.4: *Soil classification result of Airgun data along well Ida-1. The first three panels are curves for each elastic parameter, comparing the lowpass filtered log data and the inversion result along the well trace. The next six panels are curves for each soil type, comparing the probability for that soil type against a lowpass filtered log curve that makes sense to be compared against. In the case of clay probability, the volume of clay log is displayed. In the case of sand probability, one minus the volume of clay log is displayed.*
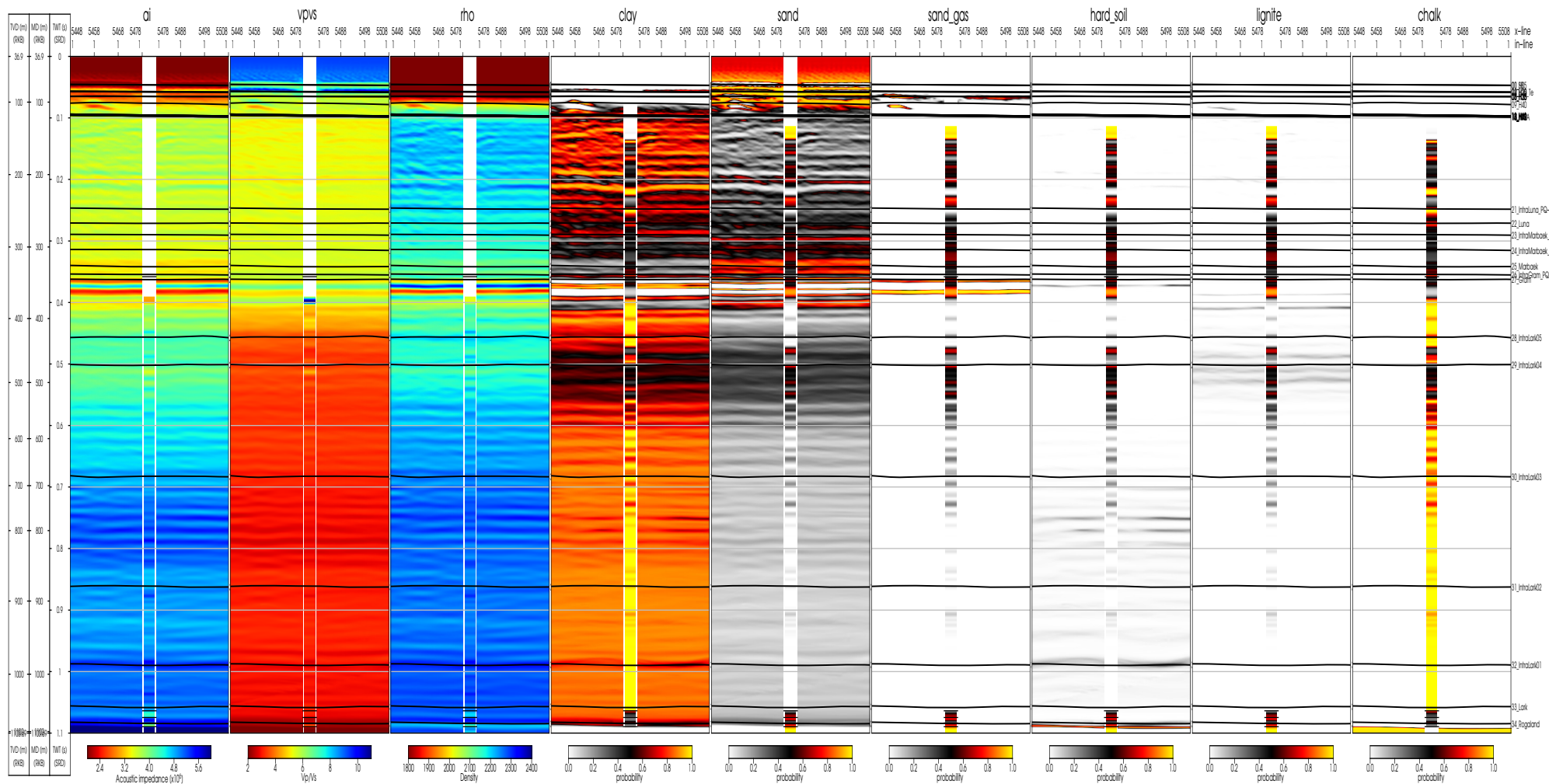
Figure 8.5: *Soil classification result of Airgun data along well Ida-1. The first three panels are curves for each elastic parameter, comparing the lowpass filtered log data and the inversion result along the well trace. The next six panels are curves for each soil type, comparing the probability for that soil type against a lowpass filtered log curve that makes sense to be compared against. In the case of clay probability, the volume of clay log is displayed. In the case of sand probability, one minus the volume of clay log is displayed.*
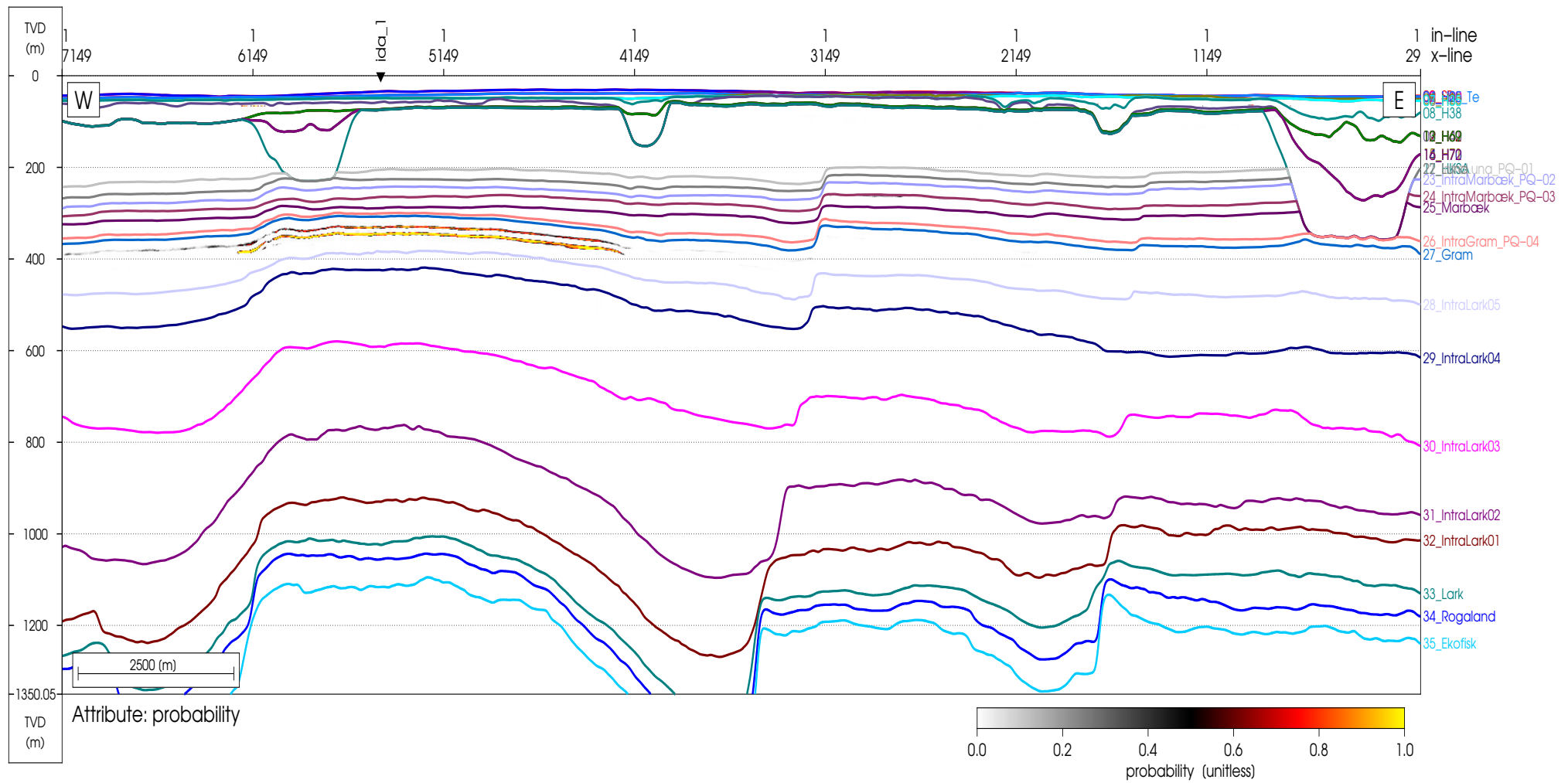
Figure 8.6: *Soil prediction of gas sand along line ML01, where there is knowledge of gas sand present. This is clearly visible along the section.*

Chapter 9

Pore pressure prediction

This chapter describes the results of using Eaton's method to scan seismic lines in the Energy Island North Sea area for indications of overpressure.

9.1   Introduction

Pore pressure is defined as the pressure of the fluid in the porous space of the soil or rock. Pore pressure prediction are methods that try to estimate the pore pressure from other data than direct pressure measurements. Pore pressure prediction is critically important to petroleum engineering at different stages: exploration, drilling, and production. It is the basic input data for the casing program optimization and the design of the drilling fluid density ("mud weight").

Pore pressure prediction is also important to find under-compacted formations with abnormal pore pressure in geomechanical applications to avoid issues if the pore pressure is relieved to the hydrostatic pressure by some mechanism.

To predict abnormal pore pressures, it is necessary to understand pore pressure and under which circumstances pore pressure becomes unusual. Pore pressures above hydrostatic pressure are termed overpressured. For deep wells the overpressure can be more than twice the hydrostatic pressure. The five major overpressure generation mechanisms are compaction disequilibrium (under-compaction), tectonic forces, clay diagenesis, aquathermal expansion, and hydrocarbon generation. The relevant mechanism in geology covering the project area is the effect on pore pressure by of under-compaction where sediments cannot expel the pore fluids in response to rate of deposition of sediment that causes loading of the underlying sediments. This leads to trapped pore fluid and the fluid begins to support the weight of the overlying sediments. The results is that the pore pressure is elevated from the hydrostatic pressure. When the fluid starts to support the weight of the overlying sediments it will retard or completely stop the porosity decrease with depth and this effects

the compaction trend of various physical quantities. Most importantly velocity increase with depth is less than expected. And similarly for resistivity. In most cases where compaction disequilibrium has been determined to be the primary cause of over pressure the rocks are geologically young and usually found in tertiary sedimentary basins of rapid deposition of sediments containing large quantities of clay minerals.

The preferred method for predicting pore pressure is starting from first principles developing a complete rock physics model that explains the elastic variables from physical properties like porosity, mineralogy, and effective pressure as an example. The rock physics model is then used in an inverse sense using the seismic results for the elastic variables to obtain the physical properties including pore pressure. This has the potential advantage of being applicable when there for example are changes to lithology and saturating fluids. However, it is rare to have quality data in the zone of interest to make such a model (full log suite, laboratory measurements) and at the same time a good predictive seismic inversion of the elastic variables. Even in a fortunate case of abundant data some geological settings are more difficult to model because of strong overlap in elastic properties for very different physical properties.

Eaton's empirical method is an industry standard method in areas of limited data and where a normal compaction curve can be reliably developed, where the lithology is relatively constant, and where the overpressure mechanism is under-compaction. Compaction is assumed driven by increases in effective (vertical) stress. The method works well for scanning for the onset of deviations from the normal compaction curve indicating overpressure and thus by definition is a method that works at a much coarser level since it detects deviations from a slowly varying trend.

All pore pressure prediction methods require data to calibrate the models to make precise numerical predictions. However, the study in questions the data is quite sparse. There are three (deep) wells outside the area of interest (Ida-1 is closest ~20km), lack of direct downhole pressure measurements (e.g. repeat formation test), and key parameters such as (acoustic) velocity and bulk density are modelled in the shallow parts (e.g. in Ida-1 well the acoustic slowness is measured from MD 368m and density from MD 1088m). The Eaton method can still be used to explore areas looking for abnormal pore pressure by searching for areas where at a certain depth there is a monotone onset of low velocity indicating under-compaction. Due to the lack of data the study at hand will calibrate a normal velocity trend model found in the literature to the shallow bore hole data. In a study with data spareness the normal trend is found from a literature study preferably using nearby wells.

Eaton's equation is given by

$$P_{\text{pore}}(z) = P_{\text{ov}}(z) - [P_{\text{ov}}(z) - P_{\text{hyd}}(z)] \cdot \left[\frac{V_{\text{p}}(z)}{V_{\text{p}}^{\text{NCT}}(z)} \right]^n, \tag{9.1}$$

where P_{pore} is pore pressure, P_{ov} is the overburden pressure, P_{hyd} is the hydrostatic pressure, V_{p} is the acoustic velocity typically from seismic inversion results or seismic interval velocities, and $V_{\text{p}}^{\text{NCT}}$ is the expected normal compaction trend for the acoustic velocity. The

Eaton exponent n was in the original paper [Eaton, 1975] set to 3 and it roughly depends on the rate of sedimentation. The Eaton exponent is a measure of the sensitivity of the velocity to changes in effective stress which correlates with rate of sedimentation.

Lithological variability and shallow overpressure create difficulty in defining the appropriate normal compaction trends for pore pressure estimation. Fluid expansion mechanisms and chemical compaction processes destroy the link between porosity and effective stress associated with normal compaction behaviour and challenge this type of method that relies on normal compaction trends only. However, chemical compaction and unloading by for example fluid expansion mechanism (aqua thermal expansion, clay dehydration reactions etc.) are assumed to be a secondary source of overpressure in most settings. These challenges can lead to an underestimate of the pore pressures. Furthermore, recognizing that geology is both complex and effects from glacial activity it is therefore diligent to develop a range of the uncertainty in pore pressure predictions to reduce any risk. In the study below conservative values will be chosen to ensure and upper bound for the pore pressure in this uncalibrated pore pressure study.

9.2 Method

The goal is to do pore pressure prediction down to the chalk in agreement with Energinet on the seismic lines in the Energy Island North Sea. In the sparse dataset case at hand, the following points needs to be addressed to accomplish that

- Literature study to find appropriate velocity normal compaction trend down to the chalk and verify consistent with data from the three deep wells Ida-1, Inez-1 and Ibenholt-1.

- Calibrate velocity normal compaction trend for the shallow data from available borehole data.

- Hydrostatic model.

- Overburden model.

- Eaton exponent.

- Acoustic velocity from the seismic inversion.

All the above items will be carefully chosen to ensure that we get a conservative estimate which is to overestimate rather than underestimate the pore pressure. The normal compaction trend is chosen with higher-than-expected acoustic velocity and the overburden model is chosen on the high side due to the lack of density information. The primary focus is to find the onset of monotonic increase in pore pressure (lower than expected velocities) due to the data sparseness of data in the project.

9.3 Results

It was not possible to find any pore pressure predictions studies very close to the Energy Island and/or that made use of the three wells closest to the project outline. However, in the paper [Vejbæk, 2021] a detailed study in the northern Danish Central Graben was carried out. Here it is shown that the Eaton method reproduces the pore pressure found from direct downhole pore pressure measurements using Repeat Formation Test (RPT). Nine wells were selected with data shallower than 1240 m. From the RPT measurements it could be concluded that the 9 wells were normally pressured (hydrostatic) and thus was fit for establishing a normal compaction trend. The paper concludes that Eaton's method has good predictive power. The normal compaction trend can be seen in the first track in Figure 9.2 as the grey curve. The three wells in the project are not located in the Danish Central Graben. Ibenholt-1 is situated on the Ringkøbing-Fyn High and Ida-1 and Inez-1 are situated in the Norwegian-Danish Basin. Nevertheless, Figure 9.2 shows that the three wells follow the normal compaction trend of the 9 wells very closely. This builds confidence that the normal compaction model can be used in Eaton's method over the target area.

The model overshoots the shallow boreholes of the project (data shown for BH-1022 and BH-1032). The focus of [Vejbæk, 2021] was not as shallow as for this project. A slightly better fit is found by calibrating the normal compaction model from [Vejbæk, 2021] with the shallow data, see black curve in first track on Figure 9.2.

The normal pore pressure gradient is a function of temperature, salinity, concentrations of various salts and dissolved gases. For this study, it is set to 1050 kg/m3 and is assumed constant. To get the overburden pressure one would integrate the density and use a density model where data is missing. However, due to lack of density data it is chosen to be constant at 2000 kg/m3 which overpredicts it for the shallow part by roughly 100-200 kg/m3. Overestimating the overburden density will be a conservative choice producing a higher pore pressure than expected.

The best predictive power in [Vejbæk, 2021] was found using an Eaton exponent $n = 2$. The original paper by Eaton uses an exponent $n = 3$. A larger exponent will make Eaton's equation more sensitive to a drop in velocity and thus produce a higher predicted pore pressure.
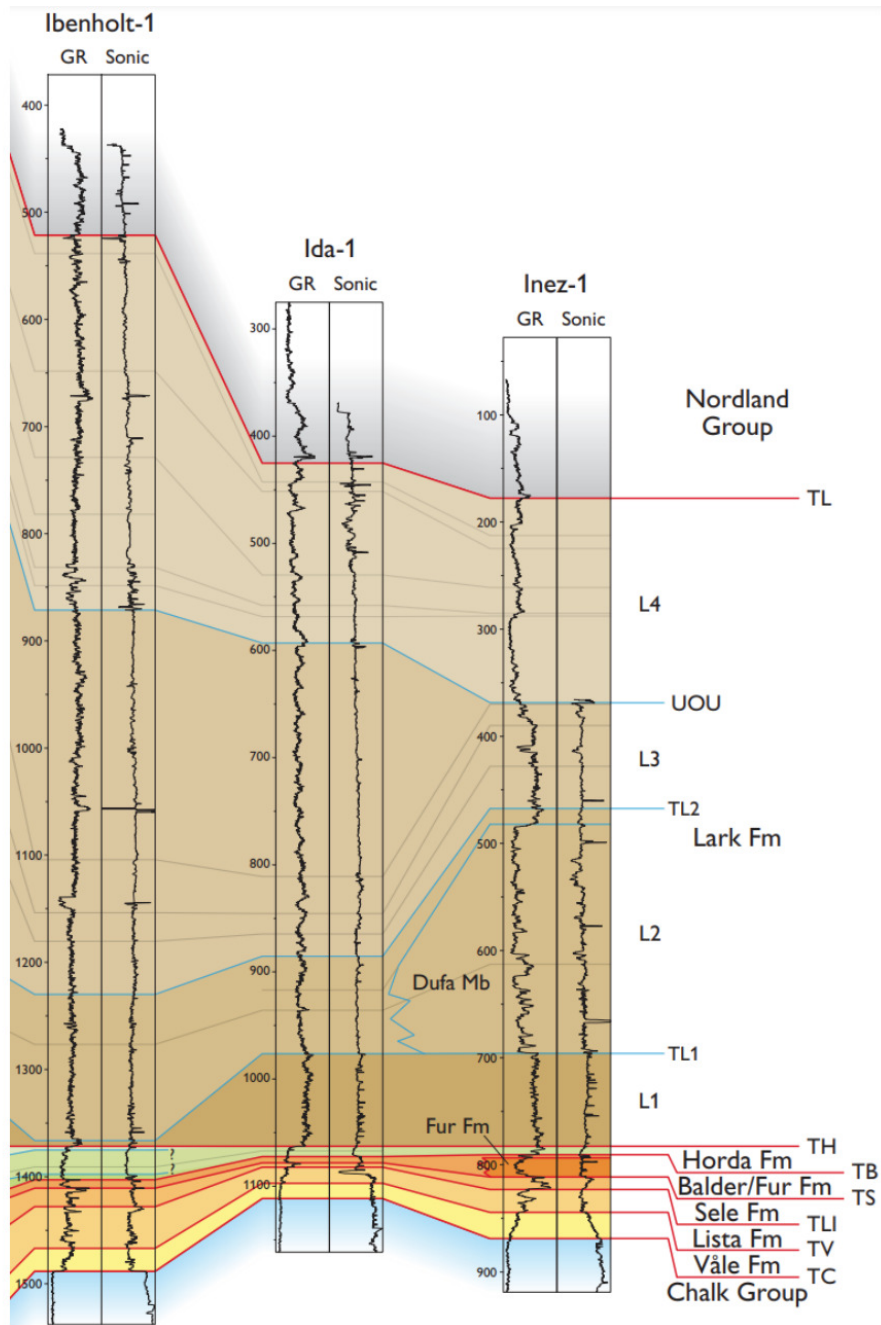
Figure 9.1: *The figure is from [Paul C. Knutz, 2022].*
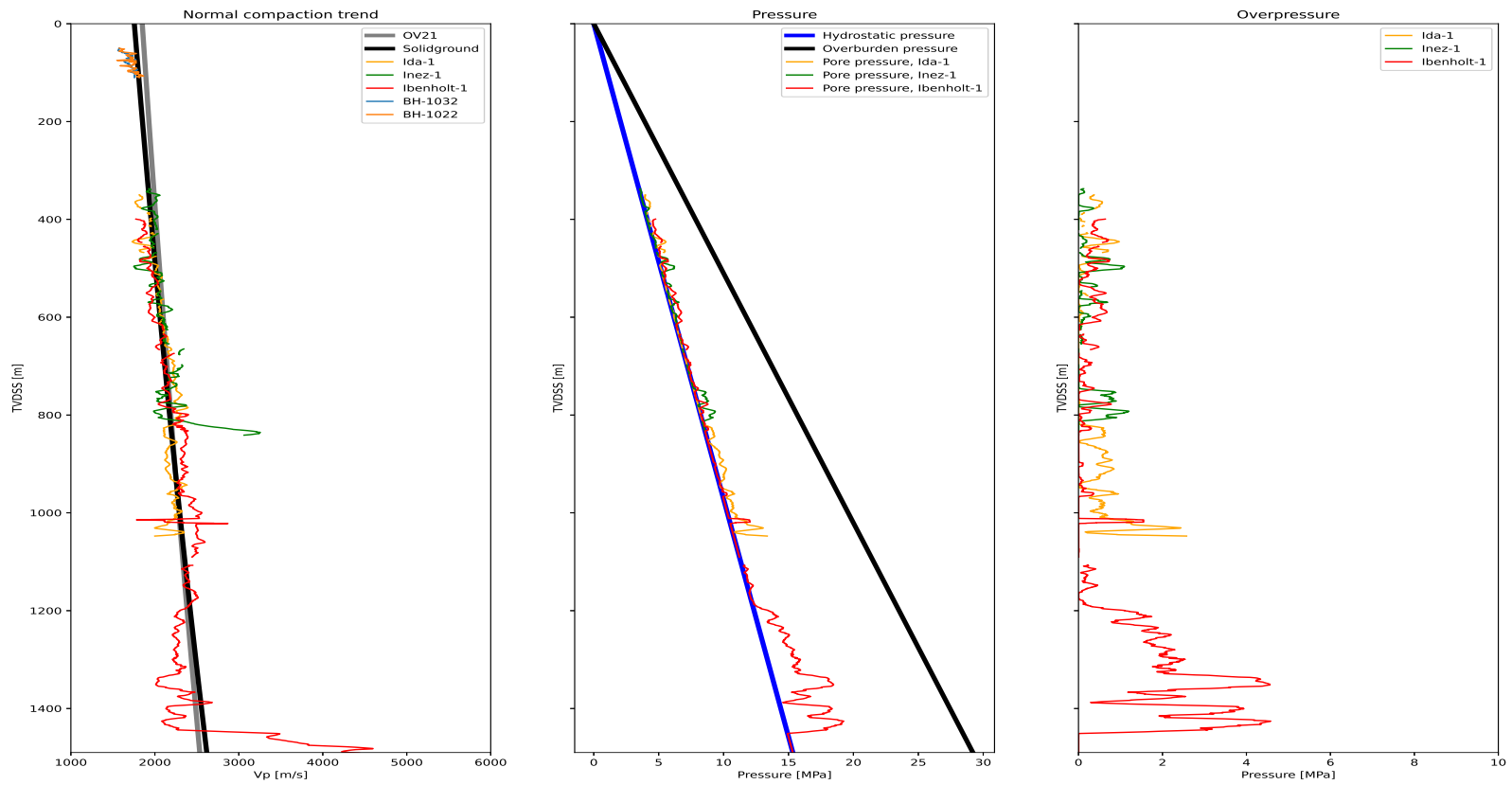
Figure 9.2: *The first track is the normal compaction trend for velocity. Notice the high velocity chalk spikes at 800 m in Inez-1 and at 1450 m in Ibenholt-1. The data is smoothed and thin high velocity non-shale values are removed. Notice that the Solidground model (black line) is less conservative by more accurately capturing the absolute value of the velocity in the shallow, but still on the conservative side (predicting too high velocity). The second track shows the pore pressure in the wells. And the third track show the overpressure. Notice that in the wells there are no onset of overpressure before 1000 m. In Ibenholt-1 overpresssure starts around 1200 m and in Ida-1 one could argue there is an onset of overpressure around 1000 m. This is consistent with findings in [Vejbæk, 2021] in the northern part of the Danish Central Graben.*

Appendix E shows, for each line:

- the hydrostatic pressure,

- the pore pressure,

- excess pore pressure,

where a value of $n = 2$ is used. At 1000m the hydrostatic pressure is 10.3 MPa.

To see where the pore pressure deviates from the hydrostatic pressure we can make a plot of the "excess" pressure which is the difference between the (conservative/upper limit) pore pressure predicted and the hydrostatic pressure.

The short scale fluctuations above unit L2 in the Lark formation are interpreted to be an artifact of lithology and fluid effects (gas in top of Gram formation in seismic line M01). These are also present when modeling the data in Figure 9.2. The apparent monotonic onset of deviating from the established normal compaction trend is indicated in the seismic lines in the older deep parts of the Lark formation in units L2 maybe even L3, see horizon on figures in Appendix E *31_Intra_Lark_02* on the plots. We see the same behaviour in Figure 9.2 where the start of the overpressure starts from around L2, see wells plots in Figure 9.1. This is consistent with the findings in [Vejbæk, 2021] where the conclusion is that the onset of overpressure is from the upper Cretaceous to mid-Miocene succession due to under-compaction mechanism of overpressure and thus the shallower units are in hydrostatic equilibrium.

The conservative choices made indicates that in the hydrostatic unit the pore pressure is consistently overestimated by 0.5 to 1.0 MPa. Therefore it is reasonable to assume that the overpressured deep zones before entering the chalk is overestimated as well. As stated earlier this study is done with limited data support and thus the main focus is to find onset of overpressure. The dependence of compaction normal trend has very little effect on the final result. However the Eaton exponent n has an effect on the absolute level of the pore pressure, but not on finding the onset of overpressure. For completeness the same results are presented for $n = 3$ in Appendix F.

Chapter 10

Conclusions

10.1 Geotechnical data

The report outlines the estimation of elastic soil properties from the available geotechnical tests in the Energy Island area. Correlations between CPT data and V_S, V_P and ρ are established and checked against the available data. Although there is some transformation uncertainty and a dependency on the methods used for measuring V_S directly (S-PCPT vs PS-logging), the proposed models provide results which are within a defined range of uncertainty ($\pm 30\%$ for V_S, $\pm 10\%$ for V_P and $\pm 15\%$ for unit weight).

10.2 Geophysical data

A large fraction of received geophysical data was the seismic data, a 2D dual seismic setup of 6 lines spanning a total of 90.34 km covering the area of interest. The data collection process involved the deployment of two distinct systems: a high frequency multi-channel seismic system targeting the shallow sections and a relative medium frequency multi-channel seismic system focusing on the deep sections.

The quality of the two data sets varied significantly. The high-frequency seismic data, intended for the shallow sections, exhibited a noticeably noisier character compared to the deeper medium-frequency seismic data. The primary challenge encountered during data acquisition was the presence of amplitude discrepancies along a line, attributable to unfavorable weather conditions. No geological factors were responsible for the dim vertical stripes observed along the seismic lines. However, this challenge was effectively addressed through the implementation of an amplitude balancing workflow as part of the preconditioning sequence.

10.3   Elastic and deformation properties

The pre-conditioned seismic angle-stack data were inverted for absolute values of bulk modulus, shear modulus and density with the aid of a background model. Other elastic properties such as Poisson's ratio, Acoustic impedance, V_P/V_S, V_P and Young's modulus were derived.

The results for the Airgun data are deemed of good quality. The Ida-1 well is predicted well in all three inverted (and other derived) properties. The Sparker results are deemed of sufficient quality, where extra caution is necessary for the very shallow part (first ~10 meters) due to the high amplitudes of the seismic data.

10.4   CPT prediction

The CPT prediction results resolve CPT properties within the seismic bandwidth and can be used to delineate spatial variations for specific CPT properties. By transforming the inversion results into the CPT domain a more direct evaluation of the seismic inversion results against the CPTs was possible, and we are now linking two completely independent measures namely seismic data and CPT mesurements.

Many of the challenges described in the previous chapters are also considered in the CPT prediction. As we are evaluating purely in the CPT domain and not in the elastic domain, the procedure of estimating elastic properties from the CPTs are less a dominant uncertainty factor in the seismic CPT prediction.

In general a very good fit between the seismic predicted CPT properties and the CPTs was observed at most CPT locations, also the behaviour of CPT predictions at the seismic lines are good.

10.5   Soil classification

The classification of the seismic data into six soil types, namely Clay, Sand, Gas sand, Hard Soil, Lignite, and Chalk, was performed using a probabilistic framework employing probability density functions. These functions were fitted to both well data and inverted data, and calibration was conducted wherever possible with respect to geophysical logs.

In the case of the Airgun data, the volume of clay log served as a reliable indicator for identifying the sand-shale transition. Regarding the Sparker data, the available calibration data was limited to the 'soil type' logs due to uncertainties in the time-depth relationships. The main challenge encountered in this field of study was the scarcity of supportive data.

However, it was demonstrated that meaningful probabilities could be derived from both the Ida-1 well and along line ML01, accurately identifying the presence of a gas layer. This provides reassurance but does not guarantee that these settings will accurately predict lithologies on other lines distant from the Ida-1 location.

10.6 Pore pressure

The conservative choices made during the analysis indicate a consistent overestimation of pore pressure by 0.5 to 1.0 MPa within the hydrostatic unit. Consequently, it is reasonable to assume that the overpressure in the deep zones prior to entering the chalk formation is also overestimated. Given the limited data support available for this study, the primary objective is to identify the onset of overpressure. The influence of the compaction normal trend on the final results is minimal.

However, the value of the Eaton exponent n does affect the absolute level of pore pressure, although it does not impact the identification of the onset of overpressure.

These findings align with the conclusions of the study referenced as [Vejbæk, 2021], which suggests that the onset of overpressure occurs within the upper Cretaceous to mid-Miocene succession due to under-compaction mechanisms. Consequently, the shallower units are believed to be in hydrostatic equilibrium.

10.7 Energy island location

In conclusion, the findings of this study were influenced by the limited availability of ground truth data, especially at greater depths, leading to a relatively high uncertainty of absolute values of deformation and elastic parameters. Despite this limitation, the seismic data quality was deemed to be of good quality, which resulted in a relatively low level of uncertainty with respect to the relative changes in the derived results.

Comparison of the seismic frequency bandwidth with the seismic derived results at ground truth locations, it is concluded that layers down to 50 centimeters are resolved with the high frequency system whereas layers down to 5 meters are resolved using the relative lower frequency system.

Zooming in on the results below the energy island location, a comprehensive examination was conducted to identify any significant anomalies within the sedimentary composition, pressure regime, and derived elastic parameters. The study indicated that the sedimentary composition in the pre-quaternary with a high likelihood primarily consists of clay, interspersed with a few layers of homogeneous sand. Notably, with high certainty the data did not reveal any evidence of gas or anomalous excess pore pressure in the pre-quaternary sand layers. The characteristics of the pre-quaternary layers, extending to the chalk surface,

were estimated to be similar to the observations from IDA-1, Ibenholt-1, and Inez-1 wells, except for the absence of gas beneath the seismic lines at the energy island location.

Regarding the quaternary section, the data analysis benefited from an extensive amount of ground truth data, which instilled a high level of confidence in the findings. However, the deepest channel infill posed the greatest uncertainty as it is unsampled by any ground pepetrations and lacked comparable sediment samples, making it a subject of future investigation.

In summary, while the study encountered challenges related to limited ground truth data, particularly at greater depths, the seismic data quality and the analysis of relative changes in derived results provided valuable insights. Future studies can focus on addressing the uncertainties associated with deeper channel infill and expanding the scope of ground truth data to enhance the accuracy and reliability of geological and geotechnical interpretations in the area.

Chapter 11

Delivered results

An overview of the delivered SEGY files with their respective filename and description is found on the following two pages.

A total of **516** files have been uploaded to the FTP.

Data	Files	Format
Airgun seismic in time	(6 lines, 10 anglestacks: **60 files**) Energy-Island-2023-May-17-**line**-airgun-2D-pre-conditioned-seismic-0.0-5.0-TWT.segy Energy-Island-2023-May-17-**line**-airgun-2D-pre-conditioned-seismic-5.0-10.0-TWT.segy Energy-Island-2023-May-17-**line**-airgun-2D-pre-conditioned-seismic-10.0-15.0-TWT.segy Energy-Island-2023-May-17-**line**-airgun-2D-pre-conditioned-seismic-15.0-20.0-TWT.segy Energy-Island-2023-May-17-**line**-airgun-2D-pre-conditioned-seismic-20.0-25.0-TWT.segy Energy-Island-2023-May-17-**line**-airgun-2D-pre-conditioned-seismic-25.0-30.0-TWT.segy Energy-Island-2023-May-17-**line**-airgun-2D-pre-conditioned-seismic-30.0-35.0-TWT.segy Energy-Island-2023-May-17-**line**-airgun-2D-pre-conditioned-seismic-35.0-40.0-TWT.segy Energy-Island-2023-May-17-**line**-airgun-2D-pre-conditioned-seismic-40.0-45.0-TWT.segy Energy-Island-2023-May-17-**line**-airgun-2D-pre-conditioned-seismic-45.0-50.0-TWT.segy	segy
Airgun relative inversion in time	(6 lines, 7 parameters: **42 files**) Energy-Island-2023-May-17-**line**-airgun-2D-inversion-relative-ai-TWT.segy Energy-Island-2023-May-17-**line**-airgun-2D-inversion-relative-vpvs-TWT.segy Energy-Island-2023-May-17-**line**-airgun-2D-inversion-relative-rho-TWT.segy Energy-Island-2023-May-17-**line**-airgun-2D-inversion-relative-e-TWT.segy Energy-Island-2023-May-17-**line**-airgun-2D-inversion-relative-g-TWT.segy Energy-Island-2023-May-17-**line**-airgun-2D-inversion-relative-k-TWT.segy Energy-Island-2023-May-17-**line**-airgun-2D-inversion-relative-pr-TWT.segy	segy
Airgun relative inversion in depth	(6 lines, 7 parameters: **42 files**) Energy-Island-2023-May-17-**line**-airgun-2D-inversion-relative-ai-TVD.segy Energy-Island-2023-May-17-**line**-airgun-2D-inversion-relative-vpvs-TVD.segy Energy-Island-2023-May-17-**line**-airgun-2D-inversion-relative-rho-TVD.segy Energy-Island-2023-May-17-**line**-airgun-2D-inversion-relative-e-TVD.segy Energy-Island-2023-May-17-**line**-airgun-2D-inversion-relative-g-TVD.segy Energy-Island-2023-May-17-**line**-airgun-2D-inversion-relative-k-TVD.segy Energy-Island-2023-May-17-**line**-airgun-2D-inversion-relative-pr-TVD.segy	segy
Airgun absolute inversion in time	(6 lines, 7 parameters: **42 files**) Energy-Island-2023-May-17-**line**-airgun-2D-inversion-absolute-ai-TWT.segy Energy-Island-2023-May-17-**line**-airgun-2D-inversion-absolute-vpvs-TWT.segy Energy-Island-2023-May-17-**line**-airgun-2D-inversion-absolute-rho-TWT.segy Energy-Island-2023-May-17-**line**-airgun-2D-inversion-absolute-e-TWT.segy Energy-Island-2023-May-17-**line**-airgun-2D-inversion-absolute-g-TWT.segy Energy-Island-2023-May-17-**line**-airgun-2D-inversion-absolute-k-TWT.segy Energy-Island-2023-May-17-**line**-airgun-2D-inversion-absolute-pr-TWT.segy	segy
Airgun absolute inversion in depth	(6 lines, 7 parameters: **42 files**) Energy-Island-2023-May-17-**line**-airgun-2D-inversion-absolute-ai-TVD.segy Energy-Island-2023-May-17-**line**-airgun-2D-inversion-absolute-vpvs-TVD.segy Energy-Island-2023-May-17-**line**-airgun-2D-inversion-absolute-rho-TVD.segy Energy-Island-2023-May-17-**line**-airgun-2D-inversion-absolute-e-TVD.segy Energy-Island-2023-May-17-**line**-airgun-2D-inversion-absolute-g-TVD.segy Energy-Island-2023-May-17-**line**-airgun-2D-inversion-absolute-k-TVD.segy Energy-Island-2023-May-17-**line**-airgun-2D-inversion-absolute-pr-TVD.segy	segy
Sparker seismic in time	(6 lines, 10 anglestacks: **60 files**) Energy-Island-2023-May-17-**line**-sparker-2D-pre-conditioned-seismic-0.0-5.0-TWT.segy Energy-Island-2023-May-17-**line**-sparker-2D-pre-conditioned-seismic-5.0-10.0-TWT.segy Energy-Island-2023-May-17-**line**-sparker-2D-pre-conditioned-seismic-10.0-15.0-TWT.segy Energy-Island-2023-May-17-**line**-sparker-2D-pre-conditioned-seismic-15.0-20.0-TWT.segy Energy-Island-2023-May-17-**line**-sparker-2D-pre-conditioned-seismic-20.0-25.0-TWT.segy Energy-Island-2023-May-17-**line**-sparker-2D-pre-conditioned-seismic-25.0-30.0-TWT.segy Energy-Island-2023-May-17-**line**-sparker-2D-pre-conditioned-seismic-30.0-35.0-TWT.segy Energy-Island-2023-May-17-**line**-sparker-2D-pre-conditioned-seismic-35.0-40.0-TWT.segy Energy-Island-2023-May-17-**line**-sparker-2D-pre-conditioned-seismic-40.0-45.0-TWT.segy Energy-Island-2023-May-17-**line**-sparker-2D-pre-conditioned-seismic-45.0-50.0-TWT.segy	segy

Data	Files	Format
Sparker relative inversion in time	(6 lines, 7 parameters: **42 files**) Energy-Island-2023-May-17-**line**-sparker-2D-inversion-relative-ai-TWT.segy Energy-Island-2023-May-17-**line**-sparker-2D-inversion-relative-vpvs-TWT.segy Energy-Island-2023-May-17-**line**-sparker-2D-inversion-relative-rho-TWT.segy Energy-Island-2023-May-17-**line**-sparker-2D-inversion-relative-e-TWT.segy Energy-Island-2023-May-17-**line**-sparker-2D-inversion-relative-g-TWT.segy Energy-Island-2023-May-17-**line**-sparker-2D-inversion-relative-k-TWT.segy Energy-Island-2023-May-17-**line**-sparker-2D-inversion-relative-pr-TWT.segy	segy
Sparker relative inversion in depth	(6 lines, 7 parameters: **42 files**) Energy-Island-2023-May-17-**line**-sparker-2D-inversion-relative-ai-TWT.segy Energy-Island-2023-May-17-**line**-sparker-2D-inversion-relative-vpvs-TWT.segy Energy-Island-2023-May-17-**line**-sparker-2D-inversion-relative-rho-TWT.segy Energy-Island-2023-May-17-**line**-sparker-2D-inversion-relative-e-TWT.segy Energy-Island-2023-May-17-**line**-sparker-2D-inversion-relative-g-TWT.segy Energy-Island-2023-May-17-**line**-sparker-2D-inversion-relative-k-TWT.segy Energy-Island-2023-May-17-**line**-sparker-2D-inversion-relative-pr-TWT.segy	segy
Sparker absolute inversion in time	(6 lines, 7 parameters: **42 files**) Energy-Island-2023-May-17-**line**-sparker-2D-inversion-relative-ai-TWT.segy Energy-Island-2023-May-17-**line**-sparker-2D-inversion-relative-vpvs-TWT.segy Energy-Island-2023-May-17-**line**-sparker-2D-inversion-relative-rho-TWT.segy Energy-Island-2023-May-17-**line**-sparker-2D-inversion-relative-e-TWT.segy Energy-Island-2023-May-17-**line**-sparker-2D-inversion-relative-g-TWT.segy Energy-Island-2023-May-17-**line**-sparker-2D-inversion-relative-k-TWT.segy Energy-Island-2023-May-17-**line**-sparker-2D-inversion-relative-pr-TWT.segy	segy
Sparker absolute inversion in depth	(6 lines, 7 parameters: **42 files**) Energy-Island-2023-May-17-**line**-sparker-2D-inversion-relative-ai-TWT.segy Energy-Island-2023-May-17-**line**-sparker-2D-inversion-relative-vpvs-TWT.segy Energy-Island-2023-May-17-**line**-sparker-2D-inversion-relative-rho-TWT.segy Energy-Island-2023-May-17-**line**-sparker-2D-inversion-relative-e-TWT.segy Energy-Island-2023-May-17-**line**-sparker-2D-inversion-relative-g-TWT.segy Energy-Island-2023-May-17-**line**-sparker-2D-inversion-relative-k-TWT.segy Energy-Island-2023-May-17-**line**-sparker-2D-inversion-relative-pr-TWT.segy	segy
Soil classification merged for sparker and airgun in depth	(6 lines, 6 soiltypes: **36 files**) Energy-Island-2023-May-17-**line**-sparker-and-airgun-soil-classification-chalk.segy Energy-Island-2023-May-17-**line**-sparker-and-airgun-soil-classification-clay.segy Energy-Island-2023-May-17-**line**-sparker-and-airgun-soil-classification-hard_soil.segy Energy-Island-2023-May-17-**line**-sparker-and-airgun-soil-classification-lignite.segy Energy-Island-2023-May-17-**line**-sparker-and-airgun-soil-classification-sand.segy Energy-Island-2023-May-17-**line**-sparker-and-airgun-soil-classification-sand_gas.segy	segy
Pore pressure prediction merged for sparker and airgun in depth	(6 lines, 3 properties: **18 files**) Energy-Island-2023-May-17-**line**-airgun-2D-hydrostatic-pressure-TVD.segy Energy-Island-2023-May-17-**line**-airgun-2D-pore-pressure-TVD.segy Energy-Island-2023-May-17-**line**-airgun-2D-excess-pore-pressure-TVD.segy	segy
CPT prediction merged for sparker and airgun in depth	6 lines, 1 property: **6 files**) Energy-Island-2023-May-17-**line**-sparker-and-airgun-2D-cone_res-TVD.segy	segy

Bibliography

[Aki and Richards, 1980] Aki, K. and Richards, P. (1980). *Quantitative Seismology: Theory and Methods*. W. H. Freeman and Company.

[Baldi, 1986] Baldi, G., R. B. N. G. M. J. . E. P. (1986). Interpretation of CPT and CPTu; 2nd part: Drained Penetration of Sands. *Fourth International Geotechnical Seminar, Singapore*, pages 143–156.

[Biringen and Davie, 2010] Biringen, E. and Davie, J. (2010). Suspension PS Logging for Geophysical Investigation of Deep Soil and Bedrock. In *GeoFlorida 2010: Advances in Analysis, Modeling & Design*, pages 1037–1048.

[Cha et al., 2014] Cha, M., Santamarina, J. C., Kim, H.-S., Cho, G.-C., et al. (2014). Small-strain stiffness, shear-wave velocity, and soil compressibility. *J. Geotech. Geoenviron. Eng*, 140(10):06014011.

[Eaton, 1975] Eaton, B. (1975). The Equation for Pore Pressure Prediction from Well Logs. *Proceedings of the Fall Meeting of the Society of Petroleum Engineers of AIME, Dallas, TX, USA*.

[Fugro, 2022] Fugro (2022). Geophysical Results Report North Sea OWF Zone West (Lot 2) Geophysical Survey | Danish North Sea.

[Gardner and Gregory, 1974] Gardner, G. H. F., L. W. G. and Gregory, A. R. (1974). Formation velocity and density-the diagnostic basics for stratigraphic traps. *Geophysics*, 39:770–780.

[Gomez and Stuyts, 2022] Gomez, D. and Stuyts, B. (2022). Bender element testing to determine small-strain shear modulus on Belgian North Sea soils. In *Proceedings of the 7th International Young Geotechnical Engineers Conference*. ISSMGE.

[Greenberg and Castagna, 1992] Greenberg, M. L. and Castagna, J. P. (1992). Shear-wave velocity estimation in porous rocks: theoretical formulation, preliminary verifications and applications. *Geophysical Prospecting*, 40:195–209.

[Huuse, 1999] Huuse, M. (1999). Detailed morphology of the Top Chalk surface in the eastern Danish North Sea. *Petroleum Geoscience*, 5:303–314.

[Huuse and Lykke-Andersen, 2000] Huuse, M. and Lykke-Andersen, H. (2000). Overdeep-ened Quaternary valleys in the eastern Danish North Sea: Morphology and Origin. *Quaternary Science Reviews*, 19:1233–1253.

[Keene et al., 2017] Keene, A. K. et al. (2017). *Next-generation equipment and procedures for combined resonant column and torsional shear testing*. PhD thesis.

[Mayne et al., 2010] Mayne, P., Peuchen, J., and Bouwmeester, D. (2010). Soil unit weight estimated from CPTu in offshore soils. *Frontiers in Offshore Geotechnics II*, 119:371–376.

[MMT, 2021] MMT (2021). Energy islands - North Sea - East - Geophysical survey for offshore wind farms and energy island North Sea.

[Nash et al., 2007] Nash, D., Sukolrat, J., Greening, P., and Benahmed, N. (2007). Comparison of shear wave velocity measurements in a soft clay specimen using time and frequency domain techniques. *Rivista Italiana di Geotecnica*, 25(2):56–68.

[Paul C. Knutz, 2022] Paul C. Knutz, Erik S. Rasmussen, K. D. S. L. . L. T. P. (2022). A desk study of the Geological Succession below a proposed Energy Island, Danish North Sea. *TEST*, 123.

[Rambøll, 2021] Rambøll (2021). Energy island Danish North Sea Geoarchaeological and Geological Desk Study.

[Robertson and Cabal, 2015] Robertson, P. and Cabal, K. L. (2015). Guide to Cone Penetration Testing. Technical report.

[Vejbæk, 2007] Vejbæk, O.V., B. T. B. P. E. M. R. E. S. U. (2007). Chalk depth structure maps, Central to Eastern North Sea, Denmark. *Bulletin 13*, pages 9–12.

[Vejbæk, 2021] Vejbæk, O. V. (2021). Soil unit weight estimated from CPTu in offshore soils. *Petroleum Geoscience*, 28.

[Wang and Mok, 2008] Wang, Y. and Mok, C. (2008). Mechanisms of small-strain shear-modulus anisotropy in soils. *Journal of geotechnical and geoenvironmental engineering*, 134(10):1516–1530.

[Zoeppritz, 1919] Zoeppritz, K. (1919). Über Reflexion und Durchgang seismischer Wellen durch Unstetigkeitsflächen. *Nachrichten von der Gesellschaft der Wissenschaften zu Göttingen, Mathematisch-Physikalische Klasse*, pages 66–84.